TU/e EINDHOVEN UNIVERSITY OF TECHNOLOGY

Development and application of a laminar coflow burner for combustion studies at high pressure

Citation for published version (APA):
Andrade Oliveira, de, M. H. (2012). *Development and application of a laminar coflow burner for combustion studies at high pressure*. [Phd Thesis 1 (Research TU/e / Graduation TU/e), Mechanical Engineering]. Technische Universiteit Eindhoven. https://doi.org/10.6100/IR732108

DOI:
10.6100/IR732108

Document status and date:
Published: 01/01/2012

Document Version:
Publisher's PDF, also known as Version of Record (includes final page, issue and volume numbers)

Please check the document version of this publication:

• A submitted manuscript is the version of the article upon submission and before peer-review. There can be important differences between the submitted version and the official published version of record. People interested in the research are advised to contact the author for the final version of the publication, or visit the DOI to the publisher's website.
• The final author version and the galley proof are versions of the publication after peer review.
• The final published version features the final layout of the paper including the volume, issue and page numbers.

Link to publication

General rights
Copyright and moral rights for the publications made accessible in the public portal are retained by the authors and/or other copyright owners and it is a condition of accessing publications that users recognise and abide by the legal requirements associated with these rights.

• Users may download and print one copy of any publication from the public portal for the purpose of private study or research.
• You may not further distribute the material or use it for any profit-making activity or commercial gain
• You may freely distribute the URL identifying the publication in the public portal.

If the publication is distributed under the terms of Article 25fa of the Dutch Copyright Act, indicated by the "Taverne" license above, please follow below link for the End User Agreement:

www.tue.nl/taverne

Take down policy
If you believe that this document breaches copyright please contact us at:

openaccess@tue.nl

providing details and we will investigate your claim.

Download date: 16. Nov. 2023

Development and application of a laminar coflow burner for combustion studies at high pressure

Proefschrift

ter verkrijging van de graad van doctor aan de
Technische Universiteit Eindhoven, op gezag van de
rector magnificus, prof.dr.ir. C.J. van Duijn, voor een
commissie aangewezen door het College voor
Promoties in het openbaar te verdedigen
op dinsdag 8 mei 2012 om 16.00 uur

door

Marcelo Henrique de Andrade Oliveira

geboren te Recife, Brazilië

Dit proefschrift is goedgekeurd door de promotoren:

prof.dr. L.P.H. de Goey
en
prof.dr. M. Aldén

Copromotor:
dr.ir. C.C.M. Luijten

Copyright©2012 by M.H. de Andrade Oliveira
All rights reserved. No part of this publication may be reproduced, stored in a retrieval system, or transmitted, in any form, or by any means, electronic, mechanical, photocopying, recording, or otherwise, without the prior permission of the author.

Cover Design: Verspaget & Bruinink
Cover Pictures: Paul R. Bloemen (the front page picture of the experimental setup) and Marcelo Oliveira (pictures of the flames)

Printed by the Eindhoven University Press.

A catalogue record is available from the Technische Universiteit Eindhoven Library.

ISBN: 978-90-386-3130-1

This thesis is dedicated to my parents, Maria Lourença de Andrade (in memoriam) and Valmir de Andrade Oliveira, for their unconditional love and commitment in giving me support for the best education they could afford; and to my wife, Judith de Jong Andrade Oliveira, who always encouraged me throughout the course of this thesis and believed that I could do it.

Contents

Summary **vii**

1 Introduction **1**
1.1 Motivation 1
1.2 The stepped approach in engine and fuels research at TU/e 3
1.3 Research goals 4
1.4 Thesis outline 5

2 Experimental setup **7**
2.1 Literature review 7
2.2 Design of the High Pressure Vessel and Burner setup (HPVB) 15
2.3 Liquid fuels vaporization 19
2.4 System layout and operation 20
2.5 Flame stability 21

3 Laser diagnostic techniques **39**
3.1 Line-of-Sight Attenuation (LOSA) 39
3.2 Laser-Induced Incandescence (LII) and Fluorescence (LIF) 43

4 Soot measurements with LOSA **53**
4.1 Soot measurements in laminar flames of gaseous and vaporized liquid fuels 53
4.2 Preliminary soot measurements at elevated pressures in methane-air diffusion flames 65

5 Soot, PAH and OH measurements in vaporized liquid fuel flames **73**
5.1 Introduction 74
5.2 Experimental methods 75
5.3 Results and Discussion 78
5.4 Conclusions 85

6 Soot, PAH and OH measurements in doped methane flames 89
6.1 Introduction . . . 91
6.2 Numerical approach . . . 92
6.3 Burner configuration . . . 92
6.4 1D numerical validation . . . 94
6.5 Experimental measurements . . . 94
6.6 Results . . . 97
6.7 Conclusions . . . 102

7 Feasibility study: burning velocities at elevated pressures 107
7.1 Laminar burning velocity . . . 107
7.2 Experimental setup . . . 109
7.3 Results and discussions . . . 113
7.4 Conclusions . . . 125
7.5 Recommendations . . . 126

8 Conclusions and recommendations 129

Appendix: Machining Drawings 133

Curriculum Vitae 139

Acknowledgements 141

Summary

Development and application of a laminar coflow burner for combustion studies at high pressure

The research presented in this thesis attempts to build a bridge between the most simplified systems that have been studied in literature (laminar flame burners, in which simple fuels such as methane, ethane or ethylene are burnt at atmospheric pressure) and the much more complex and demanding environment that is found in practical combustion engines. This is accomplished by designing and constructing a high pressure vessel and laminar burner (HPVB) integrated with an evaporation system. The capability of the HPVB setup of burning vaporized liquid fuels in laminar diffusion and partially premixed flames brings the important opportunity to isolate the impact of fuel chemistry on the combustion behavior of relevant fuels and biofuels. This experimental setup is particularly designed to offer optical accessibility for laser diagnostic techniques, allowing their assessment and development at elevated pressures.

Background information on the type of high pressure burners mostly used for combustion studies in laminar flames is reviewed in chapter 2, providing the basis for the design of the HPVB setup. A detailed assessment of the design capabilities of the HPVB setup and the flame stability issues encountered are also presented and discussed. The flames of gaseous fuels show very good stability at atmospheric pressure with flame height standard deviation (σ) over time of less than 1%. Flame stability of vaporized liquid fuels at atmospheric pressure show strong dependence on fuel vapor flow, air coflow rates and the heated ring temperature. Operational conditions where flames show good stability are identified and presented as function of these parameters. Blends of n-heptane with oxygenated fuels are unstable and the use of cyclohexanone in the blend was found to damage the ball valves in the fuel line.

Chapter 2 also describes the challenges to stabilize high pressure flames and the design modifications necessary to improve flame stability. The design modifications

include an orifice, one-way-valve and a buffer placed in the fuel line, successfully damping the strong flame oscillations that lead to flame blow off. Overall flame stability is improved by increasing the volume of the chimney. Water droplets are formed at the tip of the aluminium fuel tube which causes methane-air diffusion flames become asymmetric for pressures higher than 0.6 MPa. Changing the aluminium fuel tube to a lower thermal conductivity material (stainless steel) keeps the fuel tip relatively hotter, avoiding the water droplet formation. Methane-air partially premixed flames do not show asymmetry and are stable up to 2.5 MPa. Long term stability of vaporized liquid fuels flames (n-heptane) is observed for pressures lower than 0.3 MPa. However, flame instability dramatically increases for higher pressures with strong flame flickering and oscillations.

The theory behind the laser diagnostic techniques applied in this work is reviewed in chapter 3. The LII (Laser-Induced Incandescence) and LOSA (Line-of-Sight-Attenuation) techniques are chosen for soot volume fraction measurements. The advantages and limitations of these techniques are identified considering their application using the HPVB setup to study laminar flames at elevated pressures. Instantaneous 2D maps of soot volume fraction distribution can be obtained with the LII technique, while the LOSA technique requires laser scans over the flame width and height. Therefore, the application of LII in this setup is recommended if measurements in a large range of flame conditions (different flow rates, type of fuels, etc.) and in low sooting flames are necessary. However, at high soot concentrations, signal trapping significantly affects the LII signal. Conversely, the signal (attenuation) to noise ratio of the LOSA technique only improves when measuring higher soot concentrations, making it more suitable for high pressure measurements. The LIF (Laser-Induced Fluorescence) technique is chosen for qualitative measurements of OH radicals and polycyclic aromatic hydrocarbons (PAH's), since these are species playing an important role in soot formation and oxidation.

Chapters 4 to 6 present the measurements carried out to characterize a large range of flames from gaseous and vaporized liquid fuels, using the mentioned laser diagnostics techniques. In chapter 4, the LOSA technique is verified by comparison with experimental data from literature, showing good correspondence both in peak values and location of maxima in soot volume fractions. Measurements in methane-air flames at elevated pressures indicate that the maximum soot volume fraction increases as $f_{v_{max}} \propto P^{2.46}$ over the pressure range of 0.6 to 1.0 MPa.

In chapter 5, using a combination of LII and LIF, soot, PAH and OH measurements are carried out to characterize two important surrogate fuels: n-heptane and n-decane. The results provide experimental data for future validation of numerical models in partially premixed flames of vaporized liquid fuels. The combined LIF and LII results, using both 266 nm and 1064 nm as excitation wavelengths, illustrate that: (a) this combination can provide unambiguous spatial identification of PAH and soot in laminar flames; (b) the maximum PAH LIF signal is a good predictor of $f_{v_{max}}$ from LII; (c) excitation at 266 nm with delayed detection results in a linear correlation with soot volume fraction from LII using prompt detection and 1064 nm excitation; (d) the influence of any additional photo-chemical processes using high laser power at 266 nm

and the influence of particle size for the delayed gate time, appear not significant for the flame conditions studied here; (e) the delayed and prompt measurements of LII signals spatially match, suggesting good synchronization between the different optical setups and a good flame repeatability of the HPVB setup.

Chapter 6 presents a combined experimental work (done by the author) and numerical modeling work (done by others) aiming at the investigation of the capability of the flamelet generated manifold (FGM) approach to numerically model multidimensional, laminar, non-premixed flames with the inclusion of PAH chemistry. Qualitative measurements of OH radical and PAH are carried out in a laminar CH_4/N_2-air co-flow flame doped with two dopants, benzene and toluene, each at three different concentrations. Results showed that the model is able to capture the major characteristics of PAH formation.

In chapter 7, the heat flux method for laminar burning velocity measurements is presented and a feasibility study is performed to extend the applicability of the method to higher pressures. This is accomplished by integrating the heat flux burner in the high pressure vessel of the HPVB setup. Measurements of burning velocities are achieved at pressures up to 0.5 MPa in premixed methane-air flames. The results show that improvements in the heat transfer from the burner plate to the burner head is crucial to extend the method to higher pressures, as well as to avoid strong flame instabilities in sub-adiabatic and close-to-adiabatic conditions. Chapter 8 summarizes the conclusions and provides recommendations.

Overall, a new and innovative experimental setup has been added to enrich the spectrum of experimental research on future fuels and engines, carried out at the Combustion Technology group at Eindhoven University of Technology.

CHAPTER 1

Introduction

1.1 Motivation

The global demand of energy continues to increase, despite the recent crises in the world economy and the uncertainties in the future perspective. An outlook by Exxon (figure 1.1) predicts that the global energy demand will be almost 30% higher in 2040 than it was in 2010 [1].

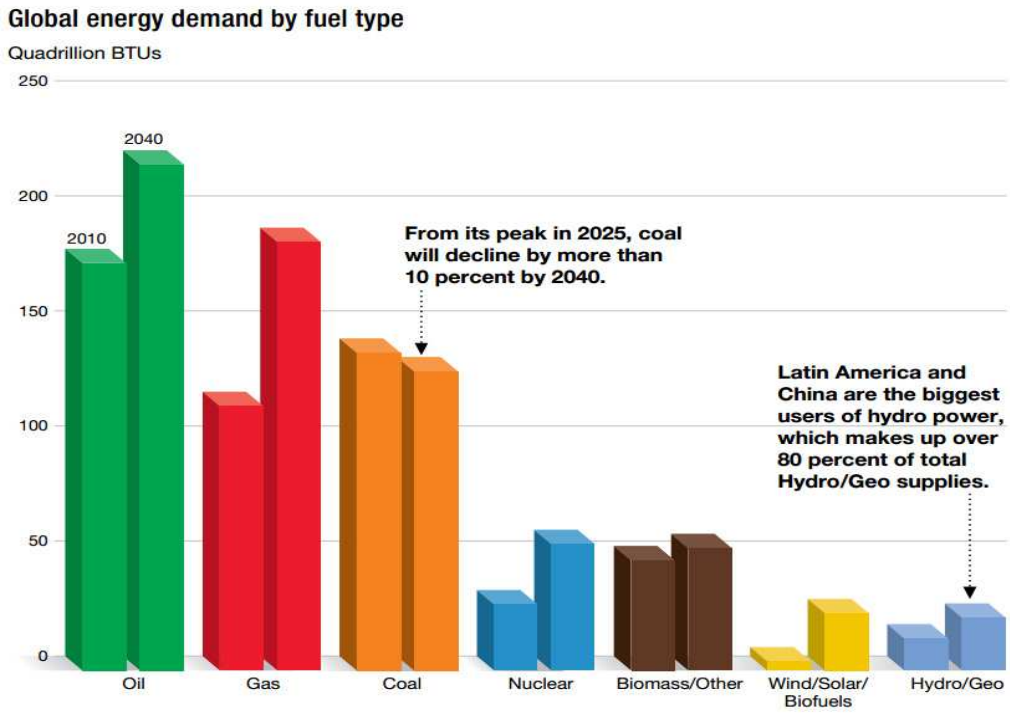

Figure 1.1: Projected demand of energy for 2040 (taken from Ref. [1]). BTU = British thermal unit ($\simeq$ 1055 Joules).

Combustion processes account for more than 90% of the energy conversion on earth. The most predominant sectors where combustion systems play a key role are transportation and electrical power supply. Fossil fuels are still carrying over 80% of the energy involved in these combustion systems. The energy outlook report provided by the International Energy Agency (IEA) foresees that the share of fossil fuels in the global primary energy consumption tends to slightly decrease (except for natural gas, which tends to increase) while renewable energy technologies will increase. However, IEA also predicts that the age of fossil fuels is far from over with the demand for all fuels rising until at least 2035 [2]. In the power sector, renewable energy will grow faster relatively to other energy forms but it will still be a small contribution in absolute terms of total energy supply. The transport sector will be responsible for the net increase in oil demand, driven by the economic growth of the emerging countries and their needs for personal mobility and transport of goods. While we have more flexibility to use different fuels (including gases and solids) to make electricity, this does not hold for transportation, since 98% of this sector runs on liquid fossil fuels.

In this scenario of growing energy demand, the emissions associated with fossil fuel combustion and the depleting fossil reserves motivate intense research on alternative fuels and on clean and efficient combustion processes. "Clean" usually designates low emissions of NOx, soot, unburnt hydrocarbons and carbon monoxide. "Efficient" typically indicates low fuel consumption. Among the candidates for partial replacement of fossil fuels are pure vegetable oils (for instance rapeseed oil), bio-diesel, GTL (gas-to-liquid) and ethanol. The way towards a more efficient and clean combustion process requires work on two fronts: (1) development of the combustion systems (for instance the engine, furnace or gas turbine) and (2) "engineering" of the fuel. The first resulted already in large improvements over the last decades, although there is certainly room for more developments. The second front requires improved understanding of combustion processes on a molecular scale, allowing the "design" of a fuel for best efficiency and lowest emissions. A combination of both strategies will lead to even more effective improvements.

Independently of the strategy taken, detailed understanding of the combustion process is necessary. In complex systems, such as a diesel engine, combustion occurs in a turbulent, high pressure, high temperature and unsteady conditions. Besides that, typical commercial fuels are blends of hundreds of components also containing very complicated molecular structures. Therefore, studying combustion on a molecular level in such combustion systems is not easy. Time-resolved and spatially resolved measurements of all relevant process parameters (temperature, velocity, fractions of all major and minor species) are necessary for a detailed understanding of the combustion behavior of fossil or alternative fuels. Such measurements seem simply impossible in real combustion engines and other combustion systems. The same difficulties hold for a complete numerical computation to understand and predict all relevant parameters, specially considering the number of chemical species and reaction mechanisms involved. There is a clear need for simplified systems in which the basic processes can be studied and the knowledge and tools acquired that can later be applied to practical combustion systems.

The most simplified combustion systems that have extensively been studied in literature include laminar flame burners, in which simple fuels such as methane, ethane or ethylene are burnt at atmospheric pressure. Among the reasons that most of these studies have been carried out with simple fuels at atmospheric pressure, are the experimental difficulties involved in vaporizing larger hydrocarbon fuels and achieving stable combustion in a well controlled pressurized environment. The challenges in experimental and computational analysis brought by the complex nature of practical liquid fuels can be tackled using the surrogate approach. Surrogate fuels are simpler representations of practical fuels that sufficiently represent their physical and chemical properties. Such fuels have been studied in practical devices, such as engines; however, it is difficult to isolate fuel chemistry effects from changes in flame lift-off length, temperature, pressure, and other variables, that may be caused by both physical and chemical effects.

In this work, an attempt is made to build a bridge between the most simplified and complex systems, by designing and constructing a high pressure vessel and laminar burner (HPVB) integrated with an evaporation system. The capability of the HPVB setup to burn vaporized liquid fuels in laminar diffusion and partially premixed flames makes possible studies aiming to isolate the impact of fuel chemistry on the combustion behavior of relevant fuels. This experimental setup was designed to offer ample optical accessibility for laser diagnostic techniques, also allowing their assessment and development at elevated pressures. In the next section, the HPVB setup is put into the context of the stepped approach taken for combustion engines and fuels research at Eindhoven University of Technology (TU/e).

1.2 The stepped approach in engine and fuels research at TU/e

The stepped approach in combustion engines and fuels research at TU/e consist of a systematic study of relevant combustion parameters throughout a well-balanced set of test rigs. Figure 1.2 places the experimental setups in perspective, considering the level of their practical relevance and experimental accessibility.

In the extremes, simple atmospheric burner systems offer great experimental accessibility while having low practical relevance compared to real engines. A considerable amount of research has been done in internal combustion engines, but most of these studies are limited to a kind of “black box” approach, in which flows into and out of the engine are analyzed. The optical engine setup is the first step to “open the black box”. It offers optical accessibility to the engine through a transparent ring, sometimes combined with a piston window in order to observe a plane near the cylinder head, where most of the combustion processes takes place. The Eindhoven High Pressure Cell (EHPC) is a so-called “spray bomb”, forming another simplifying step towards the understanding of diesel combustion. It is a constant volume chamber in which a diesel spray can be observed through windows. This helps a lot in the application of laser diagnostic tools, since the surrounding geometry of the spray does not move. Both the optical engine and EHPC setups are quite complex and hardly suited for fundamental combustion studies: unsteady and turbulent processes still take place

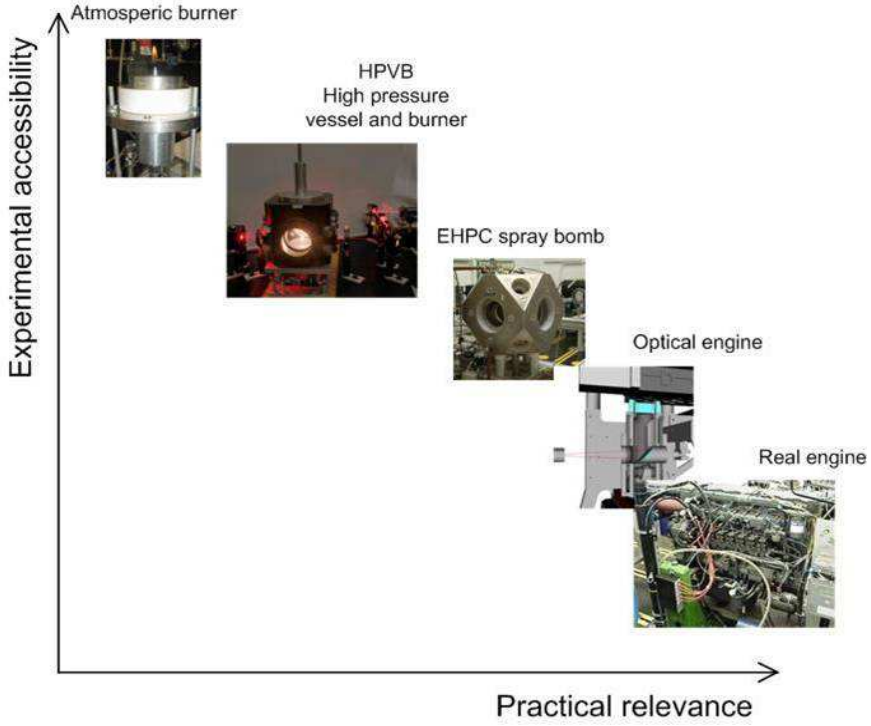

Figure 1.2: Position of the HPVB setup in the "spectrum" of available test rigs at TU/e.

at high pressure, making these setups only slightly simpler than the real engine from a combustion point of view.

The HPVB setup is an excellent candidate to bridge the gap between the simplest burner studies and the combustion research in real engines and turbines. The main reason is that the relevant complications can be introduced one-by-one like moving from gaseous to liquid fuels or moving from atmospheric to high pressures. Turbulence can also be introduced by manipulating the reactants' flow velocities and/or via small changes in the burner design.

1.3 Research goals

The main goal of this research is to develop a high pressure laminar co-flow burner, both as a tool for combustion studies and as a test vehicle for application of optical diagnostic techniques. Such experimental setup opens the opportunity for combustion research in a quite broad range of topics. Therefore, the first investigations with the HPVB have to be narrowed down and one relevant topic for combustion engine emissions is initially chosen: soot formation. Laser diagnostics will be applied in diffusion and partially premixed flames to measure soot volume fraction and other species playing a role in soot formation. The laminar burning velocity (S_L) is a key parameter that governs many properties of a combustible mixture. A feasibility study to measure S_L at elevated pressures using the heat flux method will also be carried out.

Summarizing, the goals of this research are:

1. Develop a high pressure co-flow burner and a modular/flexible high pressure vessel to study the combustion behavior of both gaseous and vaporized liquid fuels up to 3.0 MPa;

2. Apply laser diagnostics for soot studies;

3. Assess existing optical diagnostic methods for applicability at higher pressures;

4. Investigate the feasibility to study laminar burning velocities (flat flame burner) at elevated pressures, using the high pressure vessel developed.

1.4 Thesis outline

Following the introduction chapter, chapter 2 starts with background information on the type of burners mostly used for combustion studies in laminar flames. Focus is on the advantages and disadvantages of using these burners for measurements in a high pressure environment. Little research on flames from vaporized liquid fuels is found due to experimental difficulties involved in producing a stable vapor of larger hydrocarbon fuels. Nevertheless, some burners for vaporized liquid fuels, evaporation concepts and pressure vessels are evaluated in the process of designing our High Pressure Vessel and Burner (HPVB) setup. Subsequently, the design capabilities of the HPVB setup are discussed and the flame stability issues encountered are assessed at both atmospheric and elevated pressures. The main parameters observed to influence flame stability are discussed and a range of operational conditions for stable flames is defined and presented. The design modifications attempting to damp large flame oscillations and improve overall flame stability are also discussed and presented in this chapter.

Chapter 3 describes the theory behind the laser diagnostic techniques applied for measurements of soot volume fraction and qualitative profiles of polycyclic aromatic hydrocarbons (PAHs) and hydroxyl radicals (OH) reported in later chapters. In chapter 4, an optical setup is described for application of the line-of-sight attenuation (LOSA) technique for soot volume fraction measurements. The LOSA setup is validated using data obtained at atmospheric pressure in ethylene-air flames from literature and first measurements of a vaporized liquid fuel (n-heptane) are reported. Measurements of soot volume fractions in methane-air flames at elevated pressures are presented and the soot formation dependence on pressure is compared with literature data.

In chapter 5, partially premixed flames of the surrogate fuels n-heptane and n-decane are characterized in a range of equivalence ratios using a combination of Laser Induced Fluorescence (LIF) and Incandescence (LII) techniques to measure qualitative profiles of OH, PAH and soot, as well as soot volume fractions. In chapter 6, a similar laser diagnostic approach is applied in laminar CH_4/N_2-air co-flow flames

doped with benzene and toluene to provide experimental data for assessing a numerical model study (done by others).

The heat flux method for laminar burning velocity measurements was developed in our group by De Goey and co-workers [3–5] and has been applied for pressures between 0.02 and 0.3 MPa. A feasibility study to extend the applicability of this method to higher pressures is investigated in chapter 7, accomplished by integrating the heat flux burner in the high pressure vessel of the HPVB setup.

The thesis is finalized in chapter 8 with conclusions and recommendations.

Bibliography

[1] Exxon Mobil. The outlook for energy: A view to 2040. *Available in: http://www.exxonmobil.com/corporate/files/news_pub_eo2012.pdf*, 2012.

[2] International Energy Agency IEA. World energy outlook - executive summary. *Available in: http://www.iea.org/Textbase/npsum/weo2011sum.pdf*, 2011.

[3] L.P.H. de Goey, A. van Maaren, and R.M. Quax. Stabilization of adiabatic premixed laminar flames on a flat-flame burner. *Combustion Science and Technology*, 92:201–207, 1993.

[4] K.J. Bosschaart and L.P.H de Goey. Detailed analysis of the heat-flux method for measuring burning velocities. *Combustion and Flame.*, 132:170–180, 2003.

[5] R.T.E. Hermanns, A.A. Konnov, R.J.M. Bastiaans, L.P.H. de Goey, K. Lucka, and H. Köhne. Effects of temperature and composition on the laminar burning velocity of CH_4 + H_2 + O_2 + N_2 flames. *Fuel*, 89:114–121, 2010.

CHAPTER 2

Experimental setup

2.1 Literature review

2.1.1 Laminar flame burners

Most of the experimental work on the fundamental understanding of the combustion behavior of gaseous and liquid fuels has been carried out in laminar flame burners. The main reason is to avoid the complications introduced by turbulent fluctuations that also require time resolved measurements for their characterization. Laminar flames are considered as a starting point towards a more complex combustion environment. They permit line-of-sight diagnostic methods to be used and offer higher potential for application and development of advanced laser measurements techniques.

Laboratory flame configurations can be mainly classified as premixed and non-premixed flames. The most common type of burners to realize these flames are: flat flame burner, counter-flow burner and co-flow burner. Their working principle, advantages and disadvantages in combustion studies are reviewed in the following sections. Special attention is devoted to the applicability of these burners for elevated pressures and liquid fuels.

Flat flame burner

The flat flame burner has been used to study stable one-dimensional premixed flames over a large range of pressures. Fuel and oxidizer are mixed within the burner tube or chamber and exit through a nozzle which is packed with a thermally conductive material.

Flame chemistry has been characterized by measurement of OH, H_2, NO and temperature using laser diagnostics such as Laser-Induced Fluorescence (LIF) and CARS [1–3]. Soot properties have also been measured in flat flames by probe techniques. However, the flame front shifts towards the burner nozzle when pressure is increased

and, although Böhm and co-workers [4] have achieved 10 MPa, for pressures higher than 1.5 MPa measurements can only be achieved in the over flame region (flue gases) [5]. Besides that, the burner design for high pressure measurements is complex and requires continuous maintenance.

Counter-flow burner

The counter-flow burner is another very common laboratory burner. Fuel and oxidizer streams flow towards each other and flame front(s) may exist in the vicinity of the stagnation plane between them.

This burner can produce both premixed and non-premixed flames. These can be approximated as one-dimensional in the flame front region, which is an advantage for numerical simulation with detailed chemistry. Counter-flow flames have been used mainly for global flame parameter measurements, such as ignition, extinction and sooting limits [6–8]. The flames are stabilized through flame stretch and consequently they are inherently not as stable as those produced by the flat flame burner where flames stabilize by heat transfer to the burner surface. Despite that, a high pressure flame has been achieved by Sato [6] who studied the effect of pressure on flame extinction up to 3.0 MPa. Other difficulties with counter-flow burners are related to the strong dependence of flame properties on the stretch rate which is difficult to maintain constant when pressure is varied. Another problem is posed by measurements of the spatial distribution of combustion products.

Coflow burner

The coflow burner consists of two concentric circular tubes where the fuel flow is forced through the inner tube. The oxidizer flows through the space between the inner and the outer tube (figure 2.1). When only fuel flows through the inner tube, a non-premixed flame is formed and this is the type of flame that so far has been studied mostly. Eventually, air can also be mixed in the fuel tube creating partially premixed flames.

Temperature, species concentration and soot volume fraction have been measured in this type of burner using both probe techniques and laser diagnostics. Extensive work to characterize laminar non-premixed flames of gaseous fuels at atmospheric pressure, both experimentally and numerically, has been done by Long and Smooke [9–14]. In the probe techniques, an uncoated thermocouple is used for spatial measurements of temperature and a technique called thermocouple particle densitometry (TPD) is used to measure soot volume fractions. This technique is based on the error in the temperature measurement due to soot deposition and has an uncertainty of 50%. They also applied Rayleigh spectroscopy to measure temperature and Laser Induced Incandescence (LII) to measure soot concentration calibrating with extinction measurements. All flames have been studied at atmospheric pressure.

The work of Miller and Maahs [15] has been mostly referred to as one of the first on laminar non-premixed flames at high pressures. They measured NOx and temperatures up to 5.0 MPa in a coflow burner. Regarding the effect of pressure on

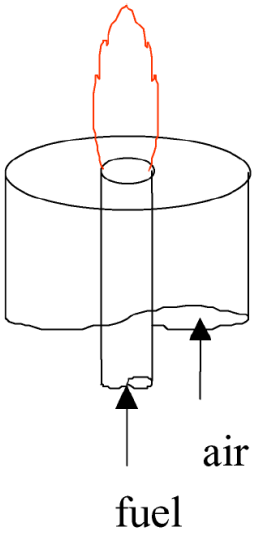

Figure 2.1: Coflow burner

soot formation in coflow burners, the work of Lee and Na [16] represents the first report of spatially resolved soot concentration, having achieved moderated pressures up to 0.4 MPa. Thomson and co-workers have greatly extended the pressure range by a factor of 10 by measuring spatially resolved soot concentration in methane/air flames at pressures up to 4.0 MPa. In his PhD thesis [17], Thomson points out several advantages of using the coflow burner for studies of soot formation at elevated pressures:

- Constant mass flow rate of fuel and air can be maintained while operating over a range of pressures allowing easy comparison of measured flame properties;
- The flame originates at the rim of the burner and extends well above. Therefore, it is possible to distinguish zones of soot nucleation and growth, even at high pressure;
- The coflow burner has a simple design with a basic tube-in-tube configuration, there is little maintenance required and there are few parameters to optimize during implementation of the burner;
- Good stability has been demonstrated for pressures up 5.0 MPa;
- The burner offers optical accessibility for spatially resolved observation of pre- and post-combustion characteristics.

McEnally et al. [18] also mention the advantage of coflow flames when applying probe techniques. Fuel decomposition and aromatics formation occur throughout the fuel-rich core of the flame, which has dimensions comparable to the flame height. These dimensions greatly exceed the spatial resolution achievable with sample probes allowing easy detection of differences between the spatial behavior of hydrocarbons.

2.1.2 Burners for vaporized liquid fuels

The majority of the work on characterization of atmospheric flames burning vaporized pure or multi-components fuels has been carried out in premixed flat-flame and counter-flow burners [19–24]. Coflow flames were mainly used to investigate aromatic pathways and soot formation by doping gaseous fuels with small amounts of the investigated liquid fuels. McEnally and co-workers have produced a large set of measurements utilizing this approach (see [18, 25–27] and references therein) which was first applied by Hamins and co-workers [28]. Only recently (2011), work has been reported on a setup burning a laminar coflow n-heptane flame [29].

Flat flame and counter-flow burners

Zervas investigated the formation of organic acids from propane, isooctane and toluene-isooctane flames [19] as well as the formation of oxygenated compounds in isooctane flames [20] by probe techniques. In both works, lean and rich premixed flames were stabilized on a flat flame burner. The liquid fuels were first evaporated in a long inox tube at 120 °C, and then mixed with air. The stability of the vapor flow was assessed by measuring the flame temperature which varied less than 2 °C, indicating a constant fuel/air ratio, so a constant evaporation rate. The fuel flow rate was controlled by a peristaltic pump.

Inal and Senkan also used the flat flame burner to characterize the structure of laminar n-heptane/oxygen/argon flames at atmospheric-pressure [21]. Two fuel rich conditions were investigated and benzene, large PAH's and soot were measured by both probe techniques and light scattering/extinction measurements. They also used a fuel rich n-heptane flame, applying the same burner and measurement techniques, to evaluate the effect of oxygenated additives (methanol, ethanol and MTBE) on the formation of polycyclic aromatic hydrocarbons (PAHs) and soot [22]. They found that all oxygenated additives reduced PAH and soot concentration. A high precision syringe pump was used to introduce the fuel and oxygenate into preheated mixtures of argon-oxygen stream at 150 °C. No more details about the evaporation concept or issues with flame stability were reported.

Berta and co-workers investigated the structure of non-premixed and partially premixed n-heptane flames both experimentally and numerically [23, 24] using the counter-flow burner. Flames were established by varying strain rates, equivalence ratios and nitrogen dilutions. They measured temperature with thermocouples. With probe techniques (microprobe and gas chromatography), they measured major species (O_2, N_2, CO_2, H_2O, etc), intermediate species (CO, H_2, CH_4, C_2H_4, etc) and higher hydrocarbon species (C_4H_8, C_4H_6, C_4H_4, C_4H_2, C_5H_{10} and C_6H_{12}). Their evaporation concept consisted of an electrically heated stainless steel chamber used as pre-vaporizer and n-heptane was led to this chamber by a liquid pump which maintained the desired mass flow rate. The chamber was filled with glass beads to increase its residence time and consequently enhance the heat transfer to the liquid fuel. Pre-heated air was mixed with the pure n-heptane flow to create rich premixed flames.

Coflow burner

According to McEnally and co-workers [18], who extensively applied the doped flame approach in coflow flames, the advantage of this methodology is that the dopant concentrations are chosen to be so small that the dopants do not affect the overall flame structure (size and shape, temperature distributions, residence times, etc.). Therefore, the effects on aromatic products (which are soot precursors) can be attributed directly to the chemical reactions of the dopant and its decomposition products. Sooting tendency of hundreds of hydrocarbon compounds have been reported [25, 27] as well as the identification of several aromatic formation pathways [18, 26]. They also claim that since simulations for large hydrocarbons are impossible, the doped flame approach is the only way to identify aromatic pathways. Besides that, it provides better experimental data to test detailed mechanisms because many uncertainties in measurements and the simulation can be factored out since the comparison of absolute concentrations in one flame is shifted to relative concentrations in a series of flames.

Although the doped gaseous fuel flame approach in coflow burners has been demonstrated to be successful in soot formation studies, it seems to be unsuitable for studies which investigate the impact of oxygenated fuels in reducing soot formation. An example is the work of McEnally [30] where a non-premixed ethylene flame was doped with DME and ethanol and both oxygenates showed an increase in soot concentration. They measured gas temperature with thermocouples, soot volume fraction with laser-induced incandescence, and species concentrations with a gas sample probe coupled to on-line mass spectrometry. The explanation given is that DME and ethanol decompose to methyl radical, which promotes the formation of propargyl radical (C_3H_3) and consequently the formation of benzene (soot precursor). Ethylene, however, does not decompose to methyl and its flames are particularly sensitive to this mechanism. Large alkanes that are part of most practical fuels, do decompose to methyl radical, and therefore, are not as sensitive to this mechanism as ethylene.

Wu and co-workers [31] also added ethanol to an ethylene flame and obtained the opposite result of McEnally. They observed that the addition of ethanol to ethylene decreased the soot concentration, as normally expected. They used, though, a different type of flames and methodology. McEnally used doped non-premixed flames in a coflow burner and Wu used partially premixed flames (ϕ =2.43 and 2.64) in a flat flame burner. Inal and co-workers [22] also used a flat flame burner to study the effect of ethanol on soot formation but used a different base fuel, a liquid fuel (heptane). As Wu, Inal reported a decrease in soot concentration. Wu and Inal obtained the same trend (soot concentration reduction) with the same type of flame (partially premixed) and burner (premixed flat burner) even using completely different base fuel (ethylene and heptane). The difference in trends between McEnally and Wu/Inal can be due to different reaction mechanisms present in the premixed and non-premixed flames. However, McEnally et al. did not perform measurements in partially premixed flames, nor did they use liquid fuels.

An ideal experimental setup seems to be one that can burn gaseous and vaporized liquid fuels in premixed and non-premixed configuration using the coflow burner

concept due to its mentioned advantages for high pressure measurements. It would be even more advantageous, if this setup would incorporate the fuel-doped approach by allowing these coflow gaseous and vaporized liquid flames to be doped with small amounts of liquid compounds. This is the kind of setup that has been the focus in this thesis. The most challenges are expected to be in the stabilization of these laminar coflow flames when burning vaporized liquid fuels, especially at elevated pressures. The liquid fuel evaporation concept is critical to achieve such laminar stable flames. Besides the ones utilized in some flat and counter-flow burners reviewed in this section, more detailed literature research is done in the next section.

2.1.3 Evaporation concepts

Bubbler systems

In many evaporation systems used in existing experimental or commercial installations, an inert gas is used as a carrier gas to transport the liquid fuel. To evaporate small amounts of liquid, bubbler systems are regularly used [32–34]. These systems run the carrier gas through a heated reservoir filled with a liquid which has to be evaporated. The liquid tends to evaporate as soon as it contacts the gas. The bubbles formed in the tank contain a mixture of the carrier gas and evaporated liquid. This evaporation method is hard to apply to the vaporization of multi-component liquids. Due to the range of boiling points of the components in such a liquid, the components with the lowest boiling points will start to vaporize first and leave the components with the high boiling points in liquid phase. The risk of having such a distillation process while running an experiment is critical and therefore this concept is discarded.

Hot plate evaporator

A concept which is fairly similar to the bubbler system is a hot plate evaporator. The main difference is the method of liquid supply. While the bubbler system has a heated reservoir, the hot plate or spray evaporator has an external reservoir and the liquid is inserted in the module through a hypodermic (hollow) needle. The spray from the needle hits a heated plate inside the evaporator which will vaporize the liquid. Similar to the bubbler system, a carrier gas will transport the vapor out of the evaporator. To avoid cooling the evaporated fluid, the carrier gas is preheated. An example of a hot plate evaporator is the module of Vranos [35, 36], see Figure 2.2, which is used to investigate the decomposition of vaporizing hydrocarbons with a high boiling point. The evaporator was entirely made out of copper, except for the fuel supply tube, and the internal surfaces nickel plated. The latter was done to avoid deposits of solid residues on the heated plate as much as possible. Unfortunately, deposits were observed during the course of testing [36]. This might be a drawback of using such an evaporator to produce a steady vapor flow. On the other hand, the investigations of Vranos conclude that the fraction of decomposed fuel is small if the temperature of the carrier gas is sufficiently high [36], which means that a representative fuel vapor can be created.

Another example of a hot plate evaporator is the module of Stobakk [37], see Figure 2.3, which is conceptually similar to the one of Vranos. The fuel is injected by a

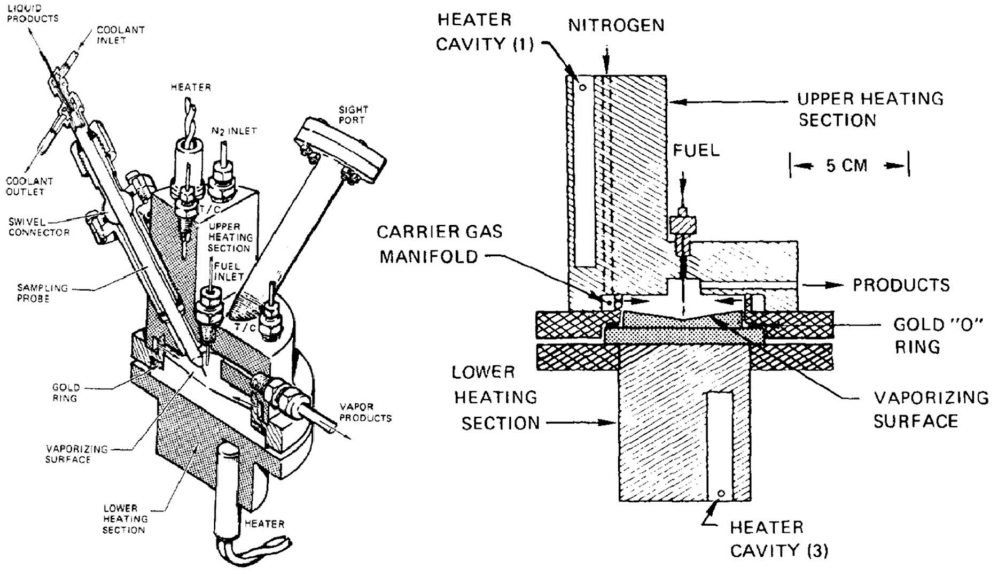

Figure 2.2: Two sectional views of the hot plate evaporator of Vranos [35, 36].

needle into a box which is heated from beneath by a heated plate and all the way around by heating tape. A pre-heated carrier gas is used to pressurize the fuel line via a by-pass and simultaneously transporting the vaporized fuel to the exit of the evaporator. In the investigations of Stobakk, a counterflow burner is connected to the evaporator and is used for flame extinction measurements. In their measurements, they used heptane, two component fuels and diesel fuel. The latter fuel gave problems due to high temperatures required in the evaporator, because some materials of the evaporator could not resist such temperatures. On the other hand, contrary to the findings of Vranos, they claim that all the components of the fuel are uniformly evaporated and no heavy components are left in the evaporator as deposits.

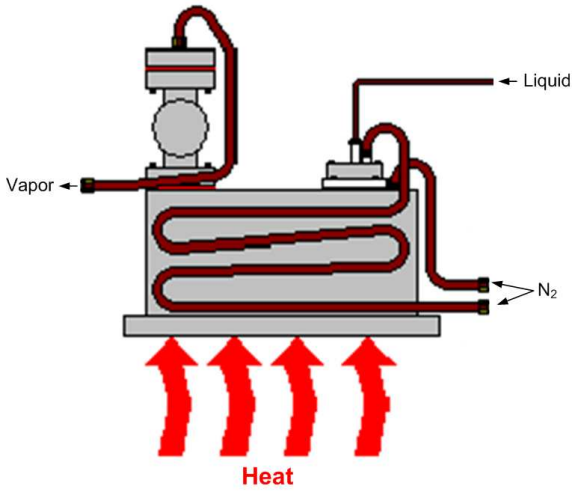

Figure 2.3: The hot plate evaporator design of Preben Stobakk [37].

Controlled evaporator mixer

A different concept to vaporize liquid in a carrier gas stream is obtained by a mixture vaporizer. In this concept, the liquid and carrier gas are mixed before both the fluids are heated. This mixing process can be controlled precisely, resulting in an accurate mixture composition, which consists of liquid droplets mixed in the carrier gas. After the mixing process, the mixture is externally heated, which vaporizes the droplets. An example of a mixture vaporizer is the controlled evaporator mixer, or short CEM, of the company Bronkhorst High-Tech, which is also a supplier of mass flow controllers. The CEM module, see Figure 2.4, can be divided into a mixing part, on the top side, and a heating part, at the bottom side of the module.

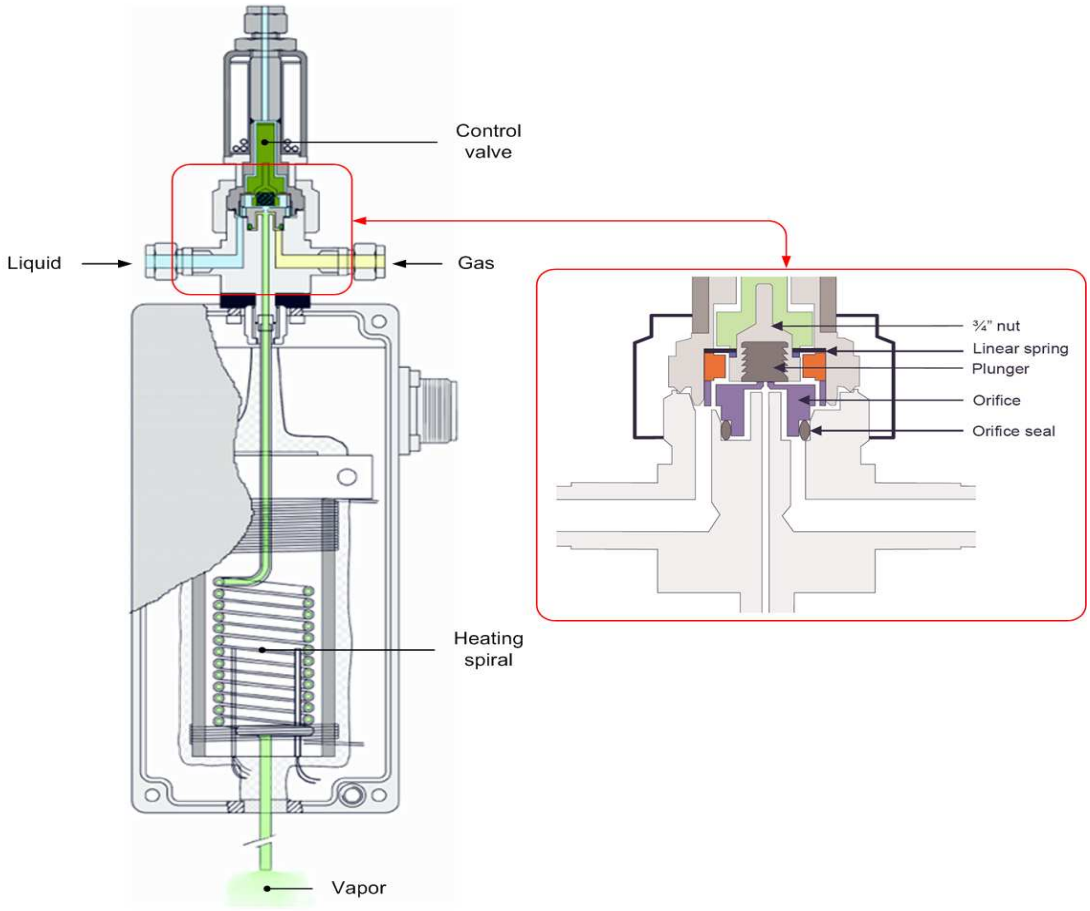

Figure 2.4: A schematic lay out of a Controlled Evaporator Mixer.

The mixing part mainly consists of a control valve and a liquid and gas connection. The control valve is able to restrict and control the liquid flow. The restriction is achieved by a small orifice, with a diameter of about 100 μm, which can be closed by a plunger. The plunger is spring loaded and naturally closed. An electric magnetic force is able to open the plunger, which causes the liquid to flow through the orifice. The mass flow of the liquid is measured upstream and by adjusting the magnetic force of the valve, the flow can be controlled. When the liquid is able to pass the

orifice, it will be cut off in small droplets by the carrier gas flow, which is entrained just underneath the orifice. This process creates a mixture of droplets and carrier gas. If the carrier gas mass flow is also measured and controlled, a very accurate mixture can be created. After the mixing process the mixture is forced to flow to the heating part of the module. The heating part consists of a spiral which is casted in a solid metal block and is externally heated. The mixture of liquid droplets and carrier gas flows through the spiral and heats up. If the temperature of the heated block is sufficient, the droplets in the mixture will vaporize. This process results in a stable and accurately controllable vapor flow. The main drawback related to the liquids considered for the experiments regarding automotive fuels, is the limited temperature of the CEM module. Due to prevention of melting the metal block, the temperature of the module is restricted to a maximum of 483 K, while the boiling point of diesel, for instance, range from 453 to 633 K. This module will be used in this thesis for the reasons discussed in section 2.3.

2.2 Design of the High Pressure Vessel and Burner setup (HPVB)

2.2.1 Vessel design

During the design of the high pressure vessel mainly three options were considered. The first design (Figure 2.5(a)) is the work of Miller and Maahs [15]. which is pioneer and one of the most refereed regarding laminar flames studies in pressurized environment.

The second design (Figure 2.5(b)) to be considered was the work of Thomson and co-workers [17, 38]. They based their burner design largely on the Miller and Maahs design. However there are significant differences in the pressure vessel design. Their high pressure vessel weighs 700 Kg with an internal diameter and height of 240 x 600 mm and can withstand pressures up to 10 MPa. The last design to be analyzed was the cubic shaped vessel design of the Eindhoven University of Technology (TU/e).

Since laser diagnostic techniques will be applied in this experimental setup, the vessel has to be optically accessible and proper windows are required to obtain this access. In the cylindrical vessel design, the windows need to be external, because there is not enough material structure in the wall of the main cylinder to attach the windows. Therefore, the cylindrical design contains welded support structures which are designed to support the windows. If the required windows become sufficiently large, the diameter of the main cylinder may become very large compared to the diameter of the burner. This is the case in the design of Thomson and co-workers [17, 38] where the internal diameter of the vessel (240 mm) is almost 10 times the diameter of the burner (25.4 mm) becoming a very large and heavy vessel. They have opted to put the whole burner assembly inside the vessel which is mounted on an external 3-axis translation system.

In contrast to the cylindrical vessel, the cubic shaped vessel design (Figure 2.5(c),)

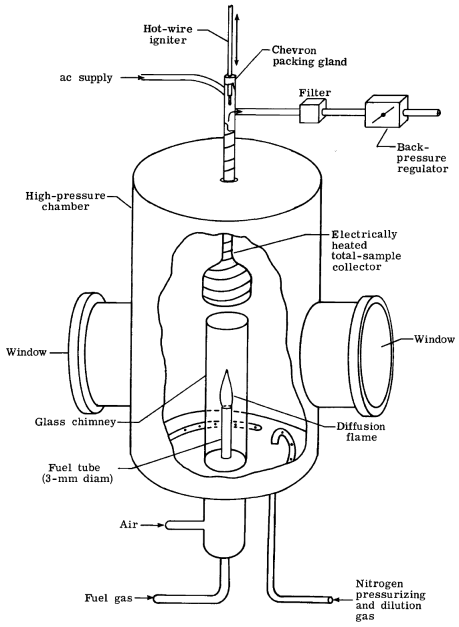

(a) Cylindrically shaped pressure vessel, with two optical ports [15].

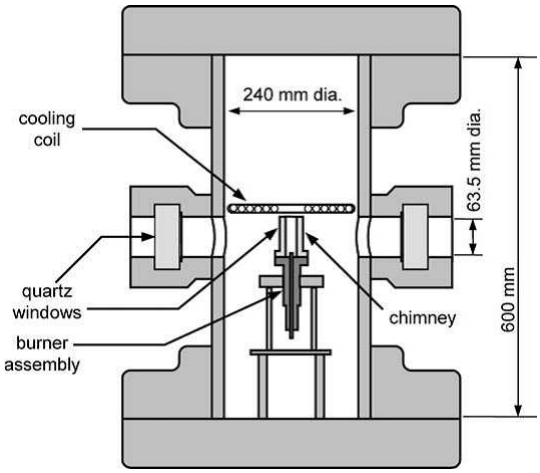

(b) Cylindrically shaped pressure vessel, with three optical ports [17].

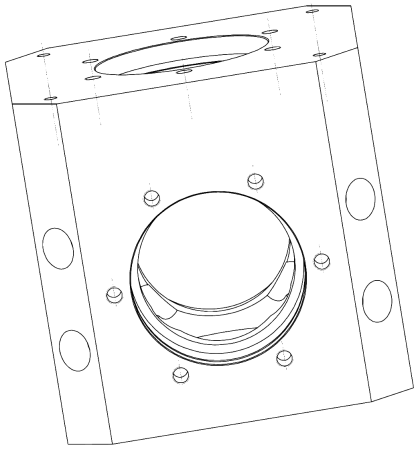

(c) Cubically shaped pressure vessel, with four optical ports and eight additional holes (on the corners).

Figure 2.5: Options for a design of a high pressure vessel.

does not require external windows. This design is focused on integrating the windows into the walls of the vessel. While the external shape is cubical, the internal structure is made out of three drilled cylinders through the three axes of the cube, which meet and merge in the center of this cube. The result is a robust and flexible high pressure design, with the possibility to have six access points from different directions. It also offers the opportunity to create additional holes to insert other measurement equipment, for example thermocouples for temperature measurements. The internal volume of the cylindrically shaped vessels of Miller and Maahs and Thomson are both approximately 27 dm^3 while the internal volume of the cubic shaped vessel is 1.6 dm^3, which is significantly smaller.

The flexibility of the cubic vessel, compact design and the in-house experience in other high pressure experiments, made this design more favorable than the cylindrical ones. Therefore, it was decided to use the cubic vessel design and adapt it for a high pressure burner.

2.2.2 Burner

The coflow burner developed by Long and Smooke has been used in extensive experimental and numerical studies of laminar flames [9–14]. It was made commercially available, giving other parties the opportunity to compare results obtained from experiments performed using the same burner. The dimensions of our burner is primary based on the burner by Long and Smooke. However, design information from other high pressure burner designs [15, 17, 38] were also considered.

The inner and outer diameter of the fuel tube are 4 mm and 6 mm, respectively. The inner diameter of the concentric tube, where the oxidizer stream flows, is equal to 50 mm and the height of the burner, from the bottom to the top of the coflow compartment is 100 mm. The (interchangeable) fuel nozzle is tapered both inside and outside to reduce the formation of turbulent eddies in the air and fuel flow. Sintered metal porous disks are used in the fuel and oxidizer line as also done by Miller and Maahs [15]. Other flow straighteners as aluminium beads (3 mm diameter) and perforated plates are placed in the air stream. A schematic drawing of the burner is shown in Figure 2.6.

The fit of the burner inside the pressure vessel is done by clamping the burner in one of the holes of the cubic shaped pressure vessel. In this case, the burner is partly placed inside the vessel, while the major part is left outside the vessel. This is done to efficiently use the space inside the pressure vessel and create a good alignment with the optical ports. Consequently, the pressure difference between the inside and the outside of the burner is increased significantly compared to the atmospheric burners, which implies the outer walls of the burner require sufficient strength to withstand the pressure difference. The drawing of the burner with detailed dimensions and material specifications can be found in the appendix. Figure 2.7 shows the setup assembly.

Liquid fuels have to be vaporized, and to avoid the cooling and consequent condensation of this vapor, the burner needs to be heated. This heat is supplied by a heated ring (supplying maximally 110 W of heat) which is mounted around the burner and is capable to keep the temperature of the burner at a constant temperature using

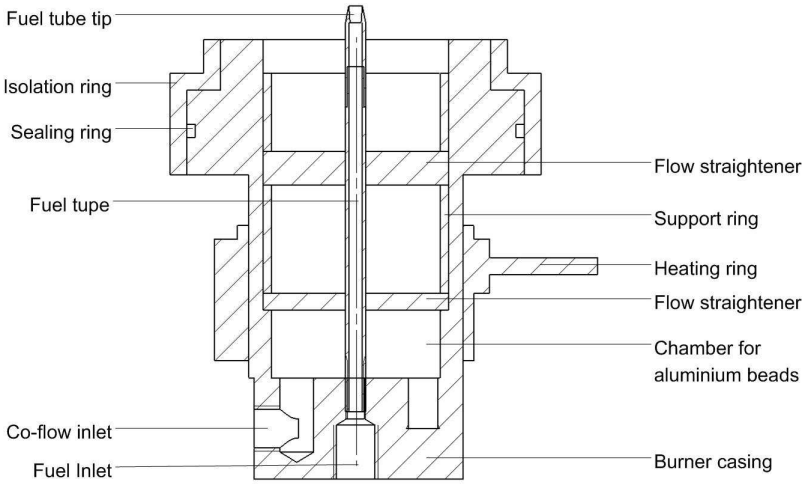

Figure 2.6: A schematic lay out of the burner.

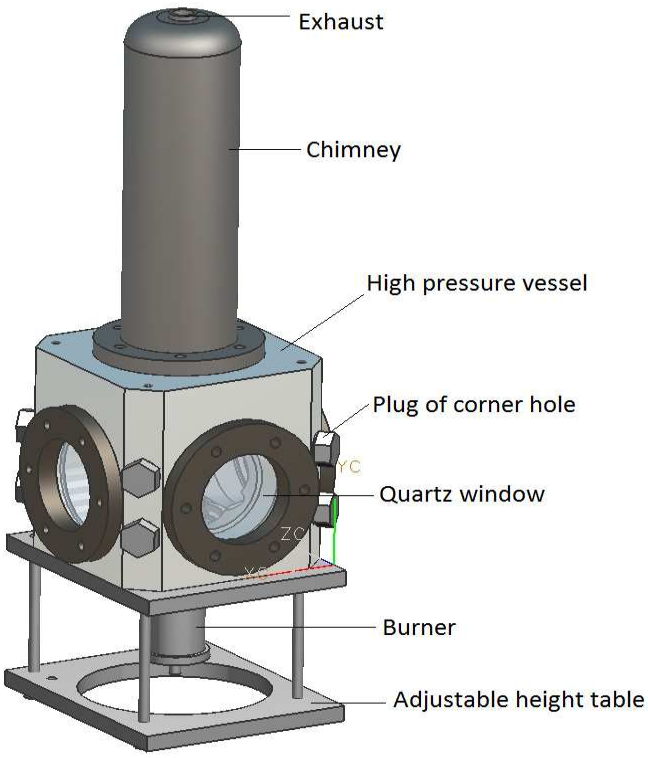

Figure 2.7: Pressure vessel and assembled parts.

a temperature controller. To enhance this control and to avoid unnecessary heat loss, the heated burner is isolated from the pressure vessel by a heat insulating ring made out of PTFE (Teflon). The burner is made of aluminum in order to transport heat more efficiently from the heated ring into the co-flow.

2.3 Liquid fuels vaporization

Some criteria were set up in order to decide for a fuel evaporation concept. The first criterion was the capability to vaporize the fuels with a high boiling point, requiring high temperatures for evaporation, which might give problems to the materials inside the devices. The second criterion was the guarantee of a fair vapor quality and purity, which creates a representative vapor flow for the experiments. A representative vapor flow implies that the chemical structure of the vapor is equivalent to the structure in the liquid phase. Deposition of heavy components of the fuel on parts of the device, creating solid residues, or decomposition of the fuel due to high temperature cracking, might destroy the chemical structure, which has to be prevented. The third criterion was the possibility to control accurately the mass flow which can be easily reproduced. The fourth criterion refers to the possibility to use the device in a pressurized environment, required for the experiments. The devices have to withstand elevated pressures and operating the burner in this environments might be of great value. The last condition is not the least important one: the availability of the devices. Can the components of the device be delivered from shelf or does it have to be designed and constructed?

The evaporation concept chosen is the Controlled Evaporator Mixer (CEM). It can deliver reproducible and accurate stable vapor flow, there is experience in its use at high pressure environments and good availability. The main drawback of the CEM is that the module has a limited maximum temperature of 473 K, which is too low to evaporate the components in the automotive fuels with a high boiling point, such as hexadecane ($C_{16}H_{34}$), which has a boiling point of 560 K. This issue is solved keeping the partial pressure of the liquid fuel below its saturation vapor pressure by increasing the carrier gas flow. If the mixture of liquid and carrier gas is sufficiently heated, the liquid will be entirely vaporized. To determine the partial pressure, the maximum vapor pressure of the liquid at the adjusted temperature of the evaporator is required. Figure 2.8 shows a vapor pressure chart of a range of hydrocarbon fuels. In every point above the line of a fuel, the fuel is in a liquid phase and in every point below the line it is in a gas phase. From this chart the partial pressure of a fuel p_f can be determined at a given temperature. Together with the total pressure of the fuel and carrier gas mixture, the fuel mole fraction can be determined by:

$$X_f = \frac{p_f}{p_t}, \tag{2.1}$$

where p_t is the total pressure of the mixture. For example, if hexadecane ($C_{16}H_{34}$) as fuel is considered and the maximum evaporator temperature is limited to 473 K, the vapor pressure of the fuel is maximum 0.075 bar, according to Figure 2.8. This means that, if the system is operated at atmospheric pressure (1 bar), the maximum fuel mole fraction X_f we can realize is 0.075, since $X_{fuel} = p_f/p_t$. The mole fraction of the carrier gas is determined by: $X_{gas} = 1 - X_f$. Now that the mole fractions are determined and the mass flow of the evaporated fuel and carrier gas mixture is known, the maximum fuel mass flow can be calculated using:

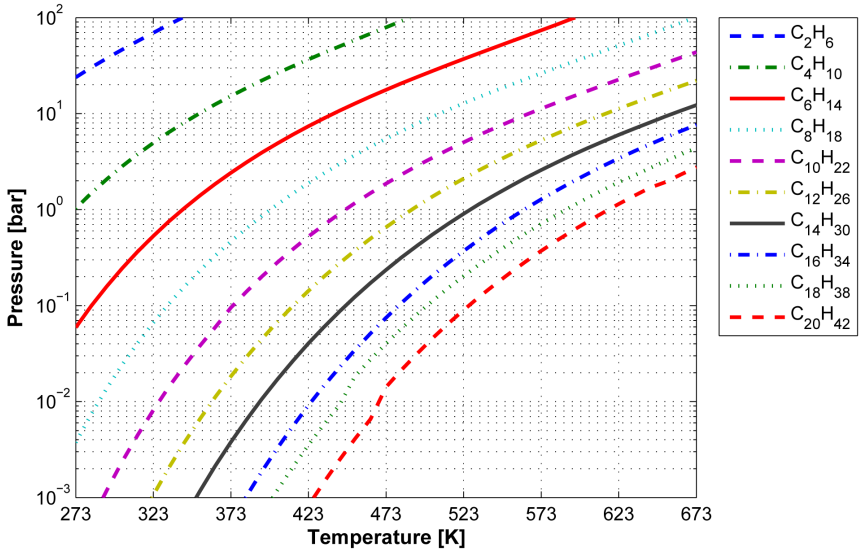

Figure 2.8: Vapor pressure chart of a range of hydrocarbons [39].

$$\phi_f = \phi_t X_f \frac{M_f}{\bar{M}}, \tag{2.2}$$

where ϕ_f and ϕ_t are the mass flow of respectively the fuel and the total mixture, M_f is the molar mass of the fuel and $\bar{M}$ is the mean molar mass of the fuel and carrier gas mixture, given by $\bar{M} = X_f M_f + (1 - X_f) M_{gas}$. During the experiments, carrier gas flow and the system temperature are always higher than the minimum required to avoid condensation.

2.4 System layout and operation

The HPVB is able to combust gaseous fuels and vaporized liquid fuels. In figure 2.9 the schematic system layout for gaseous fuels is shown. This layout is rather straightforward. The gas enters the burner in the middle and the air enters the burner from the side. If desired the gas can be diluted with nitrogen, to decrease the mass fraction of combustible gas entering the burner for a certain gas velocity. All gases are metered with calibrated mass flow controllers (Bronkhorst, EL-FLOW type).

The pressure in the vessel is regulated by the pressure controller which is placed in the exhaust tubing of the setup. Safety measure in case of vessel over pressurization is taken by installing one burst disk and one pressure relief valve via the available corner holes.

The layout for vaporized liquid fuels is more complex (see figure 2.10). The liquid in the fuel accumulator is pressurized with nitrogen, in the accumulator a membrane

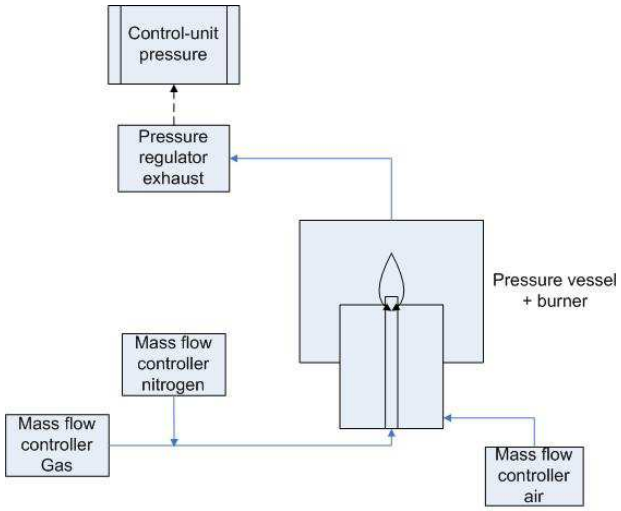

Figure 2.9: Schematic system layout for gaseous fuels

divides the liquid and the nitrogen. The flow of pressurized liquid is measured by the liquid flow meter (Bronkhorst, mini CORI-FLOW®) and the amount of liquid entering the burner is controlled by the controlled evaporator mixer (CEM). The nitrogen that goes through the CEM is controlled by the mass flow controller (MFC) nitrogen. The vaporized liquid fuels can be delivered at a temperature up to 200 °C. Because of risk for condensation these fuels may not cool down during the path to and through the burner. To prevent cooling and possible condensation of the vaporized liquid flow, the vapor hosing and total burner must be kept at 200 °C. To accomplish this the vaporized liquid is led to the burner through a heated hose of which the temperature can be set between 20 °C and 200 °C. Furthermore a heated ring is placed around the burner. Subsequently this will warm up the co-flow.

The flue gas from the chimney of the pressure vessel can have a temperature above 200 °C. The pressure regulator of the vessel can resist a maximum gas temperature of 70 °C. This means that the flue gas has to be cooled before it goes through the pressure regulator. The pressure regulator of the pressure vessel is coupled to the pressure regulator of the liquid fuel accumulator, in order to keep the pressure in the accumulator on a higher level than the pressure in the vessel.

2.5 Flame stability

The laminar coflow flames realized by the experimental setup are required to be stable for a period long enough to apply the measurement techniques proposed. This challenge is greatly increased when working at elevated pressures. For example, several problems are faced by Thomson and co-workers [17, 38] to stabilize a methane-air diffusion flame. They are our main reference regarding high pressure laminar coflow flames since they have reached stable flames in a larger range of pressures than others.

Intermittent and unpredictable flame stability and repeatability were observed

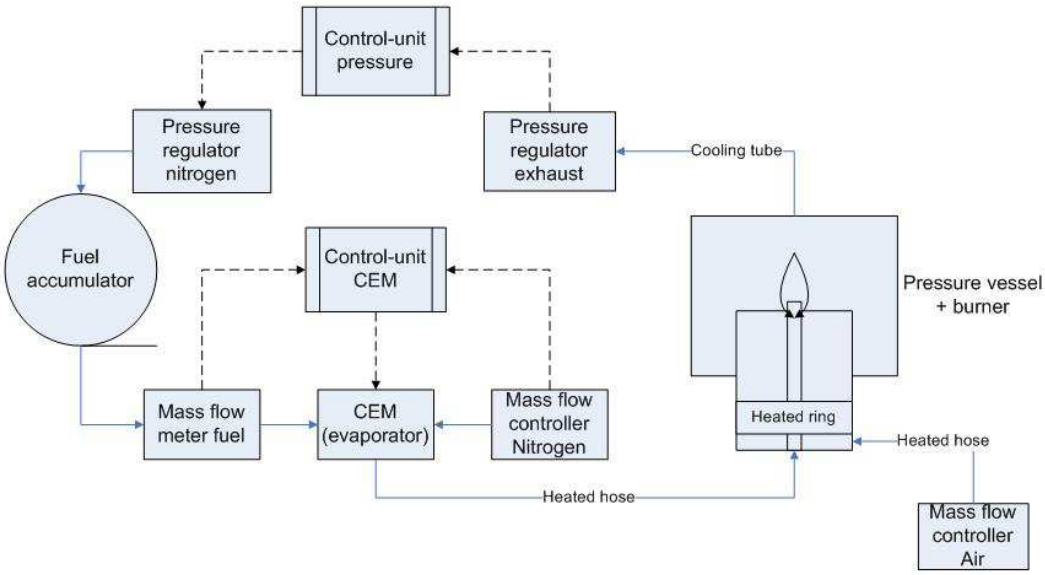

Figure 2.10: System layout for vaporized liquid fuels

under pressurized conditions [17]. They carried out air co-flow visualization using an argon-ion laser as a light source and smoke from incense (aromatic biological derived material which releases smoke when burned) to investigate the causes of instability. Large scale recirculation was occurring inside the chamber and flow patterns in the coflow-air were substantially different at elevated pressures compared to those observed at atmospheric pressure conditions for the same mass flow rate. At elevated pressure, the outer momentum driven air jet observed at atmospheric pressure is replaced by a slowly moving coflow which interacts strongly with the ambient fluid, exhibiting time dependent boundaries and vortical structures.

Flame stability was improved by increasing the coflow flow rate and the pressure limit for a stable flame was about 2.0 MPa for their vessel/burner combination. Further analysis showed that large flame instabilities were linked to periods over which recirculating water droplets interacted with the flame. In order to push this stability limit further, an inner chimney was placed around the flame as also done by Miller and Maahs [15]. The presence of the chimney walls limited recirculation of the combustion products and flames stable over longer than 30 seconds were achieved up to 9.0 MPa.

Fuel flow rate also plays a role in flame stability. Of the two main fuel flow rates studied by Thomson, the lower flow rate produced flames with better overall characteristics at high pressures. At pressures above 4.0 MPa, Thomson also observed other anomalies in the flame such as asymmetric or split flame shapes which were related to the formation of carbonaceous solids on the burner fuel nozzle rim. It is important to point out that the flow patterns influencing the flame stability will also depend on the vessel/burner configuration. Therefore, different stabilization problems and flame anomalies are also expected in our experimental setup.

The type of fuel burnt is another factor to be considered in flame stability. Gohari and co-workers [40] studied the effect of fuel variability on flame stability at elevated pressures. The dynamics of methane, ethylene and propane laminar diffusion flames were investigated at pressures up to 1.6 MPa by high speed imaging. The results show that the flame dynamics depend on the fuel used. In laminar diffusion flames, the flickering is known to be caused by the interaction of the flame and the vortices both inside and surrounding the flame jet. Gohari observed different vortex-flame interactions depending on the fuel type. The region (flow regime) of stable combustion was markedly reduced as pressure was increased and there is a linear dependence between the dominant flickering frequency of the flame and pressure.

Since our experimental setup is designed to also investigate the combustion behavior of liquid fuels, we expected to face much greater challenges due to a larger range of parameters that can influence flame stability. Indeed, elevated pressure measurements and the stabilization of vaporized liquid flames turned out to be very challenging. The following description of flame characteristics is not chronological and seeks to highlight the relevant observations and design modifications carried out to achieve and/or improve flame stability.

2.5.1 Gaseous fuels

This section describes the stability and general characteristics observed when gaseous fuels are burnt in the HPVB setup. First, flame height variation of diffusion flames of methane and ethylene is evaluated at atmospheric pressure. Methane flames are further characterized at elevated pressures in both diffusion and partially premixed modes.

Atmospheric pressure

The first flame stability tests were performed in atmospheric flames using as gaseous fuels methane and ethylene. The flame stability was evaluated on the basis of flame height variations. An ICCD camera was triggered at 1 Hz and used to record flame images during one minute. A paper grid was used to convert pixels to millimeters and the images were processed in a Matlab algorithm to obtain the flame height at several flow conditions. Table 2.1 shows the results for methane. The flows applied are shown on both volumetric (liters per minute, defined at 273.15 K and 101.325 kPa) and mass (grams per hour or grams per second) basis.

For ethylene flames, four different flames were reproduced from the work of Smooke et.al. [14] whose burner we based our design on. These flames were selected to validate our soot volume fraction measurements with the LOSA technique in Chapter 4. The fuel was a mixture of varying ratios of ethylene and nitrogen with an average cold-flow velocity of 35 cm/s. The results are shown in table 2.2 with the flames designated by the same ethylene/nitrogen flow ratio as in the paper of Smooke [14] to facilitate the comparison.

Table 2.1: Flame height variation in atmospheric methane-air diffusion flames

Fuel flow [L/min] - [g/h]	Flame height [mm]	σ [mm]	σ%
0.06 - 2.583	9.910	0.048	0.49
0.08 - 3.444	14.469	0.043	0.30
0.09 - 3.874	16.724	0.029	0.17
0.10 - 4.305	19.062	0.033	0.17
0.11 - 4.735	20.848	0.257	1.23
0.12 - 5.166	22.726	0.379	1.67
0.13 - 5.596	24.614	0.279	1.13

Both methane and ethylene flames have shown very good stability with flame height standard deviation (σ) of less than 1% in most of the conditions investigated. This is a similar level of flame stability obtained by Thomson [17] and considered acceptable to apply the LOSA technique for soot measurements.

Table 2.2: Flame height variation in atmospheric ethylene-air diffusion flames

Flame (C_2H_4/N_2%)	Flame height [mm]	σ	σ%
32/68%	25.6	0.042	0.16
40/60%	31.4	0.071	0.23
60/40%	50.6	0.063	0.12
80/20%	72.4	0.370	0.51

Elevated pressures - methane

Figure 2.11 shows a methane-air diffusion flame with fuel flow of 0.05 L/min (0.6 g/s) and coflow air of 20 L/min (0.43 g/s). At atmospheric pressure, the flame is completely blue with a bulbous appearance. When pressure is increased, the flame shape changes dramatically. Soot emission is visible already at 0.15 MPa in a small yellow tip and the soot region increases towards the base of the flame with increasing pressure. The diameter of the flame at its base is slightly larger than the burner diameter at atmospheric pressure and becomes narrow as pressure increases. When fuel flow is increased, the flame tends to be less stable and water condensation on the view ports also increases. Higher air coflow rate helps both to minimize the water condensation as well as to improve overal flame stability. These observations are in line with the work on diffusion methane-air flames of Miller and Maahs [15], Thomson [17] and Gohari [40].

The flame height increases up to 0.6 MPa which was the limit of stable flames. For higher pressures, anomalies start to occur when the flame starts to become asymmetric (see figure 2.12). This behavior could not be linked to carbonaceous deposits as observed by Thomson [17]. Instead, a water droplet is observed on the fuel tube tip

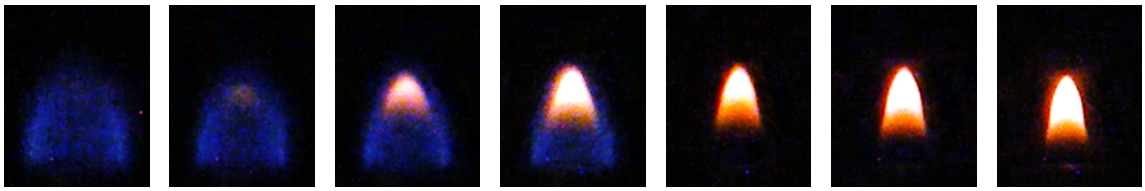

(a) 0.10 MPa (b) 0.15 MPa (c) 0.20 MPa (d) 0.25 MPa (e) 0.35 MPa (f) 0.45 MPa (g) 0.60 MPa

Figure 2.11: Direct photographs of diffusion methane-air flames at elevated pressures.

surface when the asymmetric flame shape is formed (see figure 2.13). A water droplet is also observed on the fuel tube tip when partially premixed flames are created for pressures higher than 0.8 MPa. However, in the case of partially premixed flames, no flame asymmetry is observed and the flames are stable up to 2.50 MPa.

(a) (b) (c)

Figure 2.12: Flame asymmetry in diffusion methane-air flames at elevated pressures. a) Methane 0.10 L/min, coflow-air 10 L/min, 0.74 MPa. b) Methane 0.10 L/min, coflow-air 20 L/min, 1.04 MPa. c) Methane 0.05 L/min, air 20 L/min, 1.04 MPa.

(a) (b) (c)

Figure 2.13: Water droplets on the fuel tube tip surface. a) Diffusion flame, b) Fuel tip, c) Partially premixed flame.

Partially premixed flames are formed when the fuel stream is mixed with a substoichiometric amount of air (referred to as primary air) before encountering a separate oxidizer (referred to as secondary air). They are characterized by a visible inner premixed flame front and an outer non-premixed flame. Partially premixed flames of

methane (primary equivalence ratio $\phi = 1.5$) can be seen in figure 2.14 for pressures up to 2.5 MPa. The flame is remarkably more stable than the diffusion flame. The flame height, defined by the inner premixed flame front, shrinks as pressure increases. The outer non-premixed flame becomes gradually narrower and an extended line of soot appears at the tip.

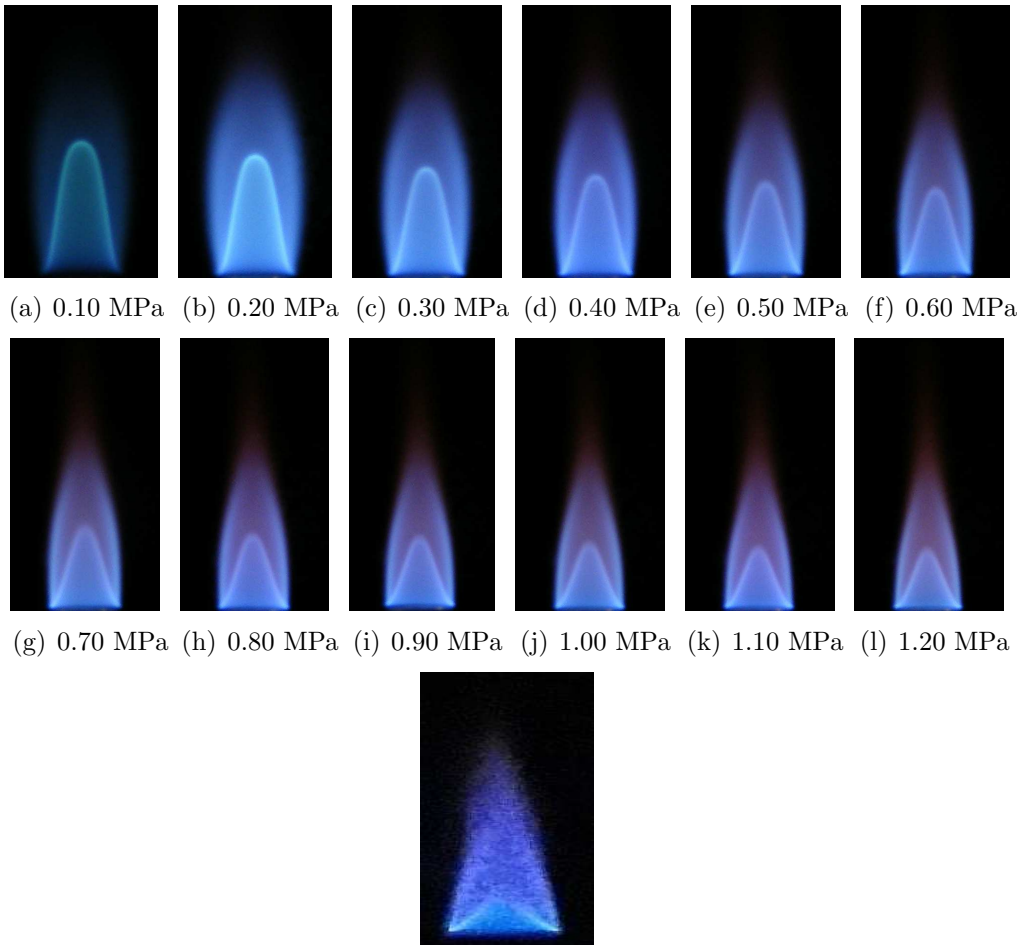

(a) 0.10 MPa (b) 0.20 MPa (c) 0.30 MPa (d) 0.40 MPa (e) 0.50 MPa (f) 0.60 MPa

(g) 0.70 MPa (h) 0.80 MPa (i) 0.90 MPa (j) 1.00 MPa (k) 1.10 MPa (l) 1.20 MPa

(m) 2.50 MPa

Figure 2.14: Partially premixed ($\phi = 1.5$) methane-air flames at elevated pressures.

2.5.2 Liquid fuels

In this section, the stability of vaporized liquid fuels is assessed at atmospheric and elevated pressure. The straight-chain alkane n-heptane is chosen as the main base fuel for the experiments for several reasons: a) its cetane number is similar to that of conventional diesel fuels, b) it is one of the primary reference fuels for octane number evaluation in internal combustion engines and c) it is a representative component of the aliphatic fraction in commercial gasoline and diesel oils. Besides n-heptane, fuel

blends including oxygenated fuels are also evaluated.

The relevant parameters and their effect on flame stability are summarized in the following subsections.

Temperature

In order to create flames from liquid fuels, they are vaporized using a carrier gas and their vapor flow temperature is controlled to avoid condensation. This is done by heating up the three main components where the vapor flows through: 1) the CEM, where liquid fuel and carrier gas are mixed; 2) the electrically heated hose that leads the vapor from the CEM to the bottom of the burner and 3) the electrically heated ring that is placed around the burner (see figure 2.10). The temperature in each of these parts can be controlled independently. System temperature refers to the same temperature set for all these parts.

Experiments with varying temperature of these three components and the flow rates showed that the coflow rate and the heated ring temperature affect more critically the flame stability. The heat generated by the electrically heated ring will first be transferred to the coflow air that surrounds the fuel tube. Consequently, the temperature of the fuel vapor will also depend on the heat transfer from the coflow air. When the coflow velocity is varied, the temperature field inside the vessel changes and a new equilibrium must be reached before the flames stabilize. The coflow rates that contributed for better stability varied between 20 and 25 L/min (0.43 - 0.54 g/s). In general, the observations show that the partially premixed flames are more stable if the system temperature is around the liquid fuel boiling point. For diffusion flames, higher temperatures show better stability.

Fuel flow rates

Using low fuel flow rates of around 4.5 g/h, a larger set of stable flames ($2 \leq \phi \leq 15$) can be created compared to higher fuel flow rates. For fuel flow rates larger than 5.0 g/h, partially premixed flames are more stable if the premixing air flow rate is higher than 0.26 L/min ($\phi \leq 6.5$). Comparatively, the diffusion flames are much less stable than the partially premixed ones at high fuel flow rates. However, stable diffusion flames can be achieved at high fuel flow rates if the temperature of the three components is higher than 150 °C and longer warm up periods (time > 3 hours) are applied.

The operational conditions for stable n-heptane flames at atmospheric pressure are summarized in table 2.3. The coflow rate is 25 L/min (0.54 g/s) and the carrier gas is nitrogen in diffusion flames and air in partially premixed flames.

Pressure upstream of the flow controllers

The pressure upstream of the mass flow controller (MFC) must be increased gradually in such way that it is always around 50% to 75% higher than the pressure inside

Table 2.3: Operational conditions for stable n-heptane flames at atmospheric pressure. The carrier gas is air for partially premixed flames (PPF) and nitrogen for diffusion flames (DF). Coflow = 25 L/min (0.54 g/s).

Flame type	Fuel flow [g/h]	Carrier gas [L/min] - [g/h]	System temp. [° C]
PPF	$\simeq 4.5$	0.057 to 0.471 - 4.42 to 36.54	> 100
PPF	5.0 to 8.5	≥ 0.26 - ≥ 20.17	> 100
DF	5.0	0.078 - 6.05	> 150
DF	6.0	0.104 and 0.130 - 8.07 and 10.09	> 150
DF	8.0	0.130 - 10.09	> 150

the vessel (i.e., the downstream pressure of the flow controller). A large upstream-downstream pressure difference ($\Delta P_{Up-Down}$) can introduce control problems for the fuel/air/N_2 flows and consequently flame instabilities. It is observed that the fuel MFC is much more sensitive to the inlet pressure than the gas MFC's. During the experiments, $\Delta P_{Up-Down} \cong 8$ bar caused the flames to jump and/or pulsate. When the inlet pressure was decreased to $\Delta P_{Up-Down} \cong 3$ bar the flame became stable for a larger set of flow conditions.

Liquid fuel variability effect on flame stability

Besides the experiments with n-heptane described above, flames from n-heptane/iso-octane blends with the following liquid fuels were also realized: cyclohexanol, cyclohexane, cyclohexanone, n-hexane and 1-hexanol (see table 2.4 for the blend compositions). These blends are part of a stepped approach study (see section 1.2 in chapter 1) on the effect of oxygenated fuels on soot formation across different experimental setups. They were burnt in a modified engine setups where exhaust soot emission is measured. The aim of studying these blends (or other automotive surrogates fuels) also in laminar burners is to isolate fuel chemistry effects from changes in flame lift-off length, temperature, pressure, etc., that may be caused by both physical and chemical effects. The preliminary studies carried out using the HPVB setup can be found in [41, 42].

Table 2.4: Composition of the liquid fuels blends.

Blend number	Fuel A [%Vol.]	Fuel B [%Vol.]	Fuel C [%Vol.]
1	n-heptane [44.9%]	iso-octane [30.3%]	n-hexane [24.8%]
2	n-heptane [68.9%]	iso-octane [5.8%]	cyclohexane [25.3%]
3	n-heptane [59.1%]	iso-octane [12.8%]	1-hexanol [28.1%]
4	n-heptane [62.3%]	iso-octane [13.7%]	cyclohexanol [24.0%]
5	n-heptane [65.4%]	iso-octane [10.5%]	cyclohexanone [24.1%]

The flame stability was observed at a range of temperatures (CEM, heated hose and burner) and flow conditions at atmospheric pressure. The blends containing the

cyclic hydrocarbons were tested first and only the non-oxygenated cyclohexane was stable. The operational conditions for stable flames with the cyclohexane blend were:

- CEM, heated hose and burner temperature at 180 °C.
- Partially premixed flames with premixing air fixed in 0.312 L/min and fuel varying up to 6.5 g/h.
- Diffusion flames: nitrogen flow = 0.104 L/min, fuel flow = 6 and 5 g/h; nitrogen flow = 0.130 L/min, fuel flow = 6.5 and 7.0 g/h.

The flames of the blend with cyclohexanol showed very strong instabilities with the flame expanding and contracting for all conditions tested. The flames from the blend containing cyclohexanone were unstable at all conditions. The ball valves in the fuel line got stuck and it was no longer possible to open/close them. It is thought that cyclohexanone reacted with the material of the ball valves carrying impurities to the evaporator system (CEM), influencing negatively the device performance and the flame stability. The system was purged with nitrogen for several hours, but no stable flame could be realized for the other blends and pure n-heptane. The CEM and the ball valves were replaced.

In order to prevent future damage to the system (specially the evaporator) during the studies with oxygenated or more aggressive fuels, it is advised to apply the doped flame approach where only a small amount of these fuels is added to the fuel line after the evaporator.

Elevated pressures - n-heptane

For both diffusion and partially premixed n-heptane flames, soot luminosity increases and flame shape changes are observed already at 0.2 MPa . Soot that initially is formed in the flame tip at atmospheric pressure is observed to be formed earlier, upstream in the flame, when pressure is increased. The blue region in the flame base at atmospheric pressure completely turns into a sooting region for pressures higher than 0.5 MPa (see figures 2.15 and 2.16).

The diffusion flame instabilities start already at pressures slightly above atmospheric when the vessel is closed. The flame flickering and oscillations instabilities increase fast with pressure. Good flame stability could only be achieved for partially premixed flames below 0.3 MPa. However, when the pressure is around 0.3 MPa the flame seems to start rotating and pulsating. Further increase in pressure worsens these instabilities. Flame rotation speed increases and the rotating cells start in the flame base and grow towards the flame tip until they break the flame envelop in a sooting tip.

A stable laminar n-heptane flame at atmospheric pressure can be created for a large set of flow conditions. However, the stability will depend on the settings of several parameters of the experimental setup as described. The effect of these parameters on the flame stability also varies if the flame is a diffusion flame or partially premixed flame. The flames become more susceptible to instabilities when pressure

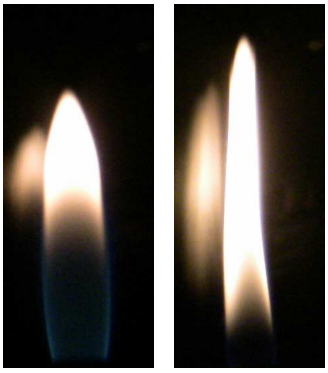

(a) 0.10 MPa (b) 0.35 MPa

Figure 2.15: Diffusion n-heptane flames at pressures of 0.1 and 0.35 MPa. Fuel flow = 6.0 g/h and carrier gas (N_2) = 0.13 L/min.

(a) 0.10 MPa (b) 0.20 MPa (c) 0.30 MPa (d) 0.50 MPa (e) 0.70 MPa

Figure 2.16: Partially premixed n-heptane flames at different elevated pressures. Fuel flow = 4.5 g/h and premixed air = 0.22 L/min.

is increased and no long term stability has been observed for pressures higher than 3 bar. During the stabilities tests discussed in this section some design modifications were implemented to improve stability and are described in the following section.

2.5.3 Design improvements for flame stability

For the tests at elevated pressures the chimney is placed on top of the vessel, initially leaving one corner hole opened for flame ignition (figure 5.1). Once ignited , an attempt is made to close the vessel but the flame starts to become very unstable with very strong up- and down-stream oscillation and sudden blow-off. Due to the small volume of the vessel, the pressure inside will always be slightly above atmospheric even with the minimal fuel and oxidizer flow needed to light a flame.

Combustion instabilities in closed systems such as a combustion chamber, is a subject that has been investigated for decades in the thermo-acoustic field. The behavior of a system including a combustion chamber is governed by the basic variables: (a) air/fuel ratio, (b) flame characteristics and (c) system geometry. Each of these variables can actively affect the instability of the system. In order to characterize such instabilities, several problems must be investigated, such as the effect of the excited system parts on the total response of the system, the generation of instabilities by the flame and coupling into the feedback system and the effects of the chamber volume on instabilities, among others. These components of the system can be excited by modifying one or a combination of any of the basic system variables.

An experimental investigation of the exact mechanism which drives the combustion oscillations observed in the present experimental setup was considered very complex and time consuming. Therefore, the first approach was to find a solution to damp the flame oscillations. During the tests conducted to find the solution, three instability dampers an orifice, one-way-valve and a buffer placed in the fuel line appeared to be successful. They are described below in the section "Instability-dampers".

The problem with water droplet formation on the fuel tip surface at elevated pressure is addressed in the section "Water-condensation".

Instability dampers

Pressure waves generated in the vessel might be traveling upstream in the fuel line causing the fuel flow, and therefore the flame, to strongly oscillate up and down. A small orifice was introduced in the fuel line to create high flow velocities near the sonic velocity. When velocities near the sonic velocity (also known as chocked velocity) are achieved, pressure waves generated in the pressure vessel do not travel upstream in the fuel line.

In order to determine what is the best orifice diameter for our system, we need to know what is the mass flow through an orifice when the sonic velocity is achieved. Sonic velocity occurs when the ratio of the absolute source upstream pressure to the absolute downstream ambient pressure is equal to or greater than $[(\gamma+1)/2]\gamma/(\gamma-1)$,

where γ is the specific heat ratio of the discharged gas. For many gases, γ ranges from about 1.09 to about 1.41, and thus $[(\gamma+1)/2]\gamma/(\gamma-1)$ ranges from 1.7 to about 1.9. This means that chocked velocity usually occurs when the absolute source vessel pressure is at least 1.7 to 1.9 times as high as the receiver vessel pressure. For the case of methane, $\gamma = 1.3$ and the absolute source upstream pressure must be 1.83 for a chocked flow. When the gas velocity is chocked, the equation for the mass flow rate $\dot{m}$ is:

$$\dot{m} = \left[\left(\frac{2\gamma}{\gamma+1}\right)^{\frac{\gamma+1}{2(\gamma-1)}}\right]\left[\frac{P_{up}A_k}{C_0}\right] \tag{2.3}$$

where P_{up} is the absolute upstream pressure, A_k is the orifice area and C_0 is the speed of sound. The mass flow through an orifice in the situation where the flow is chocked was calculated using equation 2.3 for several orifice diameters ranging from 0.1 to 1 mm. The results are shown in Table 2.5 for methane.

Table 2.5: Mass flow through an orifice in chocked flow conditions

$D_{orifice}$ [mm]	Mass Flow rate [g/h]
0.1	11.66
0.2	46.10
0.4	186.44
0.6	419.49
0.8	745.77
1.0	1165.26

The mass flow controller (MFC) for methane used in our experimental setup has a maximum mass flow rate of 13 g/h which was chosen to produce the desirable flame heights. From Table 2.5 it can be seen that the flow through the orifice diameter of 0.1 mm will achieve sonic velocity within the mass flow range of $11 \leq \dot{m} \leq 13$ g/h. Experimental tests were then conducted with the same orifice diameter range. A metal foam was introduced as a flow straightener downstream the orifice to avoid possible flow disturbances due to the high speed flow in the orifice. The fuel tube is made in two parts with an interchangeable tip. When the orifice is introduced in this interchangeable tube tip, the pressure upstream increases and the tube tip is blown away. Therefore, the tests were conducted with a new fuel tube that is made out of only one piece. It was observed that the orifice of 0.1 mm also showed the best results in terms of flame stability even when working below the chocked condition in the mass flow range of $4 \leq \dot{m} \leq 11$ g/h. This approach was successful avoiding flame blow-off and oscillations when the vessel was closed.

The disadvantage of the orifice appears when it is necessary to carry out experiments using different fuel tube material as the ones performed to solve the water condensation problem (see the next section "Water condensation"). Because the fuel tube must be made out of only one piece, the whole burner must be removed from

the vessel to exchange the entire fuel tube. Therefore, it would be cheaper and faster to experiment if only the fuel tube tip could be exchanged. A fuel tube made of two parts can be re-introduced but an alternative to the orifice solution must be found to avoid the fuel tip to detach. This was achieved by placing the one-way-valve in the fuel line upstream the burner. The one-way-valve forces the flow in one direction and therefore it was also efficient in avoiding the oscillatory flow when the vessel is closed.

Another way to damp the flame oscillations is to introduce a buffer of 200 mL in the fuel line between the heated hose and the burner. This solution showed stability improvements when burning n-heptane at atmospheric pressure. A controlled heating tape is wrapped around the buffer to control the temperature, avoiding condensation.

Water condensation

The condensation of water vapor depends mainly on its partial pressure and temperature and very weakly on total pressure. However, the combustion products will mix with the ambient gases in the chamber and the mole fraction of water vapor will depend on the fuel/air ratio. Therefore, the partial pressure of water vapour in the chamber will be proportional to and increase with the total pressure.

In order to decrease the partial pressure of water vapor and avoid condensation, the air coflow rate is increased. Although less condensation is observed on the optical windows of the vessel for increased air flow, the droplets are still formed on the fuel tip. The next attempt to avoid the formation of water droplets considered the temperature of the fuel tip. The fuel tube is made of aluminum which has a high thermal conductivity. Therefore, if the aluminum fuel tip is changed for another material with a lower thermal conductivity, it will keep the heat released by the flame for a longer period. Consequently, the fuel tip will be hotter with a lower thermal conductivity material and possibly avoid water condensation on its surface. Using the interchangeable tube tip, stainless steel and brass were tested and both indeed were successful in avoiding water droplet formation.

Overall, the design modifications described above, extended the range of operational conditions where flames from both gaseous and liquid fuels were stable. However, at elevated pressures, the flame stability of vaporized liquid fuels remains limited as described in this section. Stable methane-air partially premixed flames were achieved up to 2.5 MPa. The flame asymmetry observed for methane-air diffusion flame was solved, which was thought to be caused by the water droplet formation in the fuel tip.

Bibliography

[1] K. Kohse-Höinghaus, U. Meier, and B. Attal-Tretout. Laser-induced fluorescence study of OH in flat flames of 1-10 bar compared with resonance CARS experiments. *Applied Optics*, 29(10):1560–1569, 1990.

[2] V. Bergmann and W. Stricker. H_2 CARS thermometry in a fuel-rich, premixed,

laminar CH_4/air flame in the pressure range between 5 and 40 bar. *Applied Physics B: Lasers and Optics*, 61:49–57, 1995.

[3] C. Schulz, V. Sick, U. E. Meier, J. Heinze, and W. Stricker. Quantification of NO A-X(0,2) laser-induced fluorescence: investigation of calibration and collisional influences in high-pressure flames. *Applied Optics*, 38(9):1434–1443, 1999.

[4] H. Böhm, ChR. Feldermann, Th. Heidermann, H. Jander, B. Lüers, and H.Gg. Wagner. Soot formation in premixed C_2H_4-air flames for pressures up to 100 bar. *Proceedings of the Combustion Institute*, 24:991–998, 1992.

[5] T. Heidermann, H. Jander, and H. G. Wagner. Soot particles in premixed C_2H_4-air-flames at high pressures (p=30-70 bar). *Physical Chemistry Chemical Physics*, 1(15):3497–3502, 1999.

[6] J. Sato. Extinction of counterflow diffusion flame in high pressure. *Combustion Science and Technology*, 75:103–113, 1990.

[7] C. G. Fotache, T. G. Kreutz, and C. K. Law. Ignition of counterflowing methane versus heated air under reduced and elevated pressures. *Combustion and Flame*, 109(4):442–470, 1997.

[8] D. X. Du, H. Wang, and C. K. Law. Soot formation in counterflow ethylene diffusion flames from 1 to 2.5 atmospheres. *Combustion and Flame*, 113(1-2): 264–270, 1998.

[9] C.S. McEnally, A.M. Schaffer, M.B. Long, D. Pfefferle, M.D. Smooke, M.B. Colket, and R.J. Hall. Computational and experimental study of soot formation in a coflow, laminar ethylene diffusion flame. *The Combustion Institute*, 27th symposium on Combustion:1497–1505, 1998.

[10] K.T. Walsh, J.F ielding, M.D. Smooke, and M.B. Long. Experimental and computational study of temperature, species, and soot in buoyant and non-buoyant coflow laminar diffusion flames. *Proceedings of the Combustion Institute*, 28: 1973–1979, 2000.

[11] C.S. McEnally, L.D. Pfefferle, A.M. Schaffer, M.B. Long, R.K. Mohammed, M.D. Smooke, and M.B. Colkei. Characterization of a coflowing methane/air non-premixed flame with computer modeling, Rayleigh-Raman imaging, and on-line mass spectrometry. *Proceedings of the Combustion Institute*, 28(2063-2070), 2000.

[12] M.D. Smooke, R.J. Hall, M.B. Colket, J. Fielding, M.B. Long, C.S. McEnally, and L.D. Pfefferle. Investigation of the transition from lightly sooting towards heavily sooting co-flow ethylene diffusion flames. *Combustion Theory and Modelling*, 8: 593–606, 2004.

[13] M.D. Smooke, C.S. McEnally, L.D. Pfefferle, R.J. Hall, and M.B. Colket. Computational and experimental study of soot formation in a coflow, laminar diffusion flame. *Combustion and Flame*, 117(117-139), 1999.

[14] M.D. Smooke, M.B. Long, B.C. Connelly, M.B. Colket, and R.J. Hall. Soot formation in laminar diffusion flames. *Combustion and flame*, 143:613–628, 2005.

[15] I. M. Miller and H. G. Maahs. High-pressure flame system for pollution studies with results for methane-air diffusion flames. *NASA Technical Paper*, TN D-8407, 1977.

[16] W. Lee and Y. D. Na. Soot study in laminar diffusion flames at elevated pressure using two-color pyrometry and Abel inversion. *JSME Int. Journal Series B*, 43 (4):550–555, 2000.

[17] K.A. Thomson. *Soot Formation in Annular Non-premixed Laminar Flames of Methane-Air at Pressures of 0.1 to 4.0 MPa*. PhD thesis, University of Waterloo, 2004.

[18] C.S. McEnally, L.D. Pfefferle, B. Atakan, and K. Kohse-Höinghaus. Studies of aromatic hydrocarbon formation mechanisms in flames:progress towards closing the fuel gap. *Progress in Energy and Combustion Science*, 32:247–294, 2006.

[19] E. Zervas. Formation of organic acids from propane, isooctane and toluene/isooctane flames. *Fuel*, 84(6):691 – 700, 2005.

[20] E. Zervas, S. Poulopoulos, and C. Philippopoulos. Formation of oxygenated compounds from isooctane flames. *Fuel*, 85(3):333 – 339, 2006.

[21] F. Inal and S.M. Senkan. Effects of equivalence ratio on species and soot concentrations in premixed n-heptane flames. *Combustion and Flame*, 131(1-2):16 – 28, 2002.

[22] F. Inal and S. Senkan. Effects of oxygenate additives on polycyclic aromatichydrocarbons (PAH's) and soot formation. *Combust. Sci. and Tech*, 174(9):1–19, 2002.

[23] P. Berta, I.K. Purib, and S.K. Aggarwal. Structure of partially premixed n-heptaneair counterflow flames. *Proceedings of the Combustion Institute*, 30:447–453, 2005.

[24] P. Berta, S.K. Aggarwal, and I.K. Purib. An experimental and numerical investigation of n-heptane/air counterflow partially premixed flames and emission of NO_x and PAH species. *Combustion and Flame*, 145:740–764, 2006.

[25] C.S. McEnally and L.D. Pfefferle. Improved sooting tendency measurements for aromatic hydrocarbons and their implications for naphthalene formation pathways. *Combustion and Flame*, 148:210–222, 2007.

[26] C.S. McEnally and L.D. Pfefferle. Decomposition and hydrocarbon growth processes for hexadienes in nonpremixed flames. *Combustion and Flame*, 152:469–481, 2008.

[27] C.S. McEnally and L.D. Pfefferle. Sooting tendencies of nonvolatile aromatic hydrocarbons. *Proceedings of the Combustion Institute*, 32:673–679, 2009.

[28] A. Hamins, D.T. Anderson, and J.H. Miller. Mechanistic studies of toluene destruction in diffusion flames. *Combustion Science and Technology*, 71:175–195, 1990.

[29] G. Intasopa. Soot measurements in high-pressure diffusion flames of gaseous and liquid fuels. Master's thesis, Graduate Department of Aerospace Science and Engineering, University of Toronto, 2011.

[30] C.S. McEnally and L.D. Pfefferle. The effects of dimethyl ether and ethanol on benzene and soot formation in ethylene nonpremixed flames. *Proceedings of the Combustion Institute*, 31(1):603–610, 2007.

[31] J. Wu, K.H. Song, T. Litzinger, S.-Y. Lee, R. Santoro, M. Linevsky, M. Colket, and D. Liscinsky. Reduction of PAH and soot in premixed ethyleneair flames by addition of ethanol. *Combustion and Flame*, 144:675–687, 2006.

[32] R.G. Wylie and R.S. Fisher. Molecular interaction of water vapor and air. *J. Chem. Eng. Data*, 41(1):133–142, 1996.

[33] R.G. Wylie and R.S. Fisher. Molecular interaction of water vapor and oxygen. *J. Chem. Eng. Data*, 41(1):175–180, 1996.

[34] C.C.M. Luijten. *Nucleation and droplet growth at high pressure*. PhD thesis, Technische Universiteit Eindhoven, ISBN: 90-386-0747-4, 1998.

[35] A. Vranos. Influence of film boiling on the thermal decomposition of vaporizing n-hexadecane. *Industrial and Engineering Chemistry Product Research and Development*, 20:167–169, 1981.

[36] A. Vranos. Decomposition of vaporizing n-hexadecane. *Combustion and Flame*, 30:151–161, 1977.

[37] P. Stobakk. Multi-component fuel evaporator. Project report, University of California, San Diego, 1999.

[38] K.A. Thomson, O.L. Gülder, E.J. Weckman, R.A. Fraser, G.J. Smallwood, and D.R. Snelling. Soot concentration and temperature measurements in co-annular, nonpremixed CH_4/air laminar flames at pressures up to 4 MPa. *Combustion and Flame*, 140:222–232, 2005.

[39] FLUIDAT® on the Net V1.18/5.70, Bronkhorst High-Tech B.V., Ruurlo, The Netherlands. *Available at: www.fluidat.com.*

[40] H. Gohari Darabkhani, J. Bassi, H.W. Huang, and Y. Zhang. Fuel effects on diffusion flames at elevated pressures. *Fuel*, 88:264–271, 2009.

[41] P.A.M. Bertrand. Soot formation of lignin derived fuels in a laminar co-flow diffusion flame. Master's thesis, Eindhoven University of Technology - TU/e. Report number: WVT2009.09, 2009.

[42] L. Zhou, N.J. Dam, M.H. de Andrade Oliveira, C.C.M. Luijten, C.A.J. Leermakers, M.D. Boot, and L.P.H. de Goey. Laser diagnostics of soot formation by alternative fuels. In *Proceedings of the Summer School: "Energy and Materials from the Sun"*, pages 1–16, Kerkrade, The Netherlands, June 2011. European Graduate School - EGS.

CHAPTER 3

Laser diagnostic techniques

The following sections describe the theory behind the laser diagnostic techniques used in the measurements of soot volume fraction and qualitative profiles of polycyclic aromatic hydrocarbons (PAH's) and hydroxyl radicals (OH), reported later in this thesis. The theoretical background of the LOSA (Line-of-Sight Attenuation) technique will be discussed in section 3.1 while the LII (Laser-Induced Incandescence) and LIF (Laser-Induced Fluorescence) techniques are discussed in section 3.2. These techniques are applied in laminar flames from gaseous and liquid fuels in chapter 4 (LOSA) and chapters 5 and 6 (LII and LIF), formatted as articles. Therefore, a detailed description of the respective optical setups and measurement procedures can be found therein.

3.1 Line-of-Sight Attenuation (LOSA)

LOSA is a relatively simple and straightforward diagnostic technique that has been frequently used for quantification of soot volume fraction in flames [1–18]. Its principle is based on the extinction of light by a medium. When a light beam is attenuated by a medium, the intensity decrease of the light beam can be linked to the volume fraction of particles in the medium (see figure 3.1). In an axisymmetric system, two dimensional spatially resolved soot volume fractions can be obtained using LOSA in combination with inverse Abel transformation [12, 13].

The light extinction passing through the sooting flame is caused by two phenomena, namely scattering and absorption. Scattering is determined by the scattering factor Q, given by

$$Q = \frac{\pi^4}{4\lambda^4} d^6 f(m, N), \tag{3.1}$$

where λ is the wavelength of the light, d is the diameter of the scattering particle, f is a function depending on m, the complex refractive index of the soot particle and N is

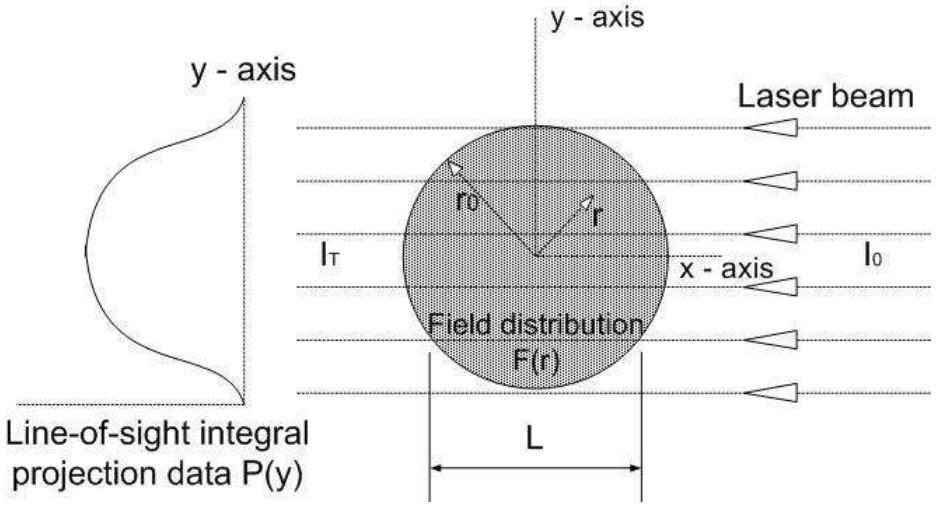

Figure 3.1: Scheme of an extinction measurement.

the particle number concentration. The absorption is determined by the absorption coefficient K_{abs}:

$$K_{abs} = \frac{\pi^2}{\lambda} E(m) N d^3 \tag{3.2}$$

with

$$E(m) = -Im\{\frac{m^2 - 1}{m^2 + 2}\}, \tag{3.3}$$

where $E(m)$ is the soot refractive index function. It can be noticed that the scattering factor is related to d^6/λ^4 while the absorption factor is related to d^3/λ implying that when d/λ is small, $K_{abs} \gg Q$ and, therefore, the influence of scattering can be neglected. The domain where scattering can be neglected is called the Rayleigh regime [6, 7] and it is given by

$$\frac{\pi d}{\lambda} \leq 0.3. \tag{3.4}$$

In moderately sooting flames and in the lower half of heavily sooting flames, the soot particles are considered to be in the early stage of soot formation and small enough to use the Rayleigh assumption [12, 19]. An experimental extinction coefficient can be calculated by measuring the transmitted light intensity I_T, the incident light intensity I_0 and the absorption length L in the flame:

$$K_{ext} = \frac{1}{L} \ln \frac{I_0}{I_T}. \tag{3.5}$$

If the soot particles are small enough to be in the Rayleigh regime, the absorption coefficient is equal to the extinction coefficient. By assuming the soot particles to be spherical, the soot volume fraction f_v can be calculated with

$$f_v = \frac{\pi}{6} N d^3. \tag{3.6}$$

Combining equation (3.6) with equations (3.5) and (3.2), this results in

$$f_v = \frac{\lambda}{k_e} K_{ext} \tag{3.7}$$

with

$$k_e = 6\pi(1 + \alpha_{sa})E(m). \tag{3.8}$$

The parameter k_e is the dimensionless optical extinction coefficient and α_{sa} is the scatter to absorption ratio. The parameter α_{sa} is only considered when the influence of scattering is taken into account. In order to estimate α_{sa}, knowledge of the morphology of the soot and multi-angle scatter measurements are required. When this information is not available, the scatter to absorption ratio is normally assumed to be $\alpha_{sa} \simeq 0$ which is a reasonable assumption for particles in the Rayleigh regime. Thomson [12] assumed α_{sa}=0.05 but with an uncertainty of 100%. Other authors report values of α_{sa} varying from 0.01 to 0.3 [11, 18, 20, 21].

Many different values for the soot refractive index m are found in literature. The work of Smyth et al. [22] presents an extensive debate about the most widely used value for the soot refractive index, $m = 1.57 - 0.56i$. According to Smyth et al. [22], this value is based on a misinterpretation of the work of Dalzell and Sarofim [23]. Actually, they have reported $m = 1.56 - 0.46i$ for acetylene and $m = 1.57 - 0.50i$ for propane flames at visible wavelengths. Other m values found in literature are $1.75 - 1.03i$ for a wavelength of 635 nm [18] and $m = 1.90 - 0.55i$ [24]. Chang et al. [25] suggest that the appropriate values of refractive index as a function of wavelength are given by

$$m = n - ik, \tag{3.9}$$

$$n = 1.811 + 0.1263\ln(\lambda) + 0.027\ln^2(\lambda) + 0.0417\ln^3(\lambda), \tag{3.10}$$

$$k = 0.5821 + 0.1213\ln(\lambda) + 0.2309\ln^2(\lambda) - 0.01\ln^3(\lambda). \tag{3.11}$$

When m is calculated for $\lambda = 632.8$ nm (which is the wavelength of the laser used in our LOSA measurements), this results in $m = 1.755 - 0.576i$. This value is also used by Kunte [13]. Not in all publications reporting refractive indices, a wavelength is specified. Furthermore, if it is specified, values are often contradicting.

The parameters m and α_{sa} define the dimensionless optical extinction coefficient k_e. Zhu and co-workers [26] claim to present the first fuel-specific data of k_e available in the near-IR spectrum (at 543.5, 632.8, 856, 1314 and 1565 nm). They combined Transmission Electron Microscopy (TEM) and optical microscopy analyses to evaluate soot morphology in acetylene and ethene laminar diffusion flames. The reported k_e values range from 7.95 ± 0.44 to 10.0 ± 0.8 and, specifically for 632.8 nm, from 8.12 ± 0.44 to 9.65 ± 0.40. They pointed out that their measured k_e values are much larger than the calculated ones using reported values of the refractive index and the Rayleigh theory which normally ranges from 2.69 to 4.87 for a wavelength of 632.8 nm.

Krishnan et al. [20, 21] measured optical properties of soot at visible wavelengths (351.2-800.0 nm) in several gaseous (acetylene, ethylene, propylene and butadiene) and liquid (benzene, cyclohexane, toluene and n-heptane) fuel flames. Dimensionless extinction coefficients were relatively independent of fuel type and wavelength (for wavelengths in the range of 400-800 nm) yielding a mean value of $k_e = 8.4$ ($\pm$ 1.5). In these publications, k_e was measured in the over-fire (or post-flame) region and not in the flame. However, Williams et al. [18] measured k_e using a small extractive sampling probe to withdraw soot from ethylene and kerosene diffusion flames. Their in-flame values were in the range of 9 to 10, similar to the results from previous studies of post-flame soot. The work of Shaddix et al. [27] in laminar ethylene diffusion flames and a JP-8 (kerosene-based jet fuel) pool fire supports the recent measurements of k_e suggesting that the optical absorptivity of agglomerating soot shows only minor variations for different fuels and flame types.

Based on the discussions above, no calculation of k_e using $E(m)$ and α_{sa} is made. Instead, and considering the possibility to use the experimental setup developed in this work to a large range of fuels, the mean value of $k_e = 8.4$ ($\pm$ 1.5) reported by Krishnan et al. [20] will be used. An exception is made if a specific comparison of soot volume fraction with reported values in literature is necessary. This was the case during the validation of the LOSA technique in our burner when soot measurements in ethylene flames are compared to the work of Smooke et al. [28] using $k_e = 10$.

Inverse Abel transformation

The logarithm of the incident laser intensity divided by the transmitted laser intensity determines the line-of-sight integral projection data

$$P(y) = \ln\left(\frac{I_0}{I_T}\right). \tag{3.12}$$

In order to convert line-of-sight integral projection data of an axisymmetric measurement field into a spatially resolved distribution $F(r)$, in this case spatially resolved K_{ext}, and subsequently soot volume fraction (see equation 3.7), inverse Abel transformation is applied:

$$F(r) = -\frac{1}{\pi}\int_{y=r}^{y=y_{max}} \frac{P'(y)}{\sqrt{y^2 - r^2}}\, dy. \tag{3.13}$$

Numerically, the integral is replaced by a summation with segments between points y_i and P' is considered to be constant between these points. This leads to

$$F(r) = \sum_{y_i=r}^{y_i=y_{max}} -\frac{1}{\pi}P'(y_i)\int_{y=y_i}^{y=y_i+y_{step}} \frac{dy}{\sqrt{y^2 - r^2}}, \tag{3.14}$$

in which the integral can be evaluated analytically, and the derivative $P'(y_i)$ is obtained from the measurements.

In order to verify whether the inverse Abel transformation was performed correctly, Abel transformation is applied to the calculated spatially resolved K_{ext} (equation 3.14) to obtain back the measured line-of-sight K_{ext}. Comparison between this recalculated line-of-sight K_{ext} and the original measured data showed deviations typically much smaller than 10%.

3.2 Laser-Induced Incandescence (LII) and Fluorescence (LIF)

OH radicals play an import role in the soot oxidation mechanism. Polycyclic aromatic hydrocarbons (PAH's) are well known as soot precursors. Therefore, along with soot concentration measurements, their characterization is of great importance to elucidate soot formation and oxidation mechanisms. First, the working principles of the laser techniques are described, followed by a review of the combined approaches found in literature to measure soot, PAH and OH.

3.2.1 Laser-Induced Incandescence - LII

The LII technique allows measurements of a 2D soot volume fraction field and soot particle size and has been widely applied in combustion studies. When soot particles are heated by a laser to temperatures above 4000 K, they will emit radiation according to the Planck distribution law in a broad wavelength range. Soot radiation is also naturally emitted from hot soot particles in a flame. However, the intensity of the radiation emitted by laser heated soot particles will be much higher than the radiation emitted at a normal flame temperature (1500-2000 K) and it is displaced towards short wavelengths, see figure 3.2(a). Therefore, the background flame luminosity can be efficiently suppressed by detecting short wavelengths. The intensity of the radiation can be linked to a certain soot volume fraction and the temporal behavior of the radiation decay relates to the soot particle size. A typical LII setup is composed by a Nd:YAG laser used at 1064 nm or 532 nm, laser sheet forming optics (combinations of spherical and cylindrical lenses) and an ICCD camera as the detector, equipped with a short-pass filter that transmits shorter wavelengths than $\sim$ 450 nm.

The physical processes present in generating the LII signal are very complex and involve particle heating by laser absorption, vaporization, heat conduction to the surrounding atmosphere, oxidation, thermal annealing and others [29, 30]. Many attempts have been made to model these processes in order to analyze LII data, specially for time-resolved signals for primary particle size measurements. A comprehensive comparison of LII models can be found in Schulz et al. [31] and references therein. A wide variability in both model predictions and experimental results is observed. Schulz concluded that despite the widespread application of LII for soot-concentration and particle-size measurements, more research is necessary to overcome the significant lack in fundamental understanding of many of the underlying physical processes.

Due to a complex interplay of the physical processes mentioned above, there is a LII signal dependence on laser fluence, being the laser pulse energy divided by the cross section area of the beam at the measurement point. If the laser pulse energy is changed and the laser fluence calculated, a curve as in figure 3.2(b) is obtained. At low laser fluences the LII signal increases with the laser fluence due to the fact that a bigger part of the laser sheet will be able to heat the soot particles to a high temperature. Above 0.2 J/cm^2 the LII signal reaches more or less a constant level (a plateau region) and at least part of the soot particles will be affected by vaporization, which will result in a loss of signal for increasing laser pulse energy. A normal LII-experiment is operated at a fluence around the knee.

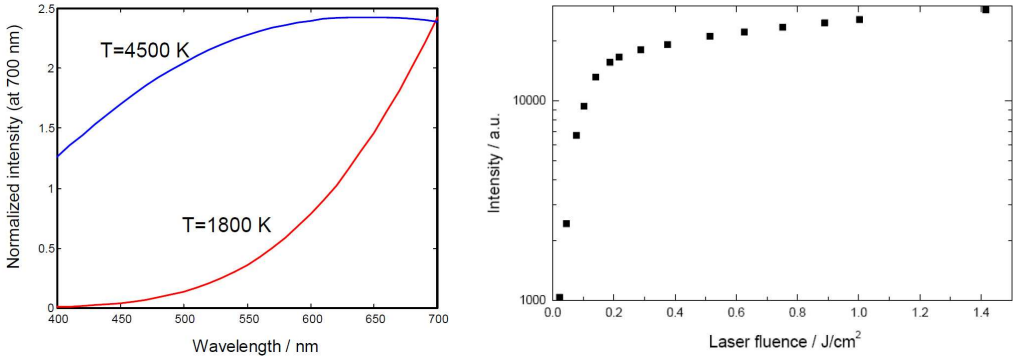

(a) (b)

Figure 3.2: Planck spectral distribution normalized at 700 nm and depicted only in the visible spectral range (a). Fluence curve for a LII-measurement (b). Figures extracted from [32].

To obtain quantitative results from LII, the measurements must be calibrated. A common way of calibrating a LII measurement for soot volume fraction measurements is applying the extinction measurements to a well characterized flame. Normally a stable partially premixed flat flame is used where the pathlength of the laser and the equivalence ratio (ϕ) is known. In case of soot particle sizes evaluated from the LII decay, the calibration is usually done using thermophoretic sampling and the transmission electron microscopy (TEM) technique. Therefore, the uncertainties in the calibration method will be transferred to the LII method. Other sources of uncertainties are related to the optical properties of the soot particles, excitation and detection wavelengths, laser fluence and spatial beam profile [31].

3.2.2 Laser-Induced Fluorescence - LIF

The laser-induced fluorescence (LIF) technique is largely used in combustion diagnostics due to several characteristics: high sensitivity, high spatial resolution, species specificity and applicability in harsh environments [33]. The technique is based on the excitation of atoms or molecules from a lower energy state to a higher excited state using a laser source. The excited atom or molecule re-emits radiation after a short

time. From this emitted radiation it is possible to deduce information on both temperature and concentration. Because it is possible to probe very specific vibrational and rotational levels, LIF has considerable selectivity. LIF can measure 2D temperature fields and species distributions of atoms (O, H, N, C) and diatomic molecules (NO, OH, CH, CN, C_2, O_2, CO, H_2). However, LIF suffers from quenching (i.e. collisional deexcitation) and quantitative species concentration measurements are not trivial. In order to relate the signal to an absolute number density scale, quenching correcting calculations and calibration procedures (e.g., absorption, Rayleigh and Raman scattering) must be performed [33, 34].

The main interest in the application of the LIF technique in this PhD thesis is the qualitative measurements of OH and PAH. The OH radicals are important in the overall combustion reactions. It is one of the most important chemical intermediates participating in the oxidation of CO to form CO_2. There is a strong link between the maximum temperature and the maximum OH concentration in flames and it is a marker for the spatial location of the flame front. Several studies strongly suggest that OH dominates the soot surface oxidation process in subatmospheric (0.01-0.1 MPa) [35], atmospheric [36] and elevated pressures (up to 0.8 MPa) conditions [37]. The most used approach to measure OH is to use a tunable dye laser (283 − 284 nm) to excite the $Q_1(8)$ transition near 283 nm in the v" = 0, v' = 1 band of the $A^2\Sigma - X^2\Pi$ system. This transition system is convenient due to its weak dependence on temperature, which is known to vary less than 5% over the temperature range 1400-2100 K. The same approach is used in this thesis to measure qualitative OH profiles and a description of the optical setup can be found in the chapters 5 and 6.

Although some polyatomic species (NH_3, H_2O, HCO, CH_2O) can also be measured with LIF, quantification of PAH using the LIF technique has been very difficult and only relative concentration measurements in flames are normally reported in the literature using this technique [38–42].

3.2.3 Combined LII/LIF - Review

The detection gate used in the LII technique has a significant impact on the accuracy of soot volume fraction measurements. Because soot is a broad-band absorber, excitation wavelengths in the UV (266 nm), visible (532 nm) or IR (1064 nm) can be used for LII detection. The mostly used wavelengths are 1064 nm and 532 nm generated by Nd:YAG lasers. However, if wavelengths in the visible and UV regions are used, possible interference from PAH's and electronically excited C_2 fragments is greatly increased as compared to 1064 nm excitation [43, 44]. Emissions from C_2 and PAH decay quickly and their interference occurs only during the laser pulse. One strategy to avoid these interferences with the LII signals, as suggested by Cignoli [45], is the delayed detection approach where the LII signal is detected after the laser pulse. However, the prompt LII has shown a higher proportionality to soot volume fraction than the delayed signal [32, 44]. Also, long or delayed detection gates bias the LII signal towards large particles since smaller particles cool faster than large ones (see [31] and references therein). Therefore, LII signals in soot volume fraction measurements are normally collected using a detector synchronized with the laser pulse and detection gates around 50 ns.

A way to unambiguously identify the spatial location of PAH's and soot is to compare 2D laser-induced emission images using either 1064 nm or 266 nm as excitation light as demonstrated by Vander Wal [46–48]. Figure 3.3 shows a simultaneous LIF-LII image of a fiber-supported burning fuel droplet. The picture in the left is obtained upon excitation using 266 nm and the right picture is the LII image using 1064 nm. While 1064 nm does not produce molecular fluorescence in the visible region, the 266 nm excitation wavelength is known to result in a broad band fluorescence from large combustion species. Therefore, a comparison between the images in figure 3.3 indicates that the signal on the base of the flame observed upon 266 nm excitation is likely to be LIF from PAH's. A dark region between the LIF-LII signals can also be observed and transmission electron microscopy (TEM) was used to characterize the material from within this region. The results suggested that a fundamental change in the material chemical/physical properties occurs in the dark region indicating a conversion between soot-precursors and solid carbonaceous soot particles.

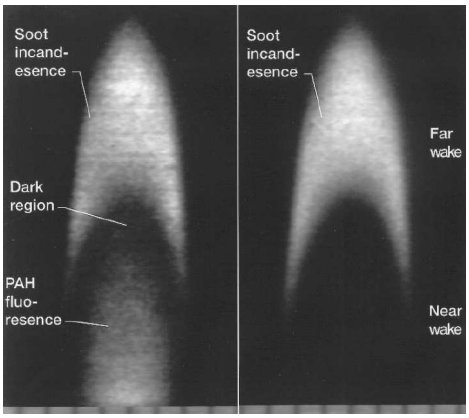

Figure 3.3: Simultaneous LIF-LII image of a fiber-supported burning fuel droplet (n-decane) produced by 266-nm excitation (left) and LII image of a similar droplet using 1064-nm excitation light (right). Figure extracted from Vander Wal [46].

While soot particles in flames can be quantified using calibrated LII signals, there is no feasible method to quantify PAH's from LIF signals. The spectral profile of aromatic substances in gas phase are broadband and change with temperature, making the spectral distinction of different species very difficult. There have been investigations on the possibility to discriminate between different PAH's by means of a temporal evolution of the fluorescence emission (see Ossler et.al. [49, 50] and references therein). They measured temporally resolved fluorescence emissions from gas phase naphthalene, fluorene, anthracene and pyrene in a flow cell at temperatures between 400 and 1200 K using a picosecond laser at 266 nm. They found that lifetimes and spectral profiles are influenced by the density of vibrational states and that the aromatic substances investigated would be chemically unstable in the presence of oxygen at flame temperatures in hydrocarbon flames. The extrapolation of these results in the cell to flame temperatures (1200 1500 K)indicates that a high temporal resolution is required for the discrimination of different PAH's since at flame temperatures lifetimes of the order of tens to hundreds of picoseconds are expected.

Furthermore, studies on the dependence of the fluorescence emission on pressure and excitation wavelength are also pointed out as necessary.

Despite the difficulties in identification and quantification of specific PAH's via fluorescence emission analysis, McEnally and Pfefferle [40] observed a close correlation between the concentration of some PAH species measured with PTMS (photoionization time-off light mass spectrometer) and the maximum intensity of the PAH LIF signals. Besides that, it is possible to relate the emission spectra of PAH fluorescence to their relative sizes. When PAH's are excited at 266 nm it is observed that the emission spectra present two spatially separated bands; one in the UV region and another in the visible region. It has been shown that the UV region emission originates from small aromatic species from 2- to 3-rings and the visible region emission is characteristic of larger aromatic species. When PAH's are excited in the wavelength range of 265-297 nm this emission characteristic does not change much (see [39, 51, 52] and references therein).

Lee et.al. [39] used the second harmonic (532 nm) of a Nd:YAG laser and a narrow band-pass filter (FWHM =10 nm) centered at 400 nm to obtain the LII signal. For PAH-LIF measurements, the excitation wavelength chosen was 283 nm. The distinguished spatial locations of soot and PAH can be seen in figure 3.4(a). The detection wavelength was varied using narrow band pass filter centered at 330, 360, 400, 450 and 500 nm to differentiate the relative size groups of PAH's. It was observed that as the detection wavelength of the PAH-LIF becomes longer, the PAH profile shifts closer to the LII profile (figure 3.4(b)). Since PAH's grow from the fuel side toward the flame and soot particles are formed from PAH's, it was concluded that PAH LIF signals measured at shorter (longer) wavelengths represent relatively smaller (larger) PAH's.

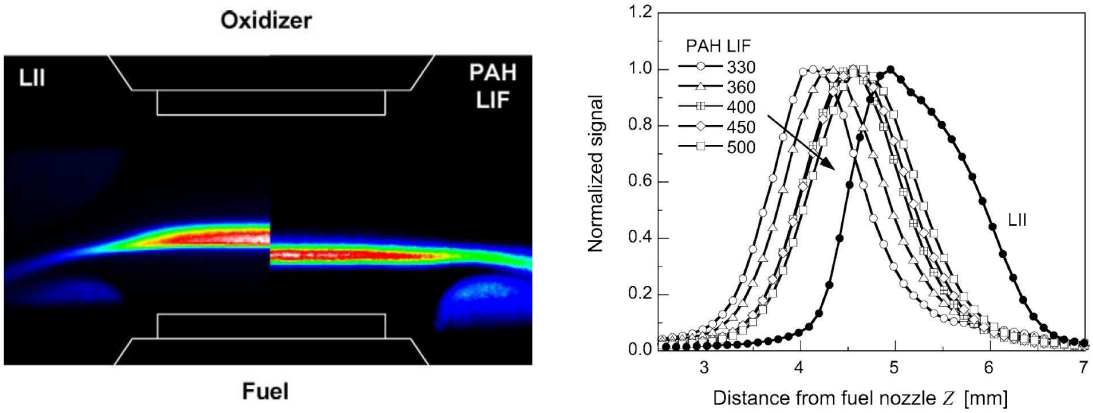

(a) (b)

Figure 3.4: Images of LII (left) and PAH LIF (right) detected at 330 nm (a) and Profiles of LII and PAH LIF signals along the centerline of counterflow for a fuel of 73% ethylene and 27% nitrogen. Figure extracted from Lee et. al. [39].

A combined LIF/LII approach is also applied in chapter 5 and 6 to measure soot

and PAH's in vaporized liquid fuels and doped methane flames. First excitation upon 266 nm is used to collect both PAH-LIF and soot-LII signals in the range of 300 nm to 500 nm with the laser and ICCD camera synchronized (prompt detection). Immediately after the prompt measurement, the spatial location of soot and PAH's is distinguished by delaying the detection with 50 ns. Quantitative soot volume fraction is obtained later by excitation upon 1064 nm and calibration using extinction measurements. In some flames, a combination of filters is used to qualitatively discriminate the relative sizes of PAH's.

Bibliography

[1] K. Mackoand M.A. Mikofski, C. Fernandez-Pello, L. G. Blevins, and R. W. Davis. Laser extincion in laminar inverse diffusion flames. 2005.

[2] L.L. McCrain and W.L. Roberts. Measurements of the soot volume field in laminar diffusion flames at elevated pressures. *Combustion and Flame*, 140:60–69, 2005.

[3] M. Braun-Unkhoff, A Chrysostomou, E. Gutheil P. Frank, R. Lückerath, and W. Sticker. Experimental and numerical study on soot formation in laminar high-pressure flames. *Combustion and Flame*, pages 1565–1572, 1998.

[4] B.F. Kock, B. Tribalet, C. Schulz, and P. Roth. Two-color time-resolved LII applied to soot particle sizing in the cylinder of a Diesel engine. *Combustion and Flame*, 147:79–92, 2006.

[5] M.P.B. Musculus and L.M. Pickett. Diagnostic considerations for optical laser-extinction measurements of soot in high-pressure transient combustion environments. *Combustion and Flame*, 141:371–391, 2005.

[6] C.R. Shaddix and K.C. Smyth. Laser-induced incandescence measurements of soot production in steady and flickering methane, propane, and ethylene diffusion flames. *Combustion and Flame*, 107:418–452, 1996.

[7] C.R. Shaddix, J.E. Harrington, and K.C. Smyth. Quantitative measurements of enhanced soot production in an flickering methane/air diffusion flame. *Combustion and Flame*, 99:723–732, 1994.

[8] K.O. Lee. Soot formation effects of oxygen concentration in the oxidizer stream of laminar coannular nonpremixed methane/air flames. *Combustion and flame*, 121:323–333, 2000.

[9] R.J. Santoro, H.G. Semerjian, and R. A. Dobbins. Soot particle measurements in diffusion flames. *Combustion and Flame*, 51:203–218, 1983.

[10] K.T. Kang, J. Y. Hwang, and S. H. Chung. Soot zone structure and sooting limit in diffusion flames: Comparison of counterflow and co-flow flames. *Combustion and Flames*, 109:266–281, 1997.

[11] B. Yang and U.O. Koylu. Detailed soot field in a turbulent non-premixed ethylene/air flame from laser scattering and extinction experiments. *Combustion and Flame*, 141:55–65, 2005.

[12] K.A. Thomson. *Soot formation in annualr non-premixed laminar flames of methane-air at pressures of 0.1 to 4.0 MPa.* PhD thesis, University of Waterloo, 2004.

[13] S. Kunte. *Untersuchuchen zum Einfluss von Brennstoffstruktur und -sauerstoffgehalt auf die Russbildung und -oxidation in laminaren Diffusionsflammen.* PhD thesis, Eidgenössischen Technischen Hochschule Zürich, 2003.

[14] M.Y. Choi and K.A. Jensen. Calibration and correction of laser-induced incandescence for soot volume fraction measurements. *Combustion and Flame*, 112: 285–491, 1998.

[15] H. Zhao and N. Ladommatos. Optical diagnostics for soot and temperature measurement in diesel engines. *Energy Combustion Science*, 24:221–255, 1998.

[16] F. Liu, K.A. Thomson, and G.J. Smallwood. Effects of soot absorption and scattering on LII intersities in laminar coflow diffusion flames. *Journal of Quantitative Spectroscopy & Radiative Transfer*, 2007.

[17] A. Gomez, M.G. Littman, and I. Glassman. Comparative study of soot formation on the centerline of axisymmetric laminar diffusion flames: Fuel and temperature effects. *Combustion and Flame*, 70:225–241, 1987.

[18] T.C. Williams, C.R. Shaddix, K.A. Jensen, and J.M. Suo-Anttila. Measurement of the dimensionless extinction coefficient of soot within laminar diffusion flames. *Heat and Mass Transfer*, 50:1616–1630, 2006.

[19] P.-E. Bengtsson. Optical diagnostics of soot in flames. Technical report, Lund Institute of Technology, 2007. Lecture notes.

[20] S.S. Krishnan, K.C. Lin, and G.M. Faeth. Extinction and scattering properties of soot emitted from buoyant turbulent diffusion flames. *Journal of Heat Transfer*, 123:331–339, 2001.

[21] S.S. Krishnan, K.C. Lin, and g.M. Faeth. Optical properties is the visible of overfire soot in large buoyant turbulent diffusion flames. *Journal of Heat Transfer*, 122:517–524, 2000.

[22] K.C. Smyth and C.R. Shaddix. The elusive history of $m = 1.57 - 0.56i$ for the refractive index of soot. *Combustion and Flame*, 107:314–320, 1996.

[23] W.H. Dalzell and A.F. Sarofim. Optical constants of soot and their application to heat-flux calculations. *Journal of Heat Transfer*, 91:100–104, 1969.

[24] S.C. Lee and C.L. Tien. Optical constants of soot in hydrocarbon flames. pages 1159–1166, 1981. 18th symposiom on Combustion.

[25] H. Chang and T.T. Charalampopoulos. Determination of the wavelength dependence of refractive indices of flame soot. *Mathematical and Physical Sciences*, 430:577–591, 1990.

[26] J. Zhu, N.Y. Choi, G.W. Mulholland, S.L. Manzello, L.A. Gritzo, and J. Suo-Anttila. Measurement of visible and near-IR optical properties of soot produced from laminar flames. *Proceedings of the Combustion Institute*, 29:2367–2374, 2002.

[27] C.R. Shaddix, A.B. Palotás, C.M. Megaridis, M.Y. Choi, and N.Y.C. Yang. Soot graphitic order in laminar diffusion flames and a large-scale JP-8 pool fire. *Heat and Mass Transfer*, 48:3604–3614, 2005.

[28] M.D. Smooke, M.B. Long, B.C. Connelly, M.B. Colket, and R.J. Hall. Soot formation in laminar diffusion flames. *Combustion and flame*, 143:613–628, 2005.

[29] H. Michelsen. Understanding and predicting the temporal response of laser-induced incandescence from carbonaceous particles. *Journal of Chemical Physics*, 118:7012–7045, 2003.

[30] H. Bladh and P.-E. Bengtsson. Characteristics of laser-induced incandescence from soot in studies of a time-dependent heat- and mass-transfer model. *Applied Physics B*, 78:241248, 2004.

[31] C. Schulz, B.F. Kock, M. Hofmann, H. Michelsen, S.Will, B. Bougie, R. Suntz, and G. Smallwood. Laser-induced incandescence: recent trends and current questions. *Applied Physics B*, 83:333–354, 2006.

[32] P.-E. Bengtsson. Optical diagnostics of soot in flames. Lecture notes, Division of Combustion Physics, Lund Institute of Technology, 2007. Lecture notes from Course on Optical Diagnostics.

[33] M. Aldén, J. Bood, Z. Li, and M. Richter. Visualization and understanding of combustion processes using spatially and temporally resolved laser diagnostic techniques. *Proceedings of the Combustion Institute*, 33:69–97, 2011.

[34] M. Aldén. Laser-induced fluorescence - General introduction. Technical report, Division of Combustion Physics, Lund Institute of Technology, 2007. Lecture notes from Course on Optical Diagnostics.

[35] C.H. Kim, A.M. El-Leathy, F. Xu, and G.M. Faeth. Soot surface growth and oxidation in laminar diffusion flames at pressures of 0.1-1.0 atm. *Combustion and Flame*, 136:191–207, 2004.

[36] F. Xu, A.M. El-Leathy, C.H. Kim, and G.M. Faeth. Soot surface oxidation in hydrocarbon-air diffusion flames at atmospheric pressure. *Combustion and Flame*, 132:43–57, 2003.

[37] C.H. Kim, F. Xu, and G.M. Faeth. Soot surface growth and oxidation at pressures up to 8.0 atm in laminar nonpremixed and partially premixed flames. *Combustion and Flame*, 152:301–316, 2008.

[38] S.-Y. Lee, S.R. Turns, and R.J. Santoro. Measurements of soot, OH, and PAH concentrations in turbulent ethylene-air jet flames. *Combustion and Flame*, 156: 2264–2275, 2009.

[39] S.M. Lee, S.S. Yoon, and S.H. Chung. Synergistic effect on soot formation in counterflow diffusion flames of ethylene-propane mixtures with benzene addition. *Combustion and Flame*, 136:493–500, 2004.

[40] C.S. McEnally and L.D. Pfefferle. Experimental study of non-fuel hydrocarbons and soot in coflowing partially premixed ethylene/air flames. *Combustion and Flame*, 121:575–592, 2000.

[41] H. Böhm and K. Kohse-Höinghaus. On PAH formation in strained counterflow diffusion flames. *Combustion and Flame*, 124:127–136, 2001.

[42] J. Wu, K. Hoon Song, T. Litzinger, S.-Y Lee, R. Santoro, M. Linevsky, M. Colket, and D. Liscinsky. Reduction of PAH and soot in premixed ethylene-air flames by addition of ethanol. *Combustion and Flame*, 144:675–687, 2006.

[43] P.-E. Bengtsson and M. Aldén. C_2 production and excitation in sooting flames using visible laser radiation: Implications for diagnostics in sooting flames. *Combustion Science and Technology*, 77:307–318, 1991.

[44] P.-E. Bengtsson and M. Aldén. Soot-visualization strategies using laser techniques: Laser-induced fluorescence in C_2 from laser-vaporized soot and laser-induced soot incandescence. *Applied Physics B*, 60:51–59, 1995.

[45] F. Cignoli, S. Benecchi, and G. Zizak. Time-delayed detection of laser-induced incandescence for the two-dimensional visualization of soot in flames. *Applied Optics*, 33:5778–5782, 1994.

[46] R.L. Vander Wal. Soot precursor material: visualization via simultaneous LIF-LII and characterization via TEM. *Twenty-Sixth Symposium (International) on Combustion/The Combustion Institute*, 78:2269–2275, 1996.

[47] R.L. Vander Wal, K.A. Jensen, and M.Y. Choi. Soot precursor material: visualization via simultaneous LIF-LII and characterization via TEM. *Combustion and Flame*, 109:399–414, 1997.

[48] R.L. Vander Wal. Soot precursor carbonization: Visualization using LIF and LII and comparison using bright and dark field TEM. *Combustion and Flame*, 112: 607–616, 1998.

[49] F. Ossler, T. Metz, and M. Aldén. Picosecond laser-induced fluorescence from gas-phase polycyclic aromatic hydrocarbons at elevated temperatures. I. cell measurements. *Applied Physics B*, 72:465, 2001.

[50] F. Ossler, T. Metz, and M. Aldén. Picosecond laser-induced fluorescence from gas-phase polycyclic aromatic hydrocarbons at elevated temperatures. II. flame-seeding measurements. *Applied Physics B*, 72:479, 2001.

[51] F. Beretta, A. D'Alessio, A. D'Orsi, and P. Minutolo. Modeling non-premixed laminar co-flow flames using flamelet-generated manifolds. *Combustion Science and Technology*, 85:455–470, 1992.

[52] L. Petarca and F. Marconi. Fluorescence spectra and polycyclic aromatic species in a n-heptane diffusion flame. *Combustion and Flame*, 78:308–325, 1989.

CHAPTER 4

Soot measurements with LOSA

This chapter presents the soot volume fraction measurements performed with the HPVB setup applying the LOSA technique. The section 4.1 is a paper accepted for the Proceedings of the 4^{th} European Combustion Meeting (ECM) where atmospheric pressure measurements in ethylene-air flames are validated by comparison with data from literature and the first measurement in a vaporized liquid fuel flame (n-heptane) is shown. In section 4.2, soot volume fraction measurements in a methane-air diffusion flame at pressures up to 1.0 MPa are presented and discussed.

4.1 Soot measurements in laminar flames of gaseous and vaporized liquid fuels

A High Pressure Vessel and diffusion Burner (HPVB) were designed, constructed and integrated with an evaporation system, to enable laminar flames studies of gaseous and vaporized liquid fuels. This experimental setup is designed to offer ample optical accessibility for laser diagnostics techniques; its capabilities and specifications are described. Soot volume fraction measurements are performed with line-of-sight attenuation (LOSA) and validated using data of ethylene flames from literature. The first measurements of a vaporized liquid fuel (n-heptane) are reported. A stable laminar n-heptane flame is achieved with a maximum standard deviation in soot volume fraction of 0.04 ppm.

The content of this section has been largely taken from:

M.H. de Andrade Oliveira, C.C.M. Luijten, L.P.H. de Goey. Soot measurements in laminar flames of gaseous and (prevaporized) liquid fuels. *Proceedings of the 4^{th} European Combustion Meeting*, Editors: P. Szentannai and F. Winter, Vienna, Austria (2009).

4.1.1 Introduction

In the present work, it is attempted to build a bridge between the most simple combustion systems that have been studied in literature (laminar atmospheric burners, in which mostly simple, gaseous fuels are burnt) and the much more complex environment that is found in practical combustion engines. This is accomplished by the design and construction of a high pressure vessel and diffusion (co-flow) burner, and integrating this with a commercial evaporation system CEM (Controlled Evaporator Mixer), making it possible to study the combustion at elevated pressures of automotive (bio-) fuels, which are typically liquid at room temperature. A set of gaseous and liquid fuels is selected for soot volume fraction studies, aiming to get new insights into the effects of fuel structure on soot formation. These experiments will also serve the purpose of integrating, debugging and validating the experimental setup, including its use at high pressures (up to 3 MPa). The first experimental approach comprises a characterization of different fuels in terms of soot formation tendency, using the line-of-sight attenuation (LOSA) technique. Future investigations will include an investigation of the pressure effect on soot formation and soot formation/reduction tendency, using different oxygenated fuels blended with more conventional fuels. Further detailed studies will be carried out using advanced laser diagnostic techniques that will be assessed and/or developed for use in a high pressure and sooting environment.

4.1.2 Specific objectives

In this paper, the design of the high pressure burner setup, its capabilities and specification are described. The soot volume fraction measurements performed with LOSA are validated using ethylene flame data from literature. For the first time, according to the author's knowledge, soot volume fraction measurements of a vaporized liquid fuel (n-heptane) performed in a laminar co-flow diffusion burner are presented.

4.1.3 Experimental methods

Pressure vessel, burner and evaporation system

The High Pressure Vessel and Burner (HPVB) were built and connected with an evaporation system, thus forming an experimental setup capable of burning gaseous and vaporized liquid fuels at pressures ranging from atmospheric up to 3 MPa. Both the high pressure vessel and the burner were designed for working pressures up to 3 MPa with a safety factor of eight (to assure safety even in the improbable case of explosion). The external shape of the vessel is cubic, the internal structure is made out of three drilled cylinders through the three axes of the cube, which meet and merge in the center of this cube. The result is a robust and flexible high pressure design, with six access ports and an internal volume of 1.6 liters. Four access ports are used to accommodate quartz windows with a diameter of 50 mm, offering the optical accessibility to apply laser diagnostics techniques. The other two access ports are used to couple a chimney with a sliding glow plug igniter to the top of the vessel, and the burner to the bottom. The vessel also has eight additional holes to insert measurement equipment such as thermocouples and pressure meters, and it is flexible to be adapted to several burner configurations (premixed, non-premixed and partially

premixed burners) and sizes. The HPVB is mounted on an adjustable table allowing vertical movement with an accuracy of 0.1 mm (see figure 5.1).

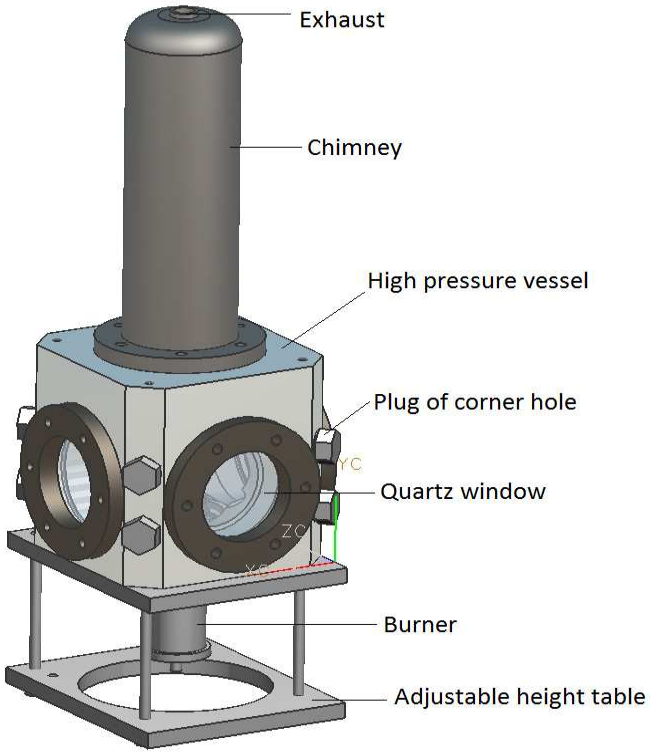

Figure 4.1: Pressure vessel and assembled parts.

The burner dimensions are based on the Long and Smooke burner [1] and its design is adapted to take into account the fit of the burner inside the pressure vessel and the use of the burner at elevated pressures. It is a coflow diffusion burner with a fuel tube inner diameter of 4 mm, an oxidizer coflow inner diameter of 50 mm and a height of 100 mm (see figure 4.2). The fuel nozzle is tapered to reduce recirculation from the burner tip and improves stability of the fluid-ambient interface. Aluminum beads, perforated plates and sintered metal are used as flow straighteners.

The high pressure vessel and burner are integrated with a commercial (Bronkhorst) evaporation system called CEM (Controlled Evaporator Mixer). In this unit, a liquid (fuel) and carrier gas are accurately mixed and then heated. The heating part consists of a heated spiral where the liquid droplets and carrier gas flow through. When the temperature of the heated block is sufficient, the droplets will vaporize. This process results in a stable and accurately controllable fuel vapor/ carrier gas stream. To avoid condensation of the fuel vapor on its way to the burner, an electrically heated tube is used to connect the CEM to the burner. The burner is also heated by an electrically heated ring.

High pressure soot diagnostics

Soot formation has been studied in the literature using both physical probing of the flame and non-intrusive optical techniques. Among the non-intrusive optical tech-

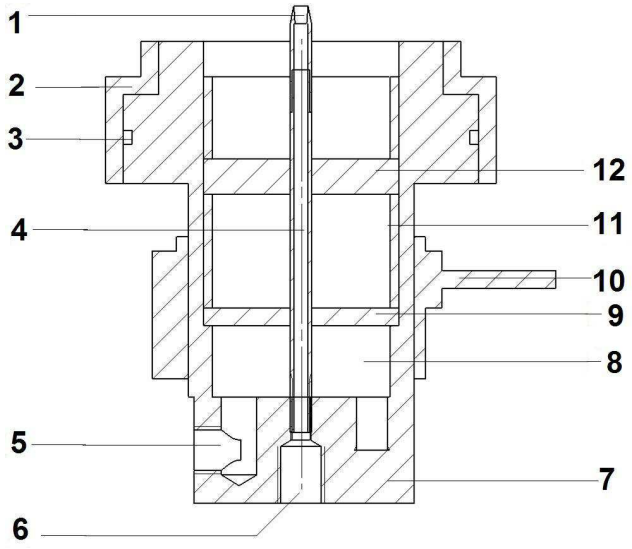

Figure 4.2: High pressure burner assembled parts. 1: Exchangeable fuel tube tip, 2: Teflon isolation ring, 3: Sealing ring, 4: Fuel tube, 5: Co-flow inlet, 6: Fuel inlet, 7: Burner casing, 8: Chamber for aluminum beads, 9: perforated plate, 10: Heated ring, 11: Support ring, 12: Sintered metal.

niques, soot volume fraction has been investigated using a variety of diagnostics including line-of-sight attenuation by soot particles (LOSA), also known as extinction, and laser induced incandescence (LII).

The LII technique allows measurements of a 2D soot volume fraction field and it is able to measure very low soot concentrations. However, in order to give quantitative results, LII must be calibrated using the LOSA technique and it has some drawbacks when used at elevated pressures: soot volume fractions at high pressure are much higher than at atmospheric conditions and signal trapping can occur when the LII signal is attenuated on its way to the camera by soot particles in the flame. Choi and Jensen [2] claim to correct for signal trapping in their measurements, however Liu and co-workers [3] strongly disagree with their method. Liu claims that correction of signal trapping in general is difficult, if not impossible, since it requires knowledge of the distributions of soot volume fraction and the morphology of soot particles.

This stated, and with high pressure application in mind, the LOSA technique was chosen for this work. LOSA is a relatively simple and straightforward diagnostic technique for quantification of soot volume fraction in flames. Its principle is based on the extinction of light by a medium (see figure 4.3). It offers high spatial resolution and does not rely extensively on prior knowledge of physical constants or morphological properties. Several researchers have obtained two dimensional spatially resolved soot volume fractions using LOSA in combination with inverse Abel transformation [4, 5].

Extinction consists of scattering and absorption. Assuming the soot particles small enough to be in the Rayleigh regime given by

$$\frac{\pi d}{\lambda} \leq 0.3, \tag{4.1}$$

where λ is the wavelength of the light and d is the particle diameter, scattering

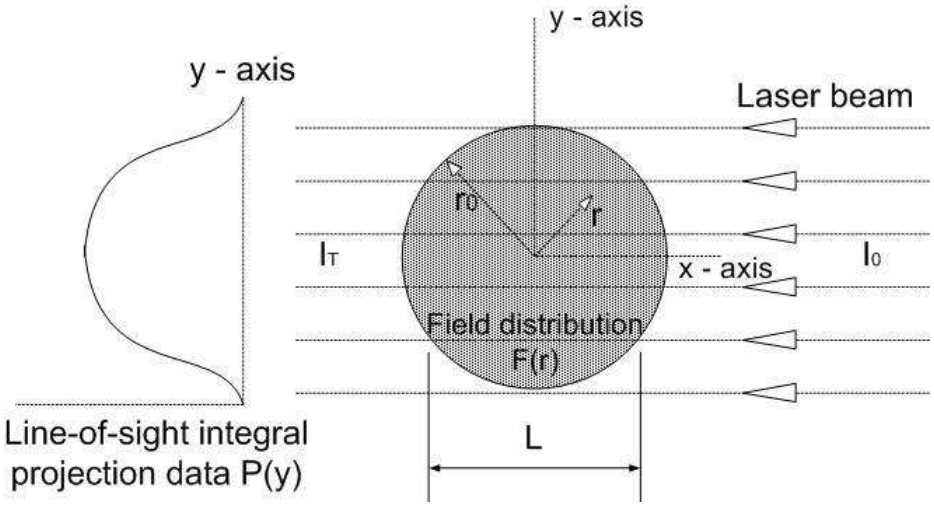

Figure 4.3: Scheme of an extinction measurement.

can be neglected and absorption is equal to extinction [6]. The extinction coefficient (K_{ext}) can be calculated by measuring the transmitted light intensity I_T, the incident light intensity I_0 and the absorption length L in the flame:

$$K_{ext} = \frac{1}{L} \ln \frac{I_0}{I_T} \tag{4.2}$$

Assuming the soot particles to be spherical, the soot volume fraction can now be calculated:

$$f_v = \frac{\lambda}{K_e} K_{ext} \tag{4.3}$$

In Eq. 4.3 K_e is the dimensionless optical extinction coefficient. The calculation of K_e demands knowledge of the soot refractive index (m) and scattering to absorption ratio (α_{sa}). The latter is neglected in the Rayleigh regime. Recently reported values of K_e are in the range of 8 to 10 at a wavelength of 632.8 nm [7, 8]. The logarithm of the incident laser intensity divided by the transmitted laser intensity determines the line-of-sight integral projection data:

$$P(y) = \ln \left(\frac{I_0}{I_T} \right) \tag{4.4}$$

In order to convert line-of-sight integral projection data of an axisymmetric measurement field into a spatially resolved distribution $F(r)$, in this case spatially resolved (K_{ext}) and subsequently soot volume fraction, inverse Abel transformation is applied:

$$F(r) = -\frac{1}{\pi} \int_{y=r}^{y=y_{max}} \frac{P'(y)}{\sqrt{y^2 - r^2}} \, dy \tag{4.5}$$

Numerically, the integral is replaced by a summation with segments between points y_i and P' is considered to be constant between these points. This leads to

$$F(r) = \sum_{y_i=r}^{y_i=y_{max}} -\frac{1}{\pi} P'(y) \int_{y=y_i}^{y=y_i+y_{step}} \frac{dy}{\sqrt{y^2 - r^2}}, \tag{4.6}$$

in which the integral can be evaluated analytically, and the derivative $P'(y)$ is obtained from the measurements.

Optical setup

The LOSA layout and equipment used in this work are shown in figure 4.4.

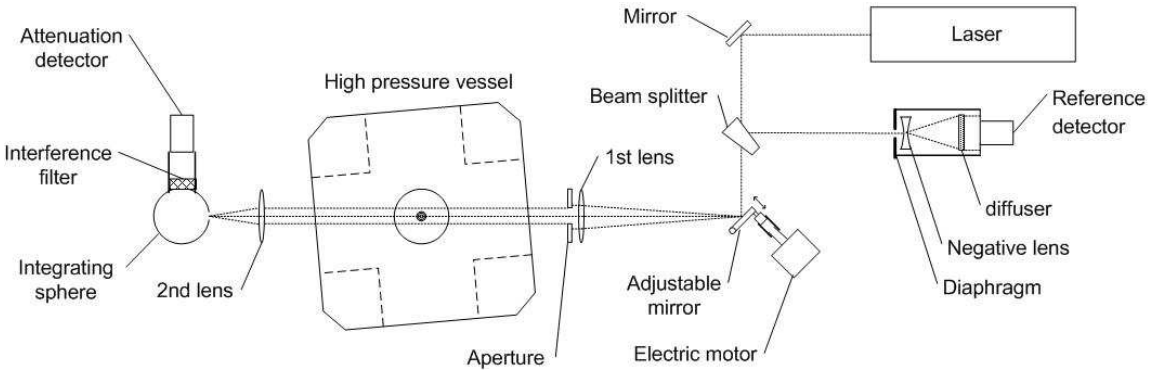

Figure 4.4: LOSA layout and equipment.

The LOSA setup is designed to minimize all possible disturbances. The laser used for this research is a HeNe laser, with a power of 5 mW and a wavelength of 632 nm. To compensate for laser intensity variation, a reference detector is used. Making use of a wedge shaped beam splitter; approximately 4% of the laser intensity is split to the reference detector. The incident light intensity is determined from the measurement without flame and the reference signals. To filter out background light in the reference detector, a tube with a diaphragm is placed in front of it. To prevent errors due to non-uniformity of the reference detector a negative lens is placed behind the diaphragm to diverge the beam to the size of the detector and a diffuser is placed just before the detector to make the signal completely uniform. The mirrors used in the setup are first layer mirrors to prevent multiple reflections. A laser scan is created by an adjustable mirror and two positive anti-reflection coated lenses. The angle of the adjustable mirror can be changed with an electric step-motor; the length of the scan is approximately 30 mm. The aperture right behind the first lens will block the laser beam when it is far away from the flame and transmits the beam when it is close to or in the flame. The laser beam with a diameter of 0.8 mm is focused in the flame where its diameter is approximately 100 μm. The diameter of the second lens is 50 mm and it is large enough to compensate for beam steering. An integrating sphere is used to create a uniform light beam for the interference filter and the attenuation detector. The entrance of the integrating sphere is placed behind the second lens at

its focal point to make sure that the total light from the laser beam will always be captured by the integrating sphere. The interference filter with a wavelength of 632 nm and a FMHW of 3 nm, filters out background light. The HPVB is placed slightly non-perpendicularly ($\sim 15\,^{\circ}$) to the laser beam, to prevent reflections in the same direction as the main laser beam.

Measurement procedure

The first measurements of soot volume fraction performed with this experimental setup are carried out in ethylene and n-heptane laminar diffusion flames at atmospheric pressure. In order to validate the LOSA measurements on the HPVB, results of soot volume fraction measured in laminar diffusion ethylene flames are compared with available data from Smooke and co-workers [9] using the same dimensionless extinction coefficient ($K_e = 10$). The oxidizer is air and the fuel is a mixture containing varying ratios of ethylene and nitrogen. Two flames are selected and named according to the ethylene/nitrogen fractions: 60% ethylene/40% nitrogen flame and 80% ethylene/20% nitrogen flame flame.

To generate laminar n-heptane diffusion flames, the n-heptane is vaporized in the CEM using nitrogen as a carrier gas and air is used as a coflow oxidizer. Two flames are generated: flame 1 has an n-heptane mass flow of 4 g/h, nitrogen flow of 0.052 L/min and coflow air of 30 L/min; flame 2 has an n-heptane mass flow of 4 g/h, nitrogen flow of 0.070 L/min and coflow air of 25 L/min. One set of measurements consists of an average of six unique measurements (a radial scan in the flame). Three sets of measurements are carried out at different days to evaluate the precision.

The soot volume fractions in these flames were measured at different flame heights. The flame height zero (the flame base) is accurately determined by changing the burner height until the laser beam is attenuated by the fuel tube tip. The scan-velocity of the laser beam is measured by scanning the beam over a known distance and analyzing the signal on the oscilloscope. This velocity is used to determine the radial position of the laser in the flame. The middle of the flame is determined by assuming the flame to be axially symmetric. To examine whether this assumption is valid, the attenuation signal of both sides of the flame is compared with every measurement. The laser scans the flame from right to left with a speed of 4.63 mm/s and two signals are collected at the same time: one by the attenuation detector, the main signal (I_A), and one by the reference detector, the reference signal ($I_{0\ ref}$). The data is read out with a digital oscilloscope and from the oscilloscope the data is transferred to the computer where the data is interpreted. The same scan is made without flame, collecting I_{0NF} and $I_{0NF\ ref}$ (NF = 'no flame'). This data is also transferred to the computer, the two scans together form one measurement. In order to determine the exact transmitted laser intensity I_T, the contribution of the flame emission (I_{FE}) to the I_A must be subtracted. The flame emission can be measured with the attenuation detector by blocking the laser. There is another way to obtain the flame emission without this extra measurement. Taking the measurements with and without flame, it appears that the difference between the intensity of a measurement with flame, measured outside the flame area ($I_{A\ outsite\ flame\ area}$), and the incident laser intensity (I_0), is exactly equal to the flame emission. Therefore, I_T can be calculated by equations 4.7 and 4.8

$$I_T = I_A - I_{FE} \tag{4.7}$$

$$I_{FE} = (I_{A\ outsite\ flame\ area} - I_0). \tag{4.8}$$

The incident intensity (I_0) is determined using the measurement without a flame and the reference signals according to equation 4.9. This is done to take into account possible variations in laser intensity during the measurements.

$$I_0 = I_{0NF} \left(\frac{I_{0\ ref}}{I_{0NF\ ref}} \right) \tag{4.9}$$

In order to enhance the precision of the measurement, all measurements are performed six times. The average of this set of measurements is considered as one complete measurement.

4.1.4 Results and Discussion

Ethylene flames

In the subsequent figures we plot the radial profile of soot volume fraction measured in two ethylene flames along with the data provided by Smooke and co-workers. The ethylene flames generated in this work show differences in height of 5% when compared to those of Smooke. It is likely that these differences in flame heights are caused by the differences in accuracy of the mass flow controllers used in both setups. Due to this fact, the flames were compared at three different vertical positions: 30%, 50% and 70% of the respective flame heights. The flames measured in this work have 60% ethylene/40% nitrogen and 80% ethylene/20% nitrogen in the fuel tube. Figures 4.5 to 4.7 show the results obtained with the flame 60% ethylene/40% nitrogen.

The flame measured in this work showed very good stability with maximum standard deviations of the soot volume fractions of 0.06 ppm. Peak soot volume fractions are located on the flame wings and considering the heights measured, the peak value of 1.2 ppm appears at 50% of the flame height. The comparison with Smooke data shows very good agreement in the absolute soot volume fractions values and in the location of the maxima. Figures 4.8 to 4.10 show the results obtained with the flame 80% ethylene/20% nitrogen.

This flame also showed good stability, although it was less stable than the flame 60% ethylene/40% nitrogen, with maximum standard deviations of soot volume fractions being 0.08 ppm. Peak soot volume fractions also appear on the flame wings with a peak value of 2.5 ppm at 50% of the flame height. The comparison with Smooke data also shows good agreement in the curve profile and location of the maxima. However, the differences in the absolute soot volume fractions values are larger when comparing with the flame 60% ethylene/40% nitrogen.

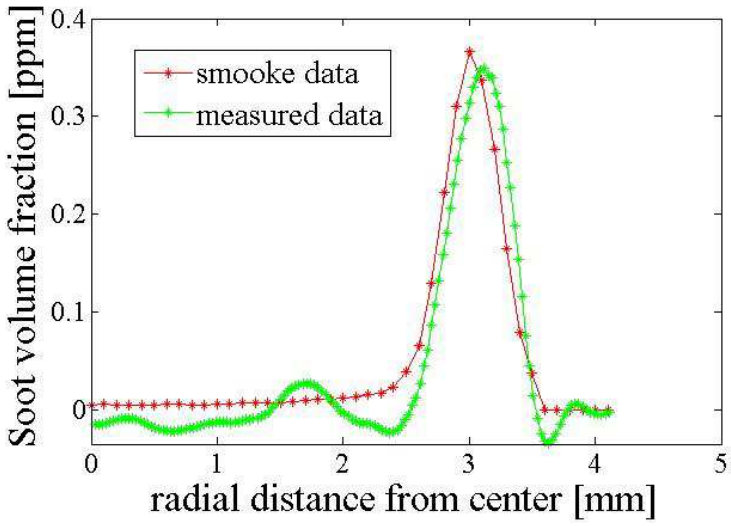

Figure 4.5: 60% ethylene/40% nitrogen flame soot volume fraction at 30% of the flame height.

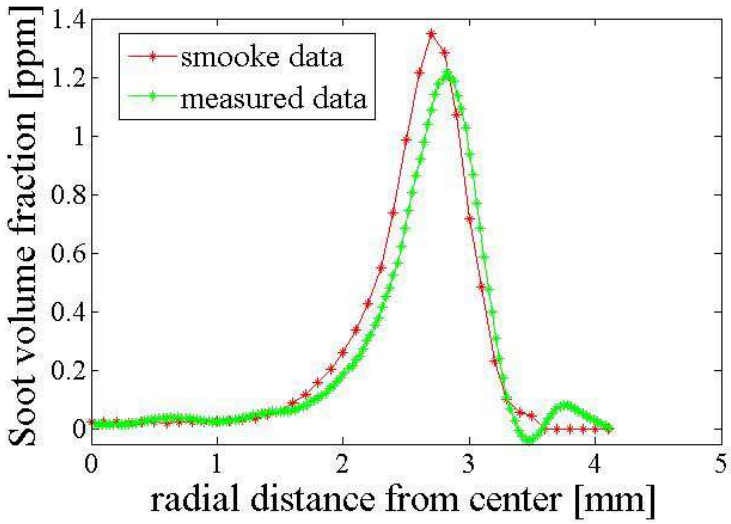

Figure 4.6: 60% ethylene/40% nitrogen flame soot volume fraction at 50% of the flame height.

n-Heptane flames

Figure 4.11 shows the first measurements of soot volume fraction in a vaporized liquid fuel flame performed with this experimental setup. The n-heptane flow is 4 g/h, nitrogen (carrier gas) flow is 0.052 L/min and the coflow air is 30 L/min. The measurements were carried out in five different days at 90% of the flame height.

The results show soot volume fractions in the center line (flame axis) varying from 1.3 ppm to 1.5 ppm and a large deviation of one measurement (set 4) near the flame edge. It can be seen that it was not possible to achieve the same repeatability as for ethylene with this flame, which has a maximum standard deviation of 0.17 ppm

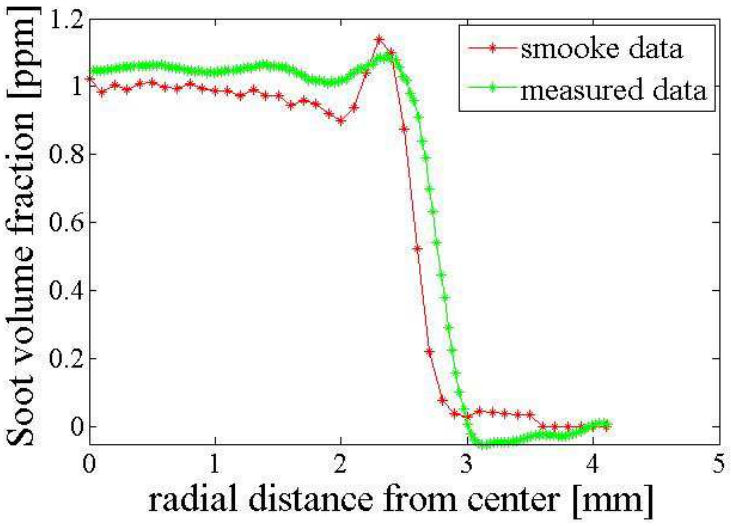

Figure 4.7: 60% ethylene/40% nitrogen flame soot volume fraction at 70% of the flame height.

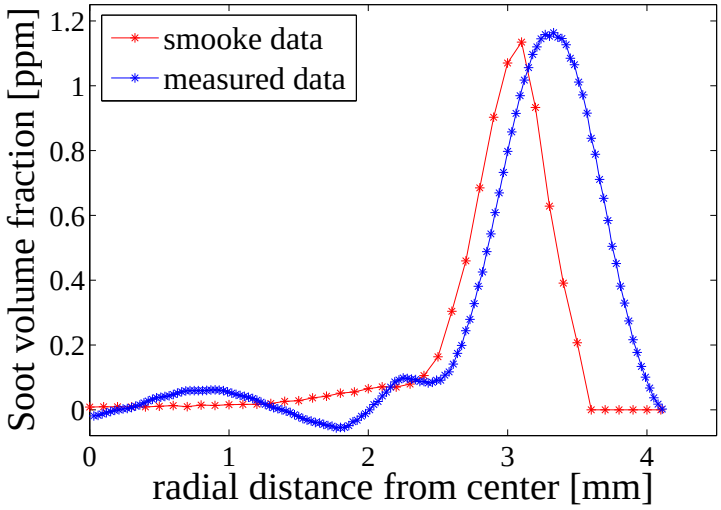

Figure 4.8: 80% ethylene/20% nitrogen flame soot volume fraction at 30% of the flame height.

within the flame area.

Efforts to improve the flame stability were made changing the carrier gas and oxidizer flows. A more stable flame was visually observed when using an n-heptane flow of 4 g/h nitrogen and air flows of 0.070 L/min and 25 L/min, respectively. The improved flame stability was reflected in the soot volume fractions measurements as can be seen in figure 4.12. The measurements were carried out in three different days also at 90% of the flame height.

As expected, the flame with 0.070 L/min of nitrogen has lower soot volume fractions when compared with the flame with 0.052 L/min of nitrogen due to the dilution

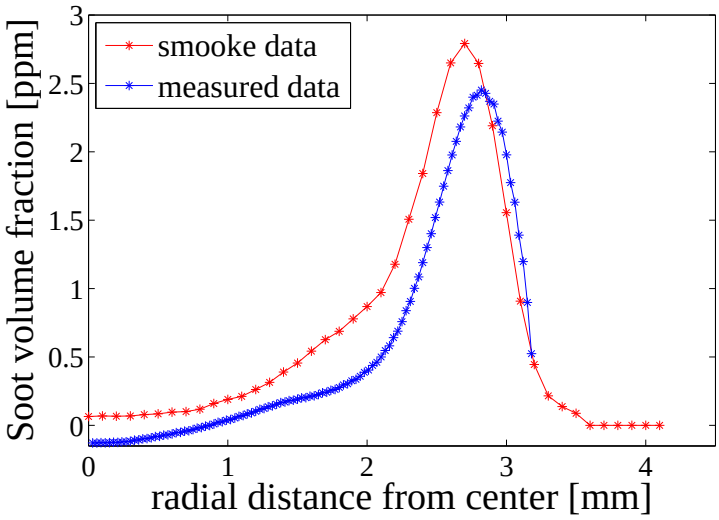

Figure 4.9: 80% ethylene/20% nitrogen flame soot volume fraction at 50% of the flame height.

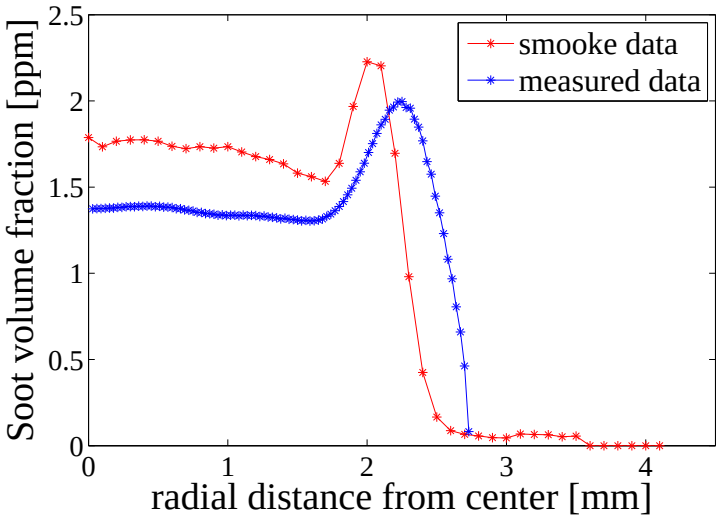

Figure 4.10: 80% ethylene/20% nitrogen flame soot volume fraction at 70% of the flame height.

effect. The maximum standard deviation of this flame was 0.04 ppm within the flame area. As in the case of ethylene flames, the wiggles observed in these two n-heptane flames can be caused by the fact that the line-of-sight integral projection data is smoothed less than in the center of the flame in these areas, as a result of the variable smoothing method used.

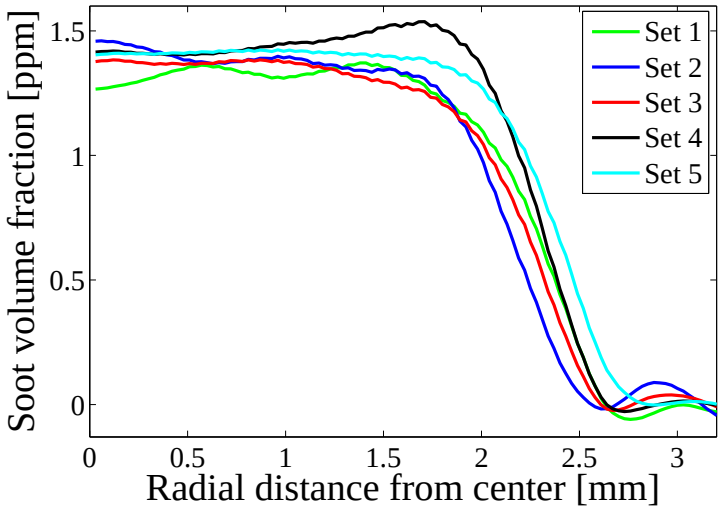

Figure 4.11: 4 g/h heptane/0.052 L/min nitrogen flame soot volume fraction at 90% of the flame height.

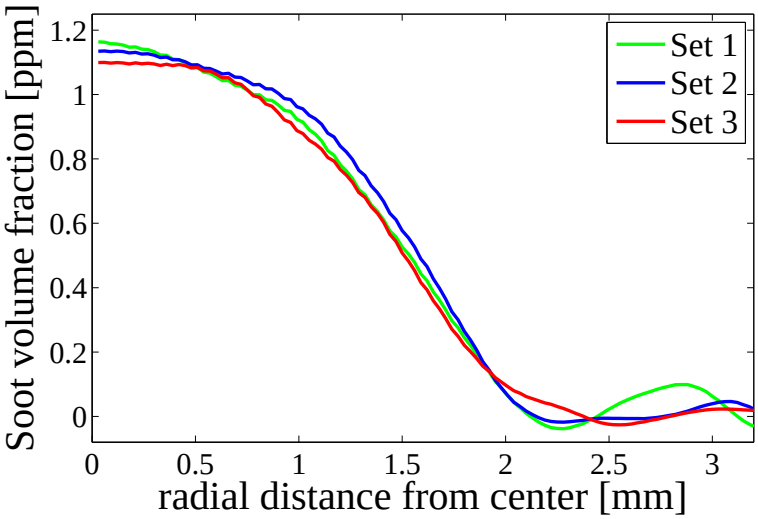

Figure 4.12: 4 g/h heptane/0.070 L/min nitrogen flame soot volume fraction at 90% of the flame height.

4.1.5 Conclusions

An experimental setup capable to burn gaseous and vaporized liquid fuels in laminar diffusion flames was constructed. The high pressure vessel and burner were designed to work at elevated pressures and to offer ample optical accessibility to apply laser diagnostic techniques. The first experiments with this setup were performed in ethylene and n-heptane flames at atmospheric pressure. The flames show good overall stability. Spatially resolved soot volume fractions were measured with line-of-sight-attenuation (LOSA) in combination with inverse Abel transformation. The measurements were validated with data from Smooke and co-workers in ethylene diffusion flames. Overall

good agreement was observed, both in peak values and location of maxima in soot volume fractions.

Soot volume fraction measurements were also performed in a vaporized liquid fuel (n-heptane) flame. The flame dynamics was clearly affected by the carrier gas and oxidizer flows. A reasonable stable flame was achieved with the flame of 4.0 g/h heptane/0.070 L/min nitrogen and 25 L/min coflow air. The results suggest that although it is possible to create a stable flame from a vaporized liquid fuel, more studies under different operational conditions should be performed with this setup to better evaluate the flame stability.

This experimental setup enables a variety of studies on liquid fuels at elevated pressures. It is also a useful tool for investigation of advanced laser diagnostics techniques in high pressure environments, allowing for improvements and new developments.

4.2 Preliminary soot measurements at elevated pressures in methane-air diffusion flames

Data at elevated pressures, which were outside the scope of the ECM paper reported in section 4.1, are reported in this section. Soot volume fraction measurements in a methane diffusion flame at pressures up to 1.0 MPa are presented.

As discussed in the section on flame stability (2.5), methane-air diffusion flames at pressures above 0.6 MPa showed asymmetry due to the formation of a water droplet on the fuel tip surface. This asymmetry can also be seen in the LOSA signal (the attenuation signal before conversion to soot volume fraction) where the left and right peaks have different heights, see figures 4.13 and 4.14. Although this effect is not so evident in the LOSA signals for 0.6 and 0.7 MPa (figure 4.13), it is quite pronounced for 0.8 and 1.0 MPa (figure 4.14). The spatial distribution of soot volume fraction will certainly be affected by this flame asymmetry.

Although the fuel mass flow rate at the fuel tip does not change due to the flame asymmetry, soot formation can possibly be influenced by changes in the flame properties and, consequently, also the values of soot volume fraction. Nevertheless, an attempt will be made to compare the maximum values of soot volume fraction ($f_{v_{max}}$) and their dependence on pressure with other similar flame conditions in the literature. The discrete soot measurement lines over the flame height are converted to a 2D picture for better identification of the location of $f_{v_{max}}$. In figures 4.15, 4.16 and 4.18(a), soot volume fractions are calculated via inverse Abel transformation using the proposed dimensionless extinction coefficient $K_e = 8.4$ (see section 3.1).

In order to compare the results with other pressurized methane flames from literature, two flames are selected and soot volume fractions are recalculated using the corresponding dimensionless extinction coefficient K_e of the respective literature sources. The first comparison is done with the work of McCrain and Roberts [10]. They used the LII technique to measure the soot volume fraction in methane flames up to 2.5 MPa and the signal is calibrated with extinction measurements. The refractive index for soot was chosen to be $m = 1.57 - 0.56i$ which leads to a coefficient

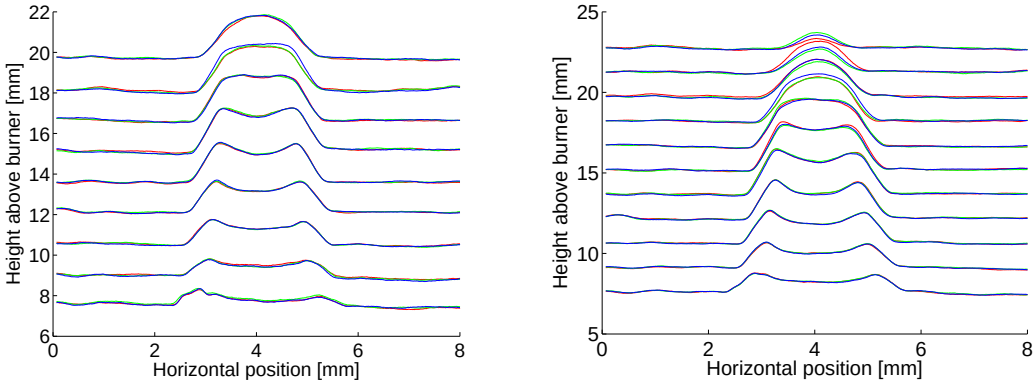

(a) LOSA signal at 0.6 MPa (b) LOSA signal at 0.7 MPa

Figure 4.13: LOSA signals of methane-air diffusion flames. Fuel flow = 0.1 L/min, coflow-air = 10 L/min.

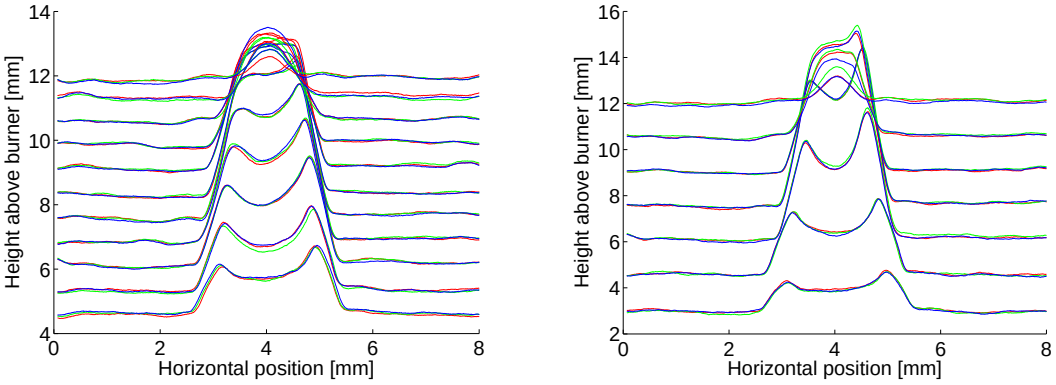

(a) LOSA signal at 0.8 MPa (b) LOSA signal at 1.0 MPa

Figure 4.14: LOSA signal of methane-air diffusion flames. Fuel flow = 0.1 L/min, coflow-air = 20 L/min.

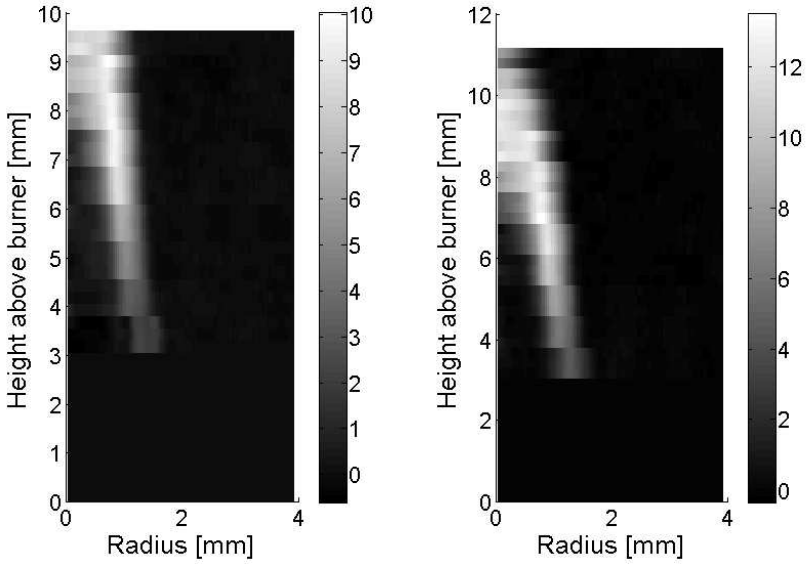

(a) 0.6 MPa and $f_{v_{max}}$=10 ppm (b) 0.7 MPa and $f_{v_{max}}$=13 ppm

Figure 4.15: Soot volume fraction profile of methane-air diffusion flames at elevated pressures. Fuel flow = 0.1 L/min, coflow-air = 10 L/min and K_e = 8.4.

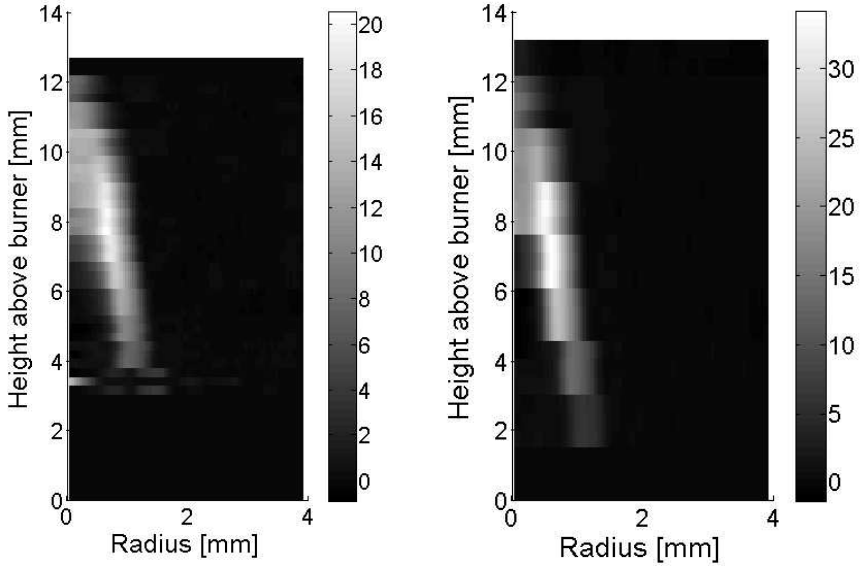

(a) 0.8 MPa and $f_{v_{max}}$=20 ppm (b) 1.0 MPa and $f_{v_{max}}$=34 ppm

Figure 4.16: Soot volume fraction profile of methane-air diffusion flames at elevated pressures. Fuel flow = 0.1 L/min, coflow-air = 20 L/min and K_e = 8.4.

$K_e = 5.6$. The methane flame at 0.8 MPa (figure 4.16(a)) is chosen for comparison and soot volume fraction is recalculated using $K_e = 5.6$ (figure 4.17). McCrain and Roberts [10] report a peak soot volume fraction of 20 ppm while we obtained 30 ppm (see figure 4.17). As discussed in the section 3.2, applying the LII technique in elevated pressure flames can lead to inaccurate results. Soot concentrations can be very high in pressurized flames and the LII signal is attenuated by the soot particles on the way to the detector. This is known as signal trapping and can become significant already at soot volume fractions above 10 ppm [6]. Choi and Jensen [2] developed a methodology to correct for signal trapping; however, Liu and co-workers [3] strongly disagree with their methodology, claiming that correction is very difficult because it requires knowledge of the distribution of soot volume fraction and the morphology of soot particles. Therefore, the signal trapping might still account for the lower values of soot volume fraction observed in the work of McCrain and Roberts [10].

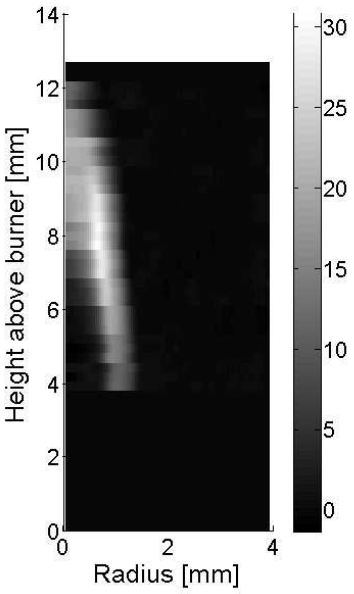

Figure 4.17: Soot volume fraction profile of methane-air diffusion flame using $K_e = 5.6$ for comparison with McCrain and Roberts [10]. Fuel flow = 0.1 L/min, coflow-air = 20 L_n/min and pressure = 0.8 MPa. Maximum f_v=30 ppm.

Thomson [11] used the LOSA technique to measure the soot volume fraction in methane flames up to 4.0 MPa. A constant value of $E(m)$= 0.27 was used and the ratio of scatter to absorption α_{sa} was assumed to be equal to 0.05 leading to a coefficient $K_e = 5.34$. Initially, for purpose of comparison with his work, a new measurement was performed by reducing the fuel flow of the flame in figure 4.16(b) to 0.05 L/min, keeping the pressure constant at 1.0 MPa, which resulted in a peak in soot volume fraction of f_v=13 ppm when using our $K_e = 8.4$ (see figure 4.18(a)). Then, the soot volume fraction profile of this flame was recalculated using the same $K_e = 5.34$ from Thomson [11], which resulted in a peak in soot volume fraction of f_v=20 ppm, see figure 4.18(b). It can be seen comparing with the result of Thomson (see figure 4.18(c))

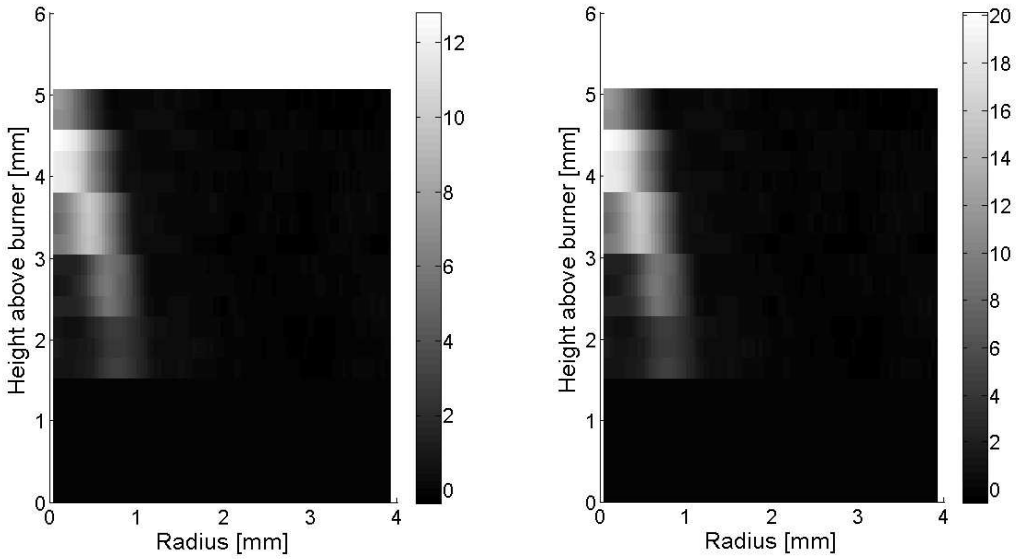

(a) $K_e = 8.4$ and $f_{v_{max}}$=13 ppm (b) $K_e = 5.34$ and $f_{v_{max}}$=20 ppm

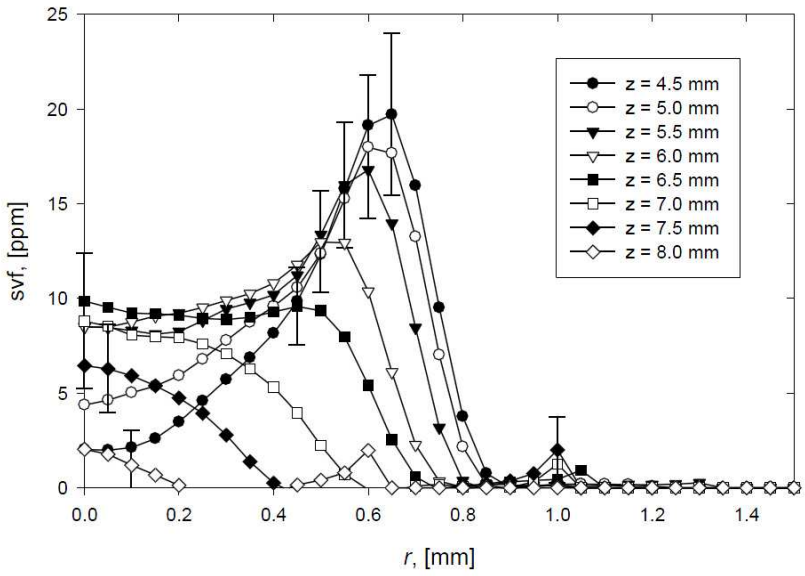

(c) $K_e = 5.34$, Thomson [11]

Figure 4.18: Soot volume fraction profile of methane-air diffusion flame. Fuel flow = 0.05 L/min, coflow-air = 20 L/min and pressure = 1.0 MPa.

that the peak soot volume fraction agrees in f_v=20 ppm. Although our value $f_{v_{max}}$ at 1.0 MPa agrees with the the work of Thomson [11] when using the same K_e = 5.34, the location of the maxima does not correspond. In the work of Thomson [11], the soot volume fraction peak is located on the wings (figure 4.18(c)) while in our work the peak is located near the flame center line (figure 4.18(b)). This difference is largely due to the flame asymmetry.

The dependence of the maximum soot volume fraction on pressure, normally reported in literature in the form $f_{v_{max}} \propto P^n$, was also evaluated and compared with the work of Thomson [11] and McCrain and Roberts [10], see figure 4.19. The LOSA measurements in this work indicate that the maximum soot volume fraction increases as $f_{v_{max}} \propto P^{2.46}$ over the pressure range of 0.6 to 1.0 MPa. This trend agrees closely with the work of Thomson for the pressures of 0.5 and 1.0 MPa while it does not agree with the work of McCrain and Roberts over the pressure range of 0.2 to 0.8 MPa.

Despite the flame asymmetry, the measurements of methane-air flames in this work show good agreement with the work of Thomson for pressures up to 1.0 MPa. The problem with the flame asymmetry was solved after the measurements reported here, however, new measurements could not be performed within the time of this research.

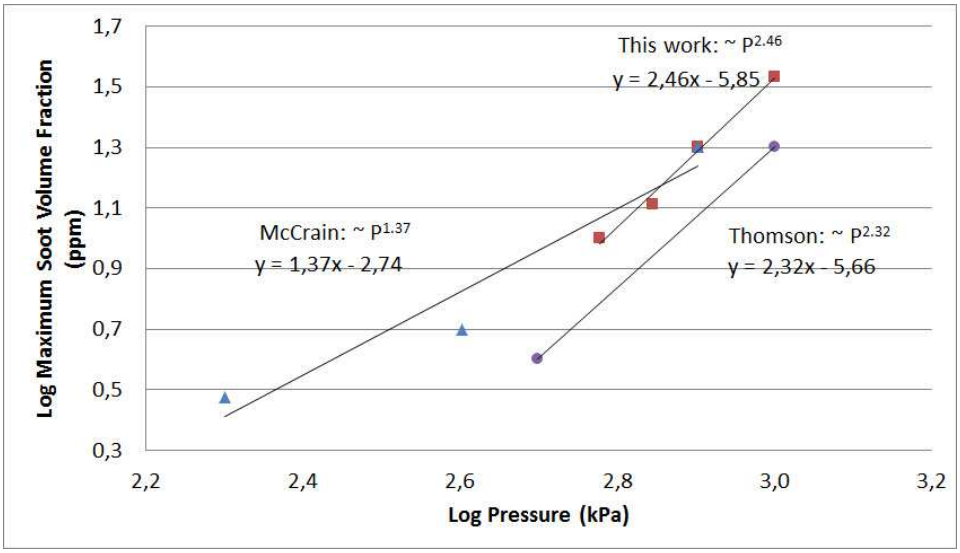

Figure 4.19: Comparison of soot volume fraction as a function of pressure for methane-air flames.

Bibliography

[1] M.D. Smooke, Y. Xu, R.M. Zurn, P. Lin, J.H. Frank, and M.B. Long. Computational and experimental study of OH and CH radicals in axisymmetric laminar diffusion flames. *in: Twenty-Fourth International Symposium on Combustion, The Combustion Institute, Pittsburgh*, pages 813–822, 1992.

[2] M.Y. Choi and K.A. Jensen. Calibration and correction of laser-induced incandescence for soot volume fraction measurements. *Combustion and Flame*, 112: 285–491, 1998.

[3] F. Liu, K.A. Thomson, and G.J. Smallwood. Effects of soot absorption and scattering on LII intersities in laminar coflow diffusion flames. *Journal of Quantitative Spectroscopy and Radiative Transfer*, 109:337–348, 2008.

[4] K.A. Thomson. *Soot Formation in Annular Non-premixed Laminar Flames of Methane-Air at Pressures of 0.1 to 4.0 MPa*. PhD thesis, University of Waterloo, 2004.

[5] S. Kunte. *Untersuchuchen zum Einfluss von Brennstoffstruktur und -sauerstoffgehalt auf die Russbildung und -oxidation in laminaren Diffusionsflammen*. PhD thesis, Eidgenössischen Technischen Hochschule Zürich, 2003.

[6] C.R. Shaddix and K.C. Smyth. Laser-induced incandescence measurements of soot production in steady and flickering methane, propane, and ethylene diffusion flames. *Combustion and Flame*, 107:418–452, 1996.

[7] S.S. Krishnan, K.C. Lin, and G.M. Faeth. Extinction and scattering properties of soot emitted from buoyant turbulent diffusion flames. *Journal of Heat Transfer*, 123:331–339, 2001.

[8] J. Zhu, M.Y. Choi, G.W. Mulholland, S.L. Manzello, L.A. Gritzo, and J. Suo-Anttila. Measurement of visible and near-IR optical properties of soot produced from laminar flames. *Proceedings of the Combustion Institute*, 29:2367–2374, 2002.

[9] M.D. Smooke, M.B. Long, B.C. Connelly, M.B. Colket, and R.J. Hall. Soot formation in laminar diffusion flames. *Combustion and flame*, 143:613–628, 2005.

[10] L.L. McCrain and W.L. Roberts. Measurements of the soot volume field in laminar diffusion flames at elevated pressures. *Combustion and Flame*, 140:60–69, 2005.

[11] K.A. Thomson. *Soot formation in annualr non-premixed laminar flames of methane-air at pressures of 0.1 to 4.0 MPa*. PhD thesis, University of Waterloo, 2004.

CHAPTER 5

Soot, PAH and OH measurements in vaporized liquid fuel flames

Qualitative measurements of OH and polycyclic aromatic hydrocarbons (PAH) and quantitative data of soot volume fraction f_v in vaporized liquid fuels are presented, with the main goal of providing experimental data for combustion models and numerical mechanism validation. Measurements were carried out in a laminar coflow burner which was also designed and integrated with an evaporation system to work with vaporized liquid fuels at elevated pressures up to 3.0 MPa. The fuels n-heptane and n-decane are mentioned in the literature as important surrogate fuels and were chosen for the first measurements at atmospheric pressure in this experimental setup, using a combination of the Laser Induced Fluorescence (LIF) and Laser Induced Incandescence (LII) techniques. The partially premixed flames of n-heptane and n-decane showed similar combustion characteristics in the range of $1.9 < \phi < 3.7$. For both fuels the threshold for soot formation was observed around $\phi \sim 3.3$. Comparison between LIF and LII measurements for n-heptane flames in the range of $3.7 \leq \phi \leq 8.5$ indicates that the maximum PAH LIF signal is a good predictor of $f_{v_{max}}$ from LII. Excitation at 266 nm with delayed detection results in signals giving a linear correlation with soot volume fraction from LII using prompt detection at 1064 nm excitation. Hence, the influence of any additional photo-chemical processes using high laser power at 266 nm and the influence of particle size for the delayed gate time, appear not significant for the flame conditions studied here.

The contents of this chapter will be submitted to a scientific journal.

M.H. de Andrade Oliveira, H. Bladh, N.-E. Olofsson, J. Johnsson, A. Lantz, B. Li, Z. Li, M. Aldén, P.-E. Bengtsson, C.C.M. Luijten, L.P.H de Goey. *Soot, PAH and OH measurements in laminar flames of liquid fuels.*

5.1 Introduction

Most investigations on soot formation so far have been performed in laminar flame burners, in which simple fuels such as methane, ethane or ethylene are burnt at atmospheric pressure [1–7] . However, practical combustion systems such as diesel engines, which are a significant source of soot formation, burn liquid fuels at high pressure. One reason that most of the studies have been carried out with simple fuels is the experimental difficulties involved in vaporizing larger hydrocarbon fuels. Moreover, simulations of laminar flames of these larger hydrocarbons require a complex and expensive computational analysis using extensive chemical mechanisms. Practical fuels, such as diesel, comprise hundreds of larger hydrocarbons (alkanes, cycloalkanes, aromatics, etc) making experimental and computational analysis even more challenging.

The surrogate approach is an attempt to overcome the challenge of modeling practical fuel combustion. Surrogate fuels are simpler representations of practical fuels that could sufficiently represent their physical and chemical properties. These fuels have been studied in practical devices, such as engines [8–10]. However, in practical combustion systems it is difficult to isolate fuel chemistry effects from changes in flame lift-off length, temperature, pressure, etc., that may be caused by both physical and chemical effects.

An attempt to build a bridge between the most simplified and complex systems has been made by designing and constructing a high pressure vessel and laminar burner (HPVB) integrated with an evaporation system. The capability of the HPVB setup of burning vaporized liquid fuels in laminar diffusion and partially premixed flames brings the important opportunity to isolate more easily the impact of fuel chemistry on the combustion behavior of relevant fuels and bio-fuels. This experimental setup was particularly designed to offer optical accessibility for laser diagnostic techniques, also allowing their assessment and development at elevated pressures. Its specifications and first measurements are described elsewhere in more detail [11].

In this work, Laser Induced Fluorescence (LIF) and Laser Induced Incandescence (LII) techniques are applied to characterize laminar coflow flames at atmospheric pressure of two important surrogate fuels: n-heptane and n-decane. Qualitative profiles of OH, polycyclic aromatic hydrocarbon (PAH) and soot, as well as soot volume fractions measurements, are performed and the combustion characteristics of both fuels are discussed. A combined LII-LIF approach is applied to unambiguously identify the spatial location of PAH's and soot by comparing laser-induced emission using either 1064 nm or 266 nm as excitation light, as demonstrated by Vander Wal [12–14]. The delayed detection approach, where the LII signal is detected after the laser pulse, has been suggested [15] as one strategy to suppress the spectral emission from C_2 and PAH interfering with the LII signal. However, the prompt LII has shown a better linearity to soot volume fraction than the delayed signal [16]. Besides that, long or delayed detection gates bias the LII signal towards large particles since smaller particles cool faster than large ones (see [17] and references therein). The influence of these issues, related to the delayed detection approach, is verified in this work by comparing the qualitative soot (delayed) signals obtained with 266 nm and the quantitative soot

volume fraction obtained with 1064 nm. Ultimately, the main goal is to provide experimental data for combustion models and numerical schemes validation. Although a considerable amount of experimental data for this purpose has been produced in the laminar (diffusion and premixed) coflow flame configuration, they mostly represent hydrocarbon fuels with $< C_4$ (gaseous fuels). Therefore, the data on vaporized liquid fuels presented here represent a further step towards more practical fuels.

5.2 Experimental methods

5.2.1 High Pressure Vessel and Burner

The High Pressure Vessel and Burner (HPVB) setup was already described in detail in [11] and only the main characteristics will be mentioned here. The burner dimensions are based on the Long and Smooke burner [1]: it is a coflow burner with a fuel tube inner and outer diameter of 4 mm and 6 mm, respectively. The oxidizer coflow inner diameter is 50 mm with a height of 100 mm. The burner design was adapted to fit in a high pressure vessel and to work at pressures up to 3.0 MPa (figure 5.1). The vessel offers optical accessibility for laser diagnostics through four quartz windows with a diameter of 50 mm and eight additional holes to insert measurement equipment such as thermocouples and pressure sensors. A commercial evaporation system called CEM (Controlled Evaporator Mixer) can accurately mix and control the liquid fuel and carrier gas, providing a stable fuel vapor stream at temperatures up to 473 K. The tube connecting the CEM to the burner and the burner itself are electrically heated in order to avoid condensation of the fuel vapor.

For the measurements presented in this paper, the temperature in the CEM, heating hose and burner is set to maintain the fuel vapor at $\approx 100\,^{\circ}C$ for n-heptane and $\approx 200\,^{\circ}C$ for n-decane. Partially premixed flames are created by using air as a carrier gas (primary air, mixed with fuel), and as a coflow oxidizer. The coflow oxidizer is maintained at 20 L/min for the n-heptane flames and 25 L/min for the n-decane flames, which helps to stabilize the flames. The liquid fuels (99.9% purity) are stored in a 0.5 liter container and led to the evaporator by pressurization with nitrogen. All gases are metered with calibrated mass flow controllers (Bronkhorst, EL-FLOW type) with absolute uncertainties in the flow rates of $\pm$ 5%. The fuel flow is accurately measured and controlled by a liquid mass flow meter and the CEM. The operating flow conditions for the measurements are shown in Table 5.1 for n-heptane flames and in Table 5.2 for n-decane flames.

5.2.2 Optical measurements

Figure 5.2 shows the experimental setup used for the measurements. Two different laser-based measurement techniques were used, Laser-Induced Fluorescence (LIF) and Laser-Induced Incandescence (LII). LIF was used to detect OH radicals using 283 nm and polyaromatic hydrocarbons (PAH's) using 266 nm excitation, whereas LII was used to detect soot volume fraction using 1064 nm excitation.

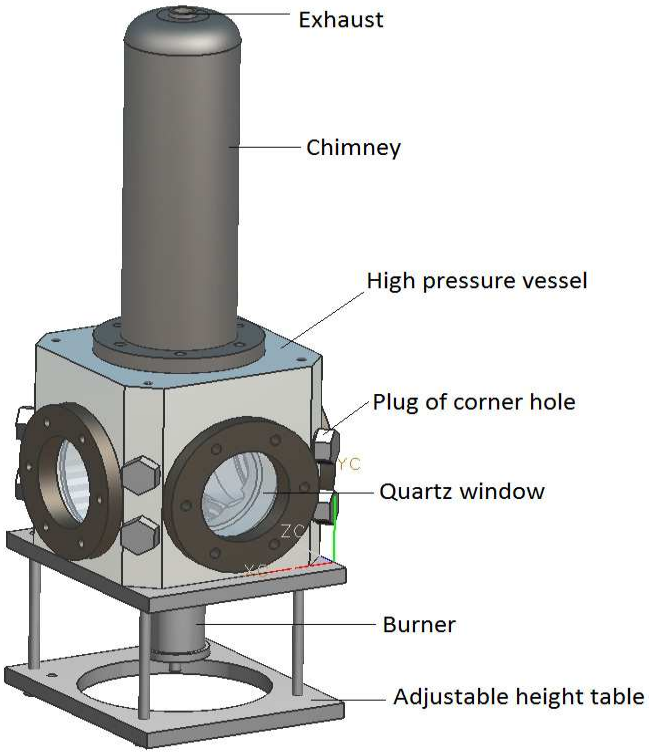

Figure 5.1: Pressure vessel and assembled parts.

Table 5.1: Flow conditions for n-heptane flames.

Fuel flow [g/h]	Carrier gas flow [g/h] and [L/min]	Equivalence ratio (ϕ)
4.5	36.5 - 0.471	1.9
4.5	29.3 - 0.377	2.3
4.5	24.4 - 0.315	2.8
4.5	21.0 - 0.270	3.3
4.5	18.4 - 0.237	3.7
4.5	12.2 - 0.157	5.6
4.5	10.5 - 0.135	6.5
4.5	8.0 - 0.103	8.5

Table 5.2: Flow conditions for n-decane flames.

Fuel flow [g/h]	Carrier gas flow [g/h] and [L/min]	Equivalence ratio (ϕ)
3.5	28.2 - 0.364	1.9
3.5	22.6 - 0.291	2.3
3.5	18.9 - 0.244	2.8
3.5	16.1 - 0.208	3.3
3.5	14.1 - 0.182	3.7

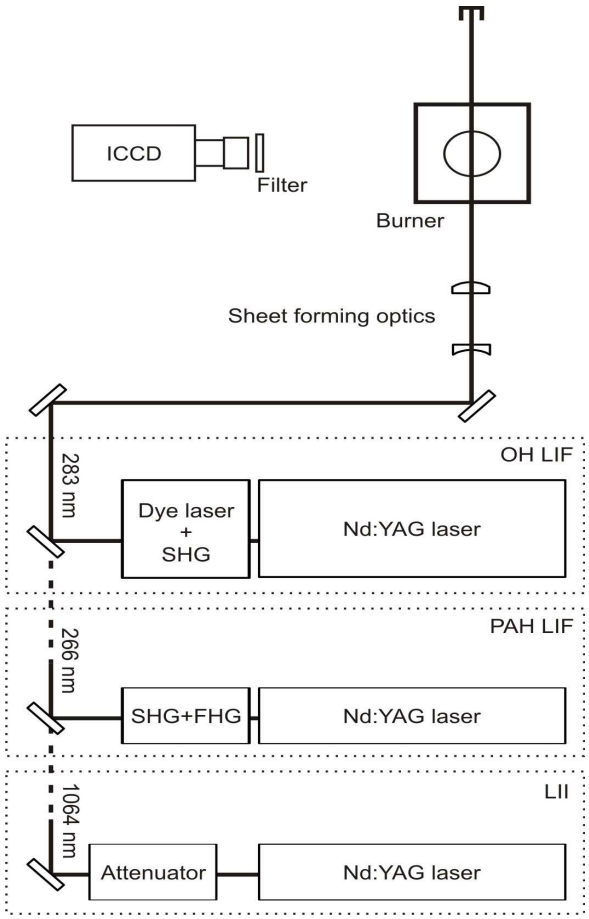

Figure 5.2: Experimental setup for OH and PAH LIF and LII. FHG and SHG stand for Fourth and Second Harmonic Generation, respectively.

For the OH LIF, a dye laser (Continuum ND60) was pumped by the second harmonic radiation of a Nd:YAG laser (Spectra-Physics, PRO-290). The frequency-doubled output of the dye laser at 283 nm was used to excite the OH radical. The 283 nm laser beam was formed into a 3 cm high laser sheet by a combination of cylindrical and spherical lenses. The OH radical was excited through the $Q_1(8)$ transition in the $A^2\Sigma^+$ - $X^2\Pi(1,0)$ band and the resulting fluorescence emission occurs at around 308 nm. The fluorescence signal was detected using an intensified CCD camera (PI-MAX, Princeton Instruments) equipped with a UV lens (UV-Nikkor, f=105 mm) and an interference filter at 310 nm (FWHM).

For the PAH LIF measurements, the 4^{th} harmonic at 266 nm from a Nd:YAG laser (Brilliant b, Quantel) was used to excite the PAH's using the same laser sheet optics, intensified CCD camera and UV-lens as for the OH LIF measurements. When using the strong 266 nm for excitation, there are contributions from both soot incandescence and PAH fluorescence in the detected signal. In order to distinguish these, two subsequent measurements were carried out: prompt detection (synchronized with the laser pulse) which contains both LIF and LII contributions; and delayed detection (50 ns after the laser pulse) which avoids the LIF signal from PAH's due to its

short life time (on the order of nanoseconds). A combination of a liquid dimethylformamide filter and a Schott filter, BG3, was used to suppress scattered laser light and collect the fluorescence signal in the range from 300 to 500 nm. For both OH and PAH LIF measurements, 500 single shots were recorded and averaged. Calculation from 500 single-shot measurements showed signal intensity variations of 7% (1 σ).

PAH's is a group of molecules with various numbers of aromatic rings, and it is well-known that these species absorb in broad spectral regions and fluoresce in broad spectral regions as well [18, 19]. Absorption at a specific wavelength thus excites a number of PAH molecules, and gives no specific selectivity. However, good correlation between the concentration of some PAH species and the maximum intensity of the PAH LIF signals has been observed [20].

The LII measurements were carried out using a Nd:YAG laser at 1064 nm, with the laser beam formed into a thin sheet directed through the flame. A fluence of 0.32 J/cm^2 at the start of the plateau regime [17] was used to ensure results with low dependence on laser pulse energy and attenuation/trapping. The laser power was adjusted using an attenuator. An intensified CCD camera was used to image the incandescence perpendicular to the incoming laser sheet. For all LII measurements a gate width of 50 ns was used and accumulations of 500 shots were recorded. LII signals were quantified by calibrating the LII setup using a flat ethylene/air flame with ϕ=2.3 on a bronze McKenna burner, previously characterized by laser extinction at 1064 nm [21]. The uncertainty in the soot volume fraction measurements is mainly dominated by the uncertainties in the magnitude of the soot refractive index function, $E(m) = -Im\{m^2 - 1/m^2 + 2\}$. The refractive index of soot applied in [21] was $m = 1.56 - 0.46i$, resulting in a dimensionless extinction coefficient of $k_e = 5.01$ and $E(m) = 0.21$. This value is assumed also for the flames studied in this work.

5.3 Results and Discussion

5.3.1 Data interpretation

In figure 5.3, a set of images is shown from applying various laser techniques to the same flame, a partially premixed n-heptane flame ($\phi = 3.7$). The OH concentration is high in the outer diffusion flame where the temperature is high as a result of combustion of fuel and flame-generated species such as PAH's. The OH distribution (figure 5.3a) surrounds the PAH distribution, and the PAH molecules formed in the fuel-rich part and hot gas mixture will be oxidized in the combustion zone. For high enough equivalence ratios, soot is formed from PAH's which in turn are oxidized higher in the flame. Studying figure 5.3b it is, however, noticeable that the signal has a sharp structure at the top not really following the smoothly curved shape of the inner border in the OH image. When studying the complete data set this sharp peak is occurring for equivalence ratios higher than 3.3 and is attributed to laser-induced incandescence (LII) interference from soot particles. This conclusion is based on measurements where we delayed the camera gate with 50 ns with respect to the laser pulse. This delayed signal for 266 nm excitation (figure 5.3c) shows the same structure

as the sharp peak in figure 5.3b. At a delay of 50 ns only species with a considerably long lifetime can contribute to the signal. It is well-known that soot particles absorb radiation in UV/visible as well as IR spectral regions and LII signals can persist for lifetimes of microseconds. Additionally, the signal shape obtained using the delayed detection with 266 nm excitation overlaps with the LII image obtained using 1064 nm excitation (figure 5.3d). The detection of the delayed signal in LIF experiments nicely connects the different data sets, certifying that the somewhat different optical setups for the LIF and LII experiments are synchronized.

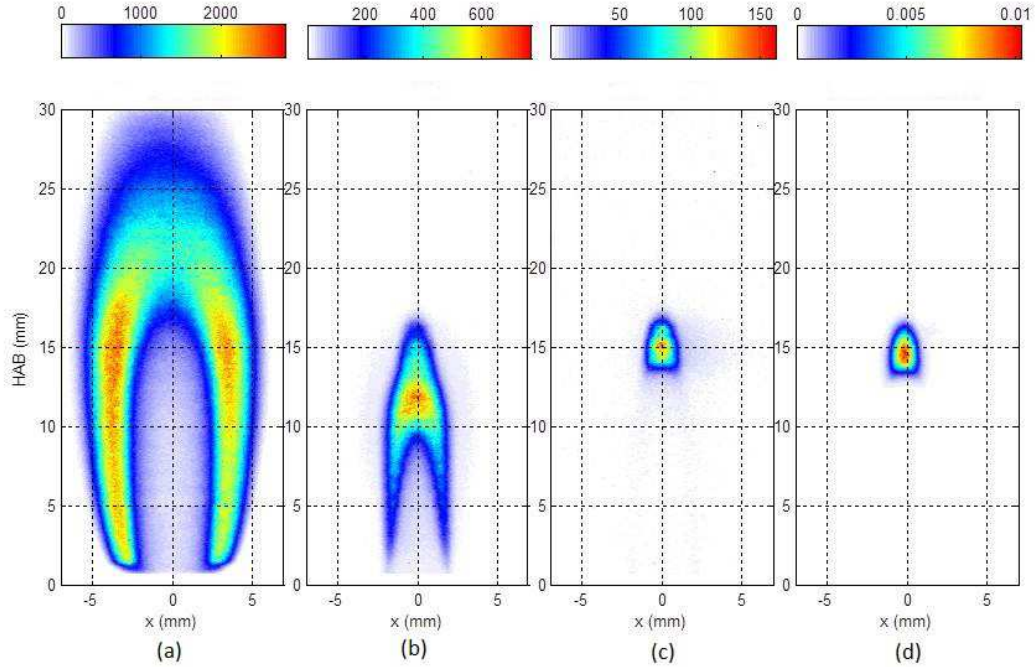

Figure 5.3: Example of measurement data from a partially premixed n-heptane flame ($\phi = 3.7$). a) shows a LIF image of the OH distribution. The signal obtained from excitation at 266 nm is shown for prompt detection (b) and delayed detection (c). Images a-c are only qualitative, the color bars showing detector counts. In d) the quantitative soot volume fraction image [ppm] obtained using LII is shown.

5.3.2 n-heptane and n-decane flames

The center line signals obtained from excitation at 266 nm for prompt detection (see 2D distribution example in Fig. 5.3b) are shown in figures 5.4 (n-heptane flames) and 5.5 (n-decane flames) as function of flame height (center line profiles) for equivalence ratios $1.9 \leq \phi \leq 3.7$. Although fuel flow rates of both fuels are different, ϕ represents a normalized fuel concentration which is kept the same for both fuels. One peak is observed for $\phi < 3.3$ corresponding to the PAH fluorescence, while for $\phi > 3.3$ another peak starts to appear at a flame height around 15 mm for n-heptane and around 12 mm for n-decane, which is attributed to incandescence from soot. Therefore, the equivalence ratio threshold where soot starts to be formed is similar ($\phi \sim 3.3$) for both

n-heptane and n-decane flames. At fuel equivalence ratios lower than this threshold, the soot precursors (PAH's) are not converted to soot indicating that the soot might be completely oxidized or formed in very low (not detectible) concentration.

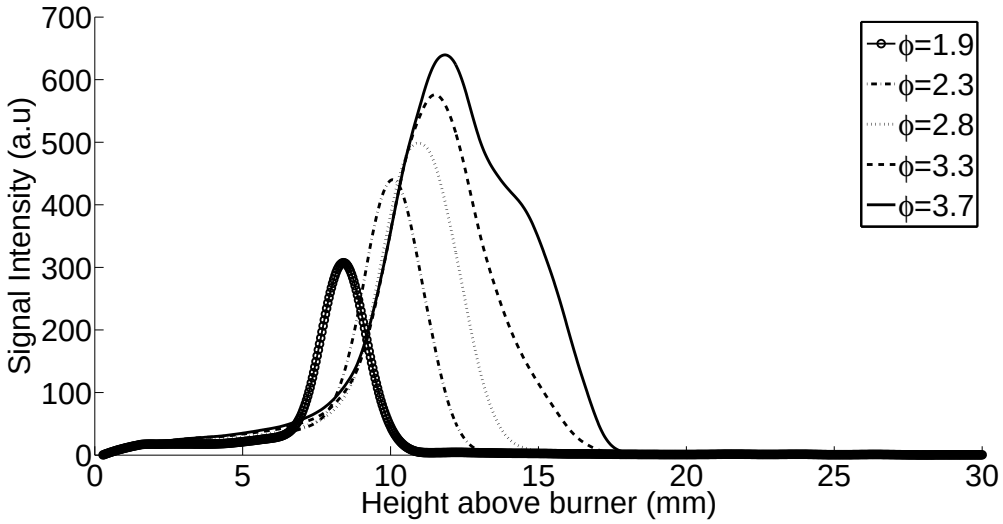

Figure 5.4: Center line signals obtained from excitation at 266 nm and prompt detection for n-heptane flames with $1.9 \leq \phi \leq 3.7$.

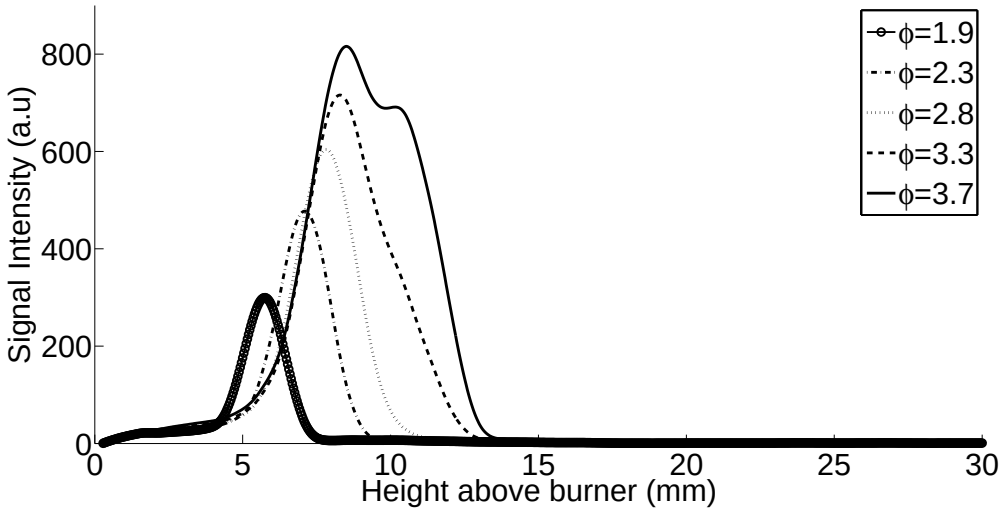

Figure 5.5: Center line signals obtained from excitation at 266 nm and prompt detection for n-decane flames with $1.9 \leq \phi \leq 3.7$.

Another indication of similar combustion characteristics between the n-heptane and n-decane flames is observed when comparing their maximum PAH LIF signals (see figure 5.6). The maximum PAH LIF signals show a monotonic increase as function of equivalence ratio (figure 5.6(a)) in the range of $1.9 < \phi < 3.7$. A very similar trend

is seen for both fuels, presenting a sharp increase from ϕ=1.9 to ϕ=2.3, followed by a smaller slope for higher values of ϕ. In figure 5.6(b), the maximum PAH LIF signals of n-heptane and for n-decane are normalized to their respective maximum values at ϕ=3.7 and a linear correlation (R^2=0.995) is found.

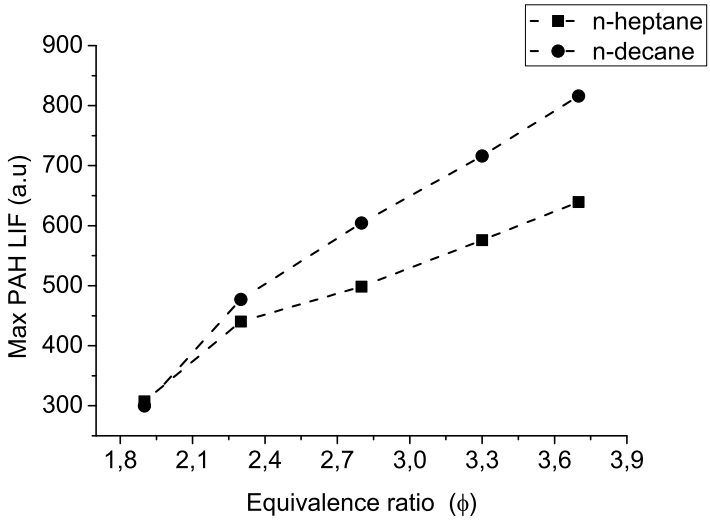

(a)

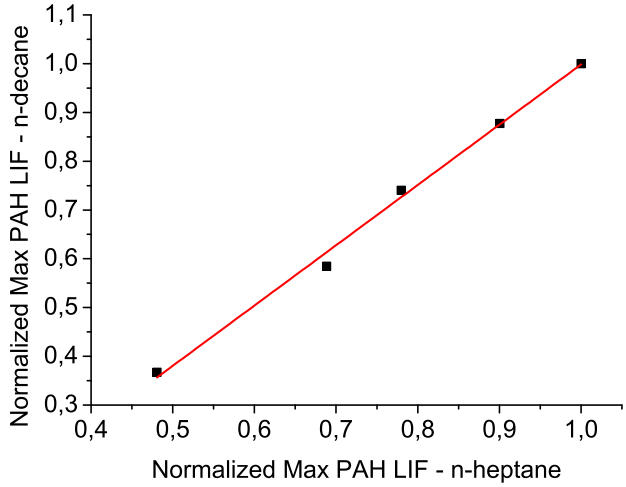

(b)

Figure 5.6: Maximum PAH LIF signals as function of equivalence ratio (a) and the correlation between the normalized maximum PAH LIF signals (b) in n-heptane and n-decane flames in the range of $1.9 \leq \phi \leq 3.7$. Red line: linear fit $y = ax+b$, with b$\neq$0 and R^2=0.995.

When fuel concentration in the n-heptane flames is increased further (by decreasing premixed air flow) to equivalence ratios up to ϕ=9.0, the LII signal from soot (second peak) becomes stronger than the PAH LIF signals (first peak) (see figure 5.7). As the 2D images in figure 5.8 also evidence, the second peak is LII from soot that becomes stronger as the equivalence ratio increases. Over this range of equivalence ratio ($3.7 \leq \phi \leq 8.5$), the soot LII signal starts to increase when the PAH

LIF is decreasing, which is observed as a local minimum in the region between both signal peaks. This observation supports the view that the chemical species giving rise to the LIF signal are soot precursors. Applying a combined LII-LIF technique, Vander Wal [12] also identified this local minimum characterizing the material from within this region by transmission electron microscopy (TEM). The results suggested conversion from soot-precursor material into solid carbonaceous soot particles. This transitional soot-precursors region has also been observed in other related studies of gas-jet diffusion flames [13, 14].

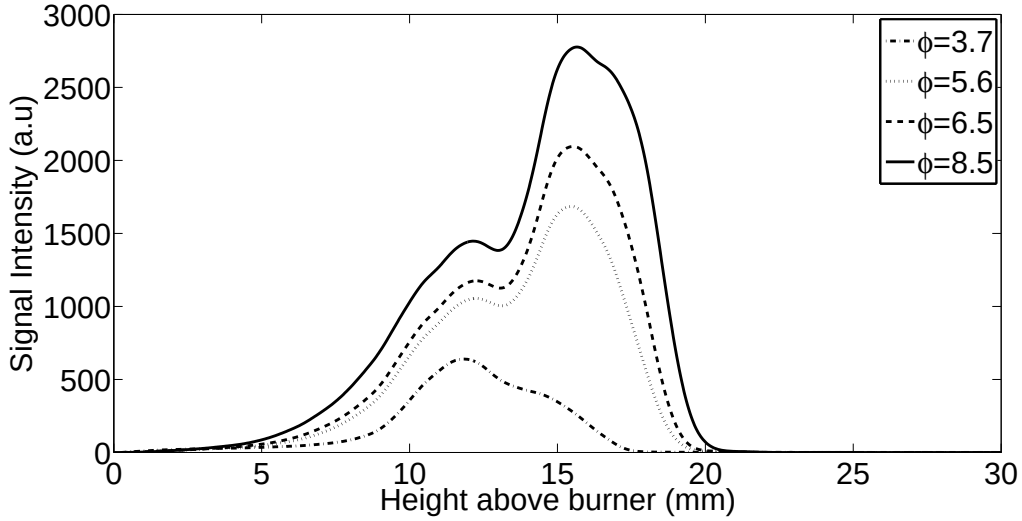

Figure 5.7: Center line signals obtained from excitation at 266 nm and prompt detection for n-heptane flames with $3.7 \leq \phi \leq 8.5$

The maximum soot volume fraction ($f_{v_{max}}$) obtained upon excitation with 1064 nm correlates very well ($R^2 > 0.99$) with the maximum prompt PAH LIF signal. The later is the first local maximum in figure (5.7). Figure 5.9 indicates that the maximum PAH LIF signal is a good predictor of $f_{v_{max}}$ from LII. This observation is in line with the work of McEnally and Pfefferle [20] on partially premixed ethylene flames.

We will now look further into possible influences related to the LII signal when using the delayed detection approach. These influences are assessed by comparing the signal obtained upon excitation with 266 nm and delayed detection, with the soot volume fractions obtained using (prompt) LII at 1064 nm excitation. Figure 5.10 shows that a good correlation coefficient ($R^2 > 0.99$) is found, indicating that the influence of particle size on the signal, which can be an issue when detecting the delayed LII signal, is minor [16]. The linear correlation also indicates that possible physicochemical interferences, which could be introduced using high-power UV excitation, do not produce systematic errors.

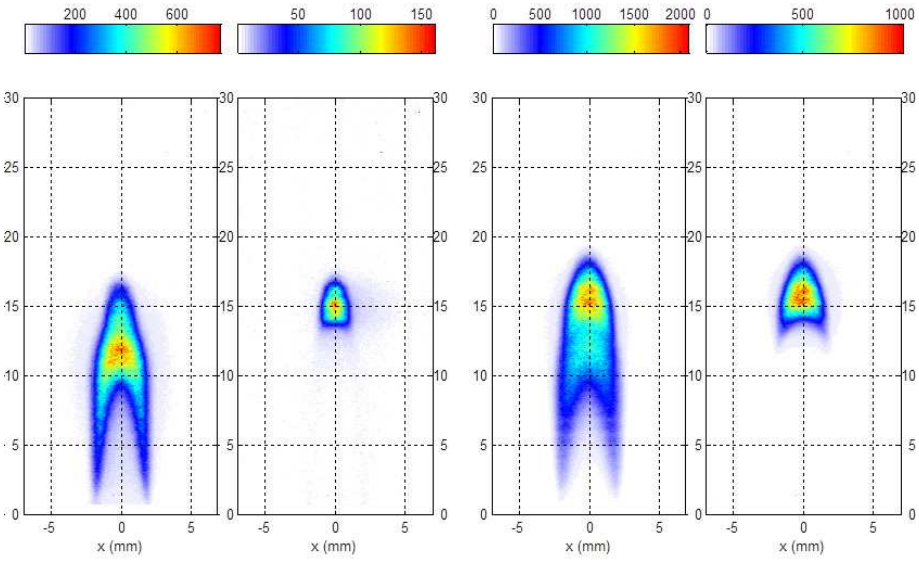

(a) ϕ=3.7 (b) ϕ=5.6

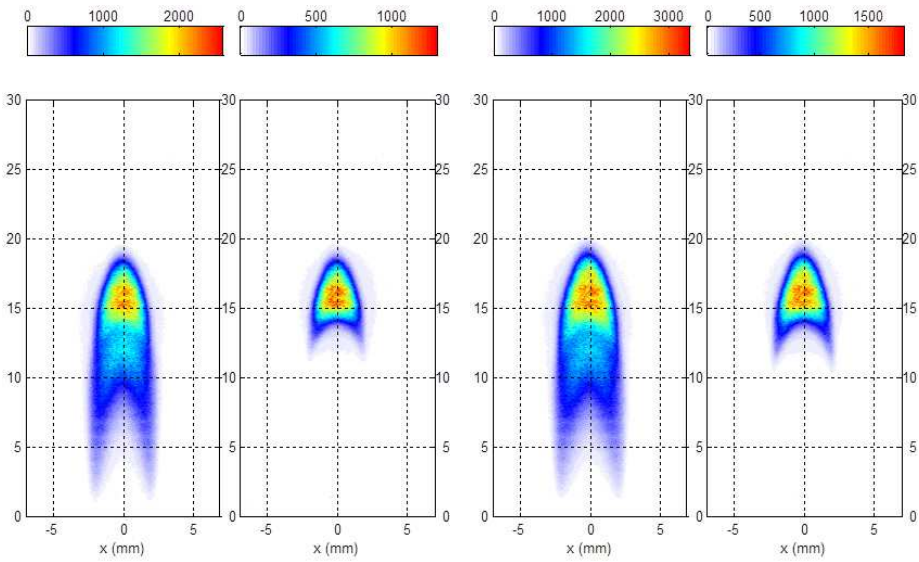

(c) ϕ=6.5 (d) ϕ=8.5

Figure 5.8: 2D images of n-heptane flames from excitation at 266 nm for prompt detection (left) and delayed detection (right).

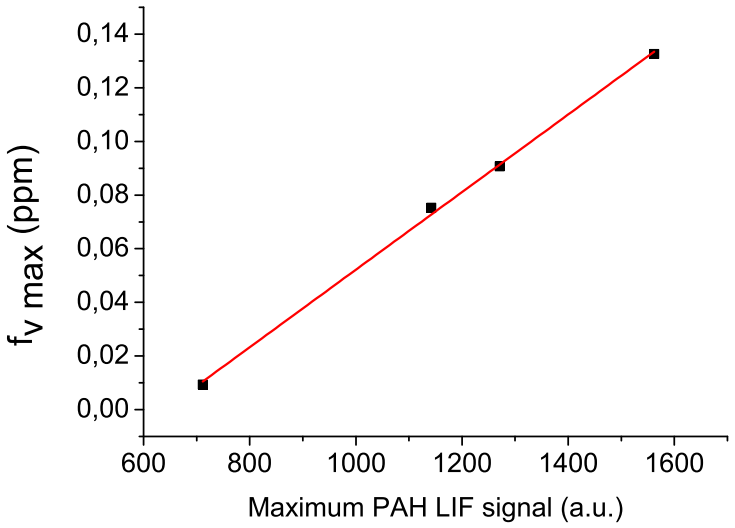

Figure 5.9: Correlation between maximum soot volume fraction and PAH LIF signal in n-heptane flames. Black squares: experimental data in the range of $1.9 \leq \phi \leq 3.7$. Red line: linear fit $y = ax + b$, with b≠0 and R^2=0.998.

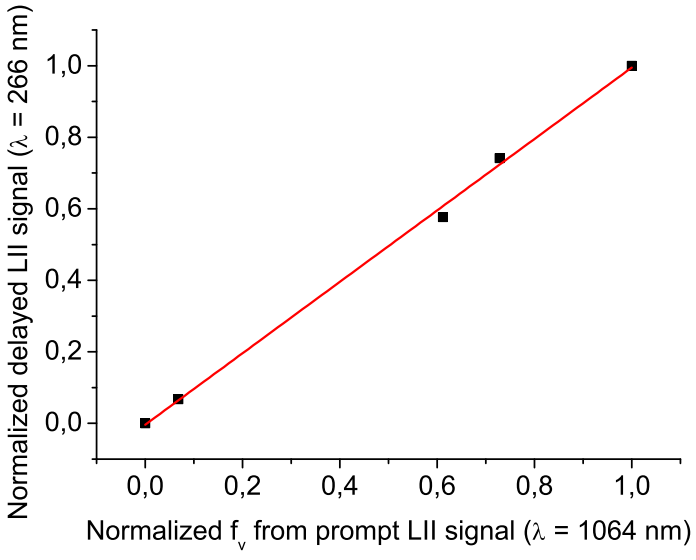

Figure 5.10: Correlation between the normalized delayed LII signal (obtained upon 266 nm excitation) and soot volume fraction (obtained from prompt LII at 1064 nm excitation) in in n-heptane flames. Black squares: experimental data in the range of $3.7 \leq \phi \leq 8.5$. Red line: linear fit $y = ax + b$, with b≠0 and R^2=0.997.

5.4 Conclusions

Partially premixed flames of the surrogate fuels n-heptane and n-decane were characterized in an experimental setup capable of burning vaporized liquid fuels in laminar coflow flames. The LIF and LII techniques were applied to measure qualitative profiles of OH, PAH and soot, as well as quantitative soot volume fractions. The results illustrate that a combination of LIF and LII using both 266 nm and 1064 nm as excitation wavelengths can provide unambiguous spatial identification of PAH and soot in laminar flames.

We have demonstrated that there is a good linear correlation between f_v, obtained using prompt detection and excitation at 1064 nm, and both PAH LIF and delayed (50 ns) LII signals obtained upon excitation with 266 nm. This result particularly suggests that, if one is interested only in a comparison of soot formation characteristics for a large range of flame conditions and fuels, it can be done with one optical setup arrangement using 266 nm as the excitation wavelength.

Possible issues related to the use of high-power UV excitation (photo-chemical processes) and delayed signal detection (influence on particle size) for PAH and soot measurements, are not significant for the flame conditions studied here. Also, these delayed and prompt measurements of LII signals seem to spatially match, suggesting good synchronization between the different optical setups and a good flame repeatability of the HPVB setup.

Bibliography

[1] M.D. Smooke, Y. Xu, R.M. Zurn, P. Lin, J.H. Frank, and M.B. Long. Computational and experimental study of OH and CH radicals in axisymmetric laminar diffusion flames. *in: Twenty-Fourth International Symposium on Combustion, The Combustion Institute, Pittsburgh*, pages 813–822, 1992.

[2] C.S. McEnally, A.M. Schaffer, M.B. Long, L.D. Pfefferle, M.D. Smooke, M.B. Colket, and R.J. Hall. Computational and experimental study of soot formation in a coflow, laminar ethylene diffusion flame. *The Combustion Institute*, 27th symposium on Combustion:1497–1505, 1998.

[3] K.T. Walsh, J. Fielding, M.D. Smooke, and M.B. Long. Experimental and computational study of temperature, species, and soot in buoyant and non-buoyant coflow laminar diffusion flames. *Proceedings of the Combustion Institute*, 28: 1973–1979, 2000.

[4] C.S. McEnally, L.D. Pfefferle, A.M. Schaffer, M.B. Long, R.K. Mohammed, M.D. Smooke, and M.B. Colkei. Characterization of a coflowing methane/air nonpremixed flame with computer modeling, Rayleigh-Raman imaging, and on-line mass spectrometry. *Proceedings of the Combustion Institute*, 28(2063-2070), 2000.

[5] M.D. Smooke, R.J. Hall, M.B. Colket, J. Fielding, M.B. Long, C.S. McEnally, and L.D. Pfefferle. Investigation of the transition from lightly sooting towards heavily

sooting co-flow ethylene diffusion flames. *Combustion Theory and Modelling*, 8: 593–606, 2004.

[6] M.D. Smooke, C.S. McEnally, L.D. Pfefferle, R.J. Hall, and M.B. Colket. Computational and experimental study of soot formation in a coflow, laminar diffusion flame. *Combustion and Flame*, 117(117-139), 1999.

[7] M.D. Smooke, M.B. Long, B.C. Connelly, M.B. Colket, and R.J. Hall. Soot formation in laminar diffusion flames. *Combustion and flame*, 143:613–628, 2005.

[8] Chevron. Motor gasolines technical review. Technical report, Chevron, San Ramon, CA, USA, 2007.

[9] Chevron. Diesel fuels technical review. Technical report, Chevron, San Ramon, CA, USA, 2007.

[10] J.T. Farrell, N.P. Cernansky, F.L. Dryer, D.G. Friend, C.A. Hergart, C. K. Law, R.M. McDavid, C.J. Mueller, A.K. Patel, and H. Pitsch. Development of an experimental database and kinetic models for surrogate diesel fuels. *SAE paper 2007-01-0201*, 1, 2007.

[11] M.H. de Andrade Oliveira, C.C.M. Luijten, and L.P.H. de Goey. Soot measurements in laminar flames of gaseous and (prevaporized) liquid fuels. *Proceedings of the 4^{t}h ECM (European Combustion Meeting), Editors: P. Szentannai and F. Winter, Vienna, Austria*, 117, 2009.

[12] R.L. Vander Wal. Soot precursor material: visualization via simultaneous LIF-LII and characterization via TEM. *Twenty-Sixth Symposium (International) on Combustion/The Combustion Institute*, 78:2269–2275, 1996.

[13] R.L. Vander Wal, K.A. Jensen, and M.Y. Choi. Simultaneous laser-induced emission of soot and polycyclic aromatic hydrocarbons within a gas-jet diffusion flame. *Combustion and Flame*, 109:399–414, 1997.

[14] R.L. Vander Wal. Soot precursor carbonization: Visualization using LIF and LII and comparison using bright and dark field TEM. *Combustion and Flame*, 112: 607–616, 1998.

[15] F. Cignoli, S. Benecchi, and G. Zizak. Time-delayed detection of laser-induced incandescence for the two-dimensional visualization of soot in flames. *Applied Optics*, 33:5778–5782, 1994.

[16] H. Bladh, J. Johnsson, and P.-E. Bengtsson. On the dependence of the laser-induced incandescence (LII) signal on soot volume fraction for variations in particle size. *Applied Physics B*, 90(1):109–125, 2008.

[17] C. Schulz, B.F. Kock, M. Hofmann, H. Michelsen, S. Will, B. Bougie, R. Suntz, and G. Smallwood. Laser-induced incandescence: recent trends and current questions. *Applied Physics B*, 83:333–354, 2006.

[18] F. Beretta, A. D'Alessio, A. D'Orsi, and P. Minutolo. Modeling non-premixed laminar co-flow flames using flamelet-generated manifolds. *Combustion Science and Technology*, 85:455–470, 1992.

[19] L. Petarca and F. Marconi. Fluorescence spectra and polycyclic aromatic species in a n-heptane diffusion flame. *Combustion and Flame*, 78:308–325, 1989.

[20] C.S. McEnally and L.D. Pfefferle. Experimental study of nonfuel hydrocarbons and soot in coflowing partially premixed ethylene/air flames. *Combustion and Flame*, 121:575–592, 2000.

[21] J. Zerbs, K.P. Geigle, O. Lammel, J. Hader, R. Stirn, R. Hadef, and W. Meier. The influence of wavelength in extinction measurements and beam steering in laser-induced incandescence measurements in sooting flames. *Appl Phys B*, 96: 683–694, 2009.

CHAPTER 6

Soot, PAH and OH measurements in doped methane flames

During the process of biomass gasification tars are formed which exit the gasifier in vapor phase. Tar condensation creates problems like fouling and plugging of after-treatment, conversion and end-use equipment. Gasification tars consist mainly of Polycyclic Aromatic Hydrocarbons (PAHs). Former research has shown the possibilities and difficulties of tar conversion by partial combustion. Basic studies to investigate the oxidation of tars in non-premixed combustion processes are expected to give more insight in this problem. In this paper the ability of the flamelet-generated manifold (FGM) approach to numerically model multi-dimensional, laminar, non-premixed flames with the inclusion of PAH chemistry is investigated. Modeling detailed PAH chemistry requires the employment of large reaction mechanisms which lead to expensive numerical calculations. The application of a reduction technique like FGM leads to a considerable decrease (up to two orders) in the required computation time. A 1D numerical validation shows that the improvements achieved by implementing a varying Lewis number for the progress variable $\mathcal{Y}$ are significant for PAH species with a large Lewis number, such as $C_{10}H_8$. Considerable improvements are found near the flame front and on the fuel side of the flame. A comparison has been made of FGM results with qualitative Planar Laser Induced Fluorescence (PLIF) measurements. A laminar CH_4/N_2-air co-flow flame has been doped with two dopants, being benzene and toluene, at three different concentrations. A set of filters has been used in order to qualitatively distinguish the small (1-2 rings) and large (3 or more rings) aromatic species. The results show that the model is able to capture the major flame characteristics typical for PAH formation in multi-dimensional laminar non-premixed flames.

The contents of this chapter have been submitted to the Proceedings of the Combustion Institute. The author contributed with the experimental work.

L.M. Verhoeven, M.H. de Andrade Oliveira, A. Lantz, B. Li, Z.S. Li, C.C.M. Luijten, J.A. van Oijen, M. Aldén, L.P.H. de Goey. Tar conversion in biogas by partial combustion: a numerical and experimental study of Polycyclic Aromatic Hydrocarbons in a laminar diffusion flame. *Preprint submitted to Proceedings of the Combustion Institute in December 23, 2011.*

6.1 Introduction

Civilization has become aware that fossil fuel stocks are finite. This led to an increasing interest in sustainable energy sources. A promising renewable conversion technique is biomass gasification. The resulting gas is called producer gas or syngas and is itself a fuel. During biomass gasification, tars are formed which exit the gasifier in vapor phase. These tars mainly consist of Polycyclic Aromatic Hydrocarbons (PAHs). Tars tend to condense and then gradually carbonize or polymerize until solid (soot) particles are formed [1]. Tar condensation causes problems like fouling and plugging of after-treatment, conversion and end-use equipment, which hampers the wide-spread application of biomass gasification. Tar formation during the thermal decomposition of biomass cannot be avoided. Therefore, it is of importance to convert or remove the tars at high temperature, before condensation takes place.

Studies by Houben *et al.* [2] and Van der Hoeven *et al.* [3] have demonstrated the possibility to remove naphthalene, a tar model component, from producer gas at high temperature by means of introducing a limited amount of air (with an air ratio $\lambda \approx 0.20$). During the experiments air was fed continuously through several nozzles into a partial combustion reactor creating multiple diffusion flames. These multiple (inverse) diffusion flames create local radical pools and a rise in temperature. It is believed that due to the mixing of these radicals with the remaining producer gas the naphthalene is converted to smaller hydrocarbons. These past studies have shown the possibilities and difficulties of tar conversion by partial combustion, leaving questions unanswered. To further investigate the conversion of tars in partial combustion reactors, a numerical model is developed. In this paper, we present a numerical model for tar/PAH chemistry in laminar diffusion flames. For validation, the results are compared with laser-diagnostic measurements of PAH in coflow diffusion flames doped with tar model compounds.

Modeling of tar conversion in partial combustion reactors requires the use of detailed chemistry models in two or even three dimensional simulations. Reaction mechanisms that describe the complicated PAH chemistry with sufficient detail, usually contain several hundreds of reactions between more than hundred species. This leads to a huge computational cost. Multiple methods, which are referred to as reduction techniques, have been developed to reduce the computational cost by eliminating fast chemical processes and as such the number of degrees of freedom of the problem [4–6]. Each method identifies the fast chemical processes in a different manner. Here we consider the flamelet-generated manifold (FGM) reduction technique which decouples chemical kinetic processes from the main flow and mixing processes by solving a set of one-dimensional (1D) flamelet equations [7]. This method has been extensively studied in simulations of premixed and non-premixed flames, both laminar and turbulent [8–12]. In the present work, the FGM approach is investigated for the modeling of PAH chemistry in non-premixed flames. Since the molar mass of PAHs is much larger than that of the major combustion species, the diffusivity of PAHs is significantly smaller, resulting in preferential diffusion effects. From a modeling perspective, preferential diffusion of PAHs has been rarely studied. The study presented in this paper focuses on the numerical and experimental validation of FGM in a laminar diffusion flame with the inclusion of detailed PAH chemistry. The first part focuses on a numerical validation in a 1D steady laminar CH_4/N_2-air counterflow flame. In

the second part, two-dimensional laminar diffusion flames doped with benzene and toluene — considered as tar representatives — are modeled with FGM and compared to measurements. Experiments have been executed to measure the distribution of OH and PAHs with Planar Laser-Induced Fluorescence (PLIF) in several doped flames.

6.2 Numerical approach

In the FGM approach, a low-dimensional manifold is created from solutions of the so-called flamelet equations. This set of 1D equations has been derived from the full set of 3D transport equations [13] and it describes conservation of mass, species and enthalpy in a flame-adapted coordinate system. For further details the reader is referred to [12]. In this study a series of counterflow diffusion flamelets is used to create a 2D manifold which is parameterized by two controlling variables. A natural selection of the control variables is the mixture fraction Z and a reaction progress variable $\mathcal{Y}$, so $\phi = \phi(Z, \mathcal{Y})$, in which ϕ can denote any thermo-chemical variable. Although any choice that results in a single-valued function is possible, the reaction progress variable is chosen here as a linear combination of the mass fractions of the main products and hydrogen: $\mathcal{Y} = \alpha_{\mathrm{CO_2}} Y_{\mathrm{CO_2}} + \alpha_{\mathrm{H_2O}} Y_{\mathrm{H_2O}} + \alpha_{\mathrm{H_2}} Y_{\mathrm{H_2}}$. The weight factors are chosen to be $\alpha_i = 1/M_i$.

The diffusion fluxes are modeled by assuming a constant Lewis numbers for each species: $Le_i = c_i$. The Lewis numbers are retrieved from a 1D flame simulation employing a complex transport model. Traditionally, the progress variable $\mathcal{Y}$ is transported without the inclusion of preferential diffusion ($Le_{\mathcal{Y}} = 1$). Here, we examine what the influence on the results is, if preferential diffusion is taken into account by assuming a variable Lewis number $Le_{\mathcal{Y}} = Le_{\mathcal{Y}}(Z, \mathcal{Y})$. As the controlling variable $\mathcal{Y}$ is a linear combination of species mass fractions, the diffusive flux of $\mathcal{Y}$ in a flamelet is given by a linear combination of the diffusion fluxes of the species:

$$\frac{1}{Le_{\mathcal{Y}}} \frac{\partial \mathcal{Y}}{\partial x} = \sum_i \frac{\alpha_i}{Le_i} \frac{\partial Y_i}{\partial x}. \tag{6.1}$$

Assuming a Fick-like diffusion model for $\mathcal{Y}$, the Lewis number can be determined as follows [12]:

$$\frac{1}{Le_{\mathcal{Y}}} = \left(\frac{\alpha_{\mathrm{H_2}}}{Le_{\mathrm{H_2}}} \frac{\partial Y_{\mathrm{H_2}}}{\partial x} + \frac{\alpha_{\mathrm{H_2O}}}{Le_{\mathrm{H_2O}}} \frac{\partial Y_{\mathrm{H_2O}}}{\partial x} + \frac{\alpha_{\mathrm{CO_2}}}{Le_{\mathrm{CO_2}}} \frac{\partial Y_{\mathrm{CO_2}}}{\partial x} \right) \left(\frac{\partial \mathcal{Y}}{\partial x} \right)^{-1} \tag{6.2}$$

in which we have used the present choice of $\mathcal{Y}$. The parameter $1/Le_{\mathcal{Y}}$ has been calculated for every single flamelet and tabulated as a function of the two controlling variables. The FGM databases used in this study are discretized on a 201×201 ($Z \times \mathcal{Y}$) equidistant grid. Data has been retrieved from these databases using bilinear interpolation. The solution of Z and $\mathcal{Y}$ is used in a postprocessing step to retrieve all parameters of interest from the manifold.

6.3 Burner configuration

The diffusion flame is created in a co-flow burner with a fuel tube inner diameter of 4 mm and an oxidizer coflow inner diameter of 50 mm. In the fuel tube flows a

Table 6.1: Experimental conditions.

Nr.	Dopant species	Concentration
1	No dopant	-
2	Benzene C_6H_6	1333 ppm
3	Benzene C_6H_6	2000 ppm
4	Benzene C_6H_6	2667 ppm
5	Toluene C_7H_8	1121 ppm
6	Toluene C_7H_8	1667 ppm
7	Toluene C_7H_8	2222 ppm

mixture of 55 V% methane and 45 V% nitrogen, and the co-flow consists of air. In the experiments, methane and nitrogen are supplied from high-purity gas cylinders and air from a compressor. All gases are metered with calibrated mass flow controllers (Bronkhorst, EL-FLOW type) with absolute uncertainties in the flow rates of ±5%. The flames investigated in this work showed good stability with a maximum standard deviation of 1.7% of the total flame height over time. A syringe pump system (pump = model SP100i; syringe= Hamilton 100μL) is used to inject the two dopants (benzene or toluene) in the fuel line at three different flow rates. The dopants purity is 99.8% (Sigma Aldrich). The fuel line was heated to 323 K before and after the injection point down to the bottom of the burner, to assist vaporization of the dopants and prevent condensation. At this temperature and the highest flow rate applied, the saturated vapor pressure of benzene is 2 orders of magnitude higher than its partial pressure in the fuel mixture (0.362 bar vs 0.0026 bar). The dopant concentrations of the seven studied flames are listed in table 6.1. As a reference, all measurements have been executed (in addition to the doped flames) on a flame without dopant. This flame is defined as the *base flame* (nr. 1 in table 6.1).

Numerically, the flame is described within a 2D axisymmetric domain by using an unstructured mesh containing 50.000 grid cells. Several grid size studies have shown that an applied grid cell size of 3 to 6 $\times$ 10^{-5} m in the region of the flame front is adequate [12]. The size of the numerical domain is 0.075 $\times$ 0.025 m. The stoichiometric mixture fraction is $Z_{\mathrm{st}} = 0.124$. The oxidizer (air) stream enters the geometry with a temperature of 300 K. The fuel stream enters the geometry with a temperature of 323 K. The flow in the fuel tube is prescribed by a parabolic velocity profile with a maximum of 0.58 m/s. The coflow is modeled by a plug flow with a constant velocity of 0.25 m/s. No-slip conditions are applied at the outer wall (radius $r = 0.025$ m). The outlet is modeled with an outflow boundary condition, assuming a zero normal gradient for all flow variables except pressure. The so-called ABF reaction mechanism [14, 15] (101 chemical species and 544 reactions) has been employed to compute the flamelets. Since toluene chemistry is not present in the ABF mechanism, the so-called Richter mechanism [16] (158 chemical species and 872 reactions) is employed for the flamelet calculations in which the fuel is doped with toluene.

6.4 1D numerical validation

In order to validate the FGM implementation, 1D steady laminar CH_4/N_2-air stagnation flames have been computed with $Le_i = c_i$. Results of detailed chemistry are compared with results obtained by using FGM. In this validation study C_6H_6 (2667 ppm) has been added to the fuel (55 %V CH_4, 45 %V N_2). When applying FGM, the following two transport equations, apart from the momentum equations, are solved for Z and $\mathcal{Y}$:

$$\vec{\nabla}\left(\rho\vec{u}Z\right) = \vec{\nabla}\left(\frac{\lambda}{c_p}\vec{\nabla}Z\right) \tag{6.3}$$

$$\vec{\nabla}\left(\rho\vec{u}\mathcal{Y}\right) = \vec{\nabla}\left(\frac{1}{Le_{\mathcal{Y}}}\frac{\lambda}{c_p}\vec{\nabla}\mathcal{Y}\right) + \omega_{\mathcal{Y}} \tag{6.4}$$

with $\omega_{\mathcal{Y}}$ being the source term for $\mathcal{Y}$, λ the thermal conductivity and c_p the heat capacity. The source term is composed from the source terms of the selected species CO_2, H_2O and H_2 and tabulated as a function of Z and $\mathcal{Y}$. The solution of Z and $\mathcal{Y}$ is used in a postprocessing step to retrieve all parameters of interest from the manifold. A comparison is made between the detailed solution employing the full chemistry model (FC), a non-premixed FGM (np-FGM) where $Le_{\mathcal{Y}} = 1$, and a non-premixed FGM with $Le_{\mathcal{Y}} = f(Z, \mathcal{Y})$ (np-FGM2). Calculations have been executed at a range of strain rates. The results for the mass fractions of $C_{10}H_8$, $C_{14}H_{10}$, and $C_{16}H_{10}$ at two different strain rates: $a = 0.10$ and 100 s^{-1}, can be seen in Fig. 6.1. A recent publication [12] has shown the performance of the inclusion of a Lewis number for $\mathcal{Y}$ for main species such as H_2, and OH. The results in Fig. 6.1 show that the improvements achieved by implementing a varying Lewis number for $\mathcal{Y}$ ($Le_{\mathcal{Y}} = f(Z, \mathcal{Y})$) are significant for PAH species with a large Lewis number. The Lewis numbers of the shown species $C_{10}H_8$, $C_{14}H_{10}$, and $C_{16}H_{10}$ are respectively 2.99, 3.66, and 3.94. Considerable improvements are found near the flame front and on the fuel side of the flame. The results validate the FGM approach for the modeling of laminar, non-premixed flames with the inclusion of detailed PAH chemistry and preferential diffusion. Comparing FGM results to experimental data does not derogate this, since the accuracy of a reduced chemistry model is always limited by the accuracy of the detailed model on which it is based.

6.5 Experimental measurements

Planar laser-induced fluorescence was used to visualize OH radicals using 283 nm, and PAHs using 266 nm excitation. Figure 6.2 shows the experimental setup used for all measurements. For the OH measurements, a dye laser (Continuum ND60, Rhodamine 590) is pumped by the second harmonic radiation (532 nm) of a Nd:YAG laser (Spectra-Physics, PRO-290). The output of the dye laser (566 nm) is frequency-doubled to 283 nm to excite the OH radical. The 283 nm laser is guided by two dichroic mirrors and formed into a 3.5 cm high laser sheet (positioned 1 mm above the burner tip) by a collection of cylindrical and spherical lenses. The $Q_1(8)$ line belonging to the $A^2\Sigma^+$ - $X^2\Pi(1,0)$ band is excited and the fluorescence at around 308 nm is collected by an ICCD camera (Princeton PI-MAX, 1024 × 1024 pixels)

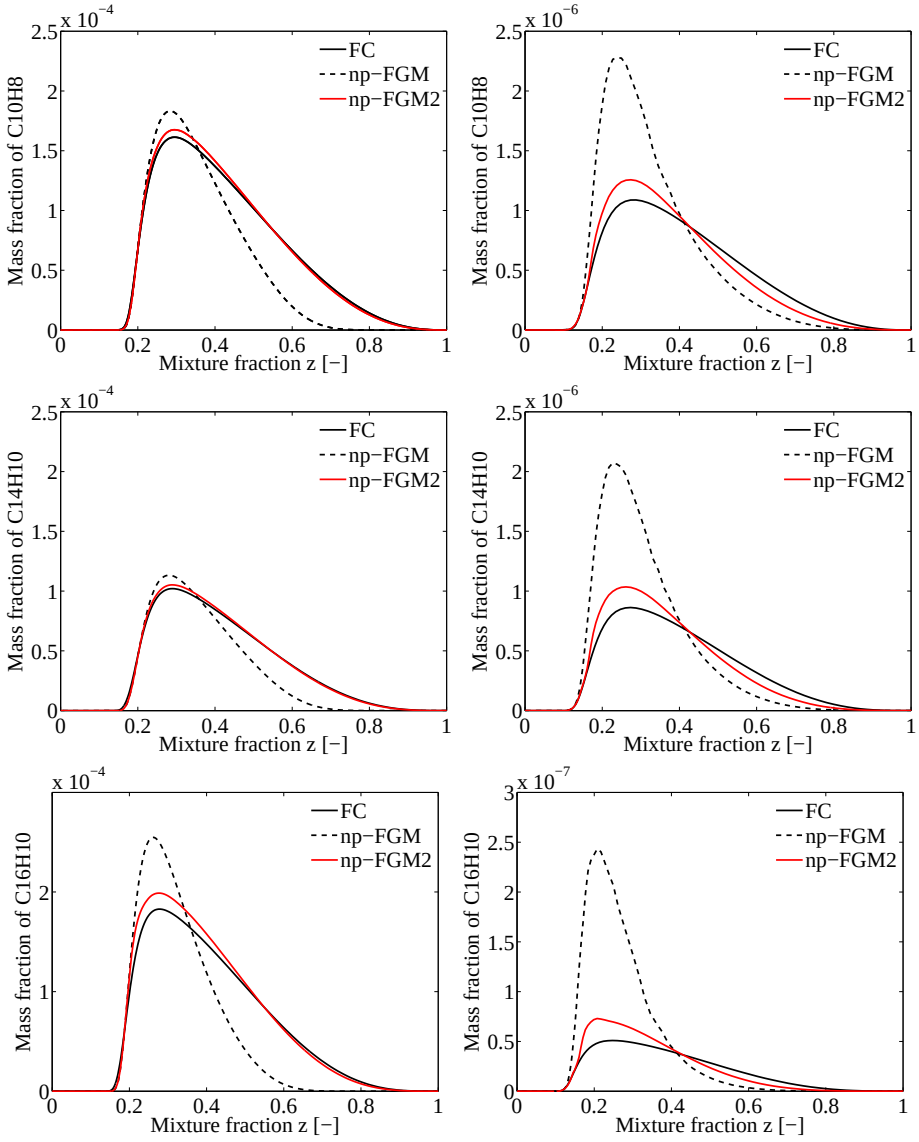

Figure 6.1: One-dimensional steady counterflow flamelet calculations with $Le_i = c_i$ for a strain rate $a = 0.10$ s^{-1} (left) and $a = 100$ s^{-1} (right). Profiles of the mass fractions of $C_{10}H_8$ (1st row), $C_{14}H_{10}$ (2nd row), and $C_{16}H_{10}$ (3rd row) are shown for the full chemistry solution (FC; solid black), non-premixed FGM simulations with $Le_{\mathcal{Y}} = 1$ (np-FGM; dashed), and non-premixed FGM simulations with $Le_{\mathcal{Y}} = f(Z,\mathcal{Y})$ (np-FGM2; solid red), as function of the mixture fraction Z.

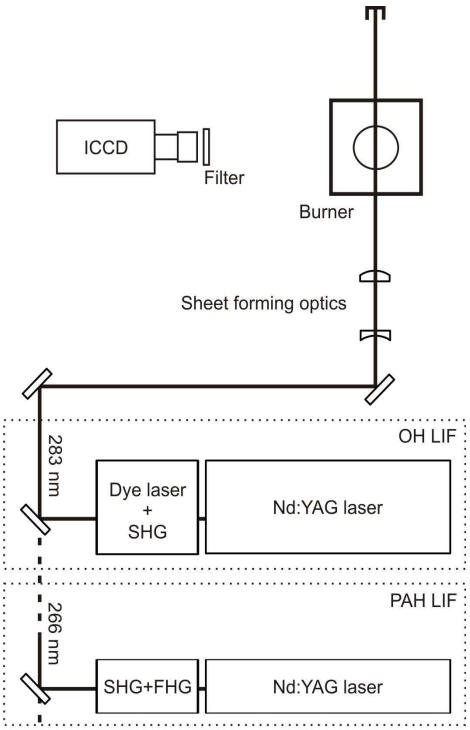

Figure 6.2: Experimental setup for OH and PAH PLIF. FHG and SHG stand for Fourth and Second Harmonic Generation, respectively.

equipped with a UV objective (UV Nikon, 100 mm focal length) and an interference filter (centered at 310 nm with FWHM of 10 nm).

For the PAH measurements, the 4^{th} harmonic at 266 nm from a Nd:YAG laser (Brilliant b, Quantel) is used. To detect the PAHs, the same laser sheet optics, ICCD camera and UV-lens are used as for OH PLIF. When using the strong 266 nm for excitation, there are contributions from both soot incandescence and PAH fluorescence in the detected signal. In order to distinguish these, two subsequent measurements are carried out: prompt detection (synchronized with the laser pulse) which contains both LIF and LII contributions; and delayed detection (50 ns after the laser pulse) which avoids the LIF signals from PAHs due to their short life time ($\simeq$ 15 ns). Although the prompt measurements thus contain some incandescence, it turned out to be negligible compared to the PAH signal. A liquid dimethylformamide filter is used in combination with the BG3 filter to suppress laser scattering and collect the fluorescence of PAH in the range of 300 to 500 nm. In some flames a set of filters are used, in order to qualitatively distinguish the small (1-2 aromatic rings) and large (3 or more aromatic rings) aromatic species which show characteristic fluorescence in the UV region and visible region, respectively [17, 18]. The filters used were: small aromatics: UG11 + WG320; large aromatics: GG420 + BG12. For all measurement conditions, 500 single shots were captured and averaged. Calculation from 500 single-shot measurements showed signal intensity variations of 7%.

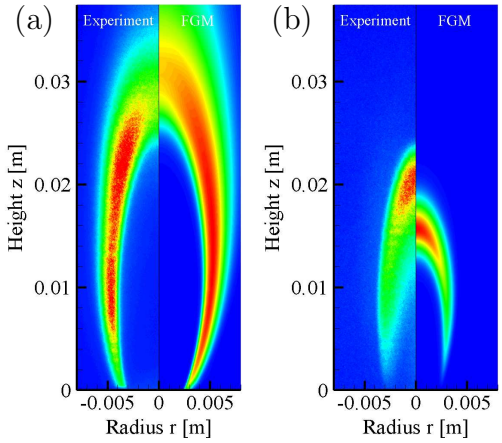

Figure 6.3: *Base flame (dopant-free)*; a) Comparison of OH PLIF signal (left) and calculated OH mass fraction (right). b) Comparison of PAH PLIF signal (left) and calculated PAH mass fraction (right). The color scheme is based on the normalization of both the signal strength (experiment) and the species mass fractions (numerical model).

6.6 Results

6.6.1 Contour plots

A contour plot of the OH PLIF signal strength (left), and the mass fraction of OH calculated by FGM (right) of the dopant-free *base flame* can be seen in Fig. 6.3a. Although the LIF signal strength is directly related to the species concentration, no statements can be made regarding the agreement of absolute concentrations [19]. For comparison both the experimental data and the FGM results have been normalized. The model predicts the flame tip, defined as the location of the maximum OH value on the center line, at a position 7% higher than the experimentally observed one. This small difference can be related to the difficulties in matching the correct boundary conditions from experiments for coflow flames [20–23]. Conduction and radiation from the flame to the burner in the experiments can cause noticeable preheating of both fuel and air inlet streams. Calculations in Ref. [20] have demonstrated that the flame height and local temperature can be significantly affected by the assumed inlet temperatures. Since the burner tip is not included in the present calculation, it is very likely that the fuel flow in reality is somewhat preheated, leading to a deviation in flame height.

Figure 6.3b shows a contour plot of the PAH PLIF signal (left) and a summation of calculated PAH mass fractions (right), in which PAH species are defined as species with a molar mass larger than that of benzene: $M_i \geq M_{C_6H_6}$. The FGM model results capture the lower part of the experimental profile. It is very likely that PAH species that have more than four aromatic rings, which are not included in the applied reaction mechanism, are present in the flame, possibly explaining the observed difference at higher heights.

The tendency of a flame to form PAH, which subsequently can lead to the formation of soot, is strongly dependent on the fuel structure [24]. The experimental results show that PAH distributions are found before the flame front, on the fuel side.

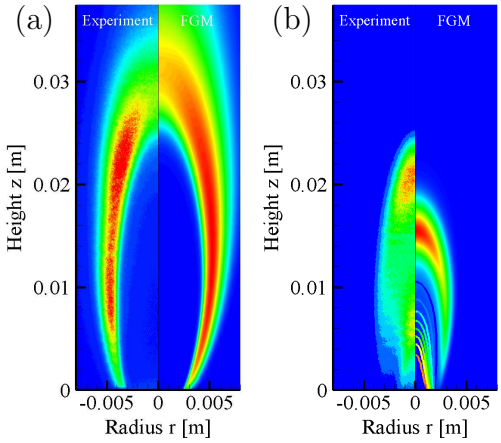

Figure 6.4: *Benzene doped flame* - 2667 ppm; a) Comparison of OH PLIF signal (left) and calculated OH mass fraction (right). b) Comparison of PAH PLIF signal (left) and calculated PAH mass fraction (right). The mass fraction of the dopant benzene has been made visible by colored iso-lines. The color scheme is based on the normalization of both the signal strength (experiment) and the species mass fractions (numerical model).

When quantities of benzene are added to the fuel (see Fig. 6.4), the results show no effect on the OH distribution and an increase of the PAH concentration, in respect to the base flame. Since addition of the first new ring is typically the rate-limiting step in the formation of larger PAHs, and subsequently soot [25], this increase in PAH concentration is to be expected. Furthermore, it appears that the LIF signal also captures smaller aromatic species like the dopant itself, since it is highly unlikely that benzene is converted to PAHs at the involved low temperatures in the region close to the burner exit. The experimentally observed cone is not visible in the model results, since the dopant itself is not included in the definition of the numerically computed PAH. To show the agreement between the measured PAH and the calculated benzene fraction, iso-lines of the computed dopant mass fraction are included in Fig. 6.4b on the right.

Also when toluene is applied as a dopant, a strong LIF signal is observed near the burner tip, visualizing the dopant (see Fig. 6.5a). The PAH concentrations near the flame tip are higher when toluene is added, than when benzene is applied as a dopant, when it is assumed that an increase in LIF signal strength is directly related to an increase in concentration. This increased tendency to form larger PAHs, which will subsequently lead to an increase in soot formation, is in line with experiments by McEnally *et al.* [24]. They determined sooting tendencies for a large number of aromatic hydrocarbons. Their results showed that, when toluene was added (400 ppm) to a fuel mixture, identical to the mixture applied in this study, a higher sooting tendency was found in comparison to benzene (400 ppm). This is confirmed here by LII measurements which have been executed in addition to the PLIF measurements. Soot volume fraction measurements obtained upon excitation at a wavelength of 1064 nm show that in the flame doped with toluene, soot is formed with a concentration which is one order of magnitude higher than in the flame doped with benzene.

The results obtained with the filter for small aromatic species (1-2 rings) are presented in Fig. 6.5b. The experimentally determined profile has been compared

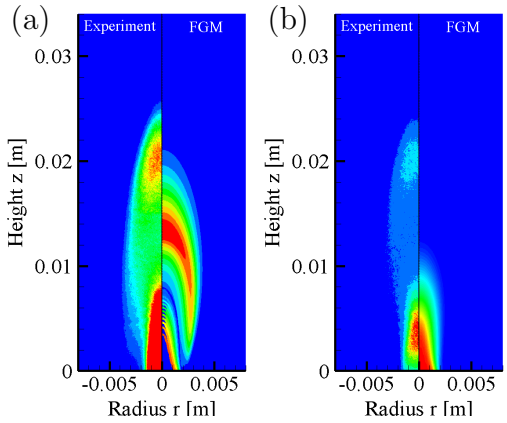

Figure 6.5: *Toluene doped flame - 2222 ppm*; a) Comparison of PAH PLIF signal (left), and calculated PAH mass fraction (right). The mass fraction of the dopant has been made visible by colored iso-lines. The color scheme is based on the normalization of both the signal strength (experiment) and the species mass fractions (FGM model). b) Comparison of the filtered (small aromatic species) PAH PLIF signal (left) with the numerical result showing the mass fraction of the dopant C_7H_8 (right).

with the sum of all calculated species mass fractions, which have a molar mass smaller than the 2-ring aromatic species naphthalene. In the lower region of the flame, the dopant species in the fuel, being toluene, seems to be responsible for the small cone visible at the burner tip.

The results obtained with the filter for large aromatic species are presented in Fig. 6.6. Figure 6.6a compares the profile found in the LIF experiments (left) with a summation of species mass fractions which can be referred to as 3-ring aromatic species found in the FGM results (right). The exact ring class definition is given in the next section. These results indicate that, in the experiments, PAH species are excited which contain more than three rings. A ring analysis on the centerline of the flame, which is presented further on in table 6.2, strengthens this assumption. The right figure shows the species mass fraction profile of 9,-anthryl $C_{14}H_9$, which has been found to be the species which can be found highest up in the modeled diffusion flame.

6.6.2 Centerline profiles

The mass fractions of all species have been retrieved from the applied manifold by using the numerical solution of Z and $\mathcal{Y}$ on the centerline. The mass fractions of species, with a molar mass larger than C_6H (hexatriynyl), have been summed, and this summation is referred to as the mass fraction of PAH. The dopant itself is not included in this summation. This PAH definition also includes species which are not poly-aromatic, but since their structure is closely related to the dopant species, their presence in the experiments is expected. The upper left panel in Fig. 6.7 shows the PAH distribution along the centerline in the base flame. The black dots represent the normalized LIF signal strength, and the solid line shows the normalized modeling results. Larger PAH species are expected to form higher up in the flame than smaller ones. The shift between the numerical results and experimental data can therefore be explained by the fact that no PAHs with more than four rings have been included

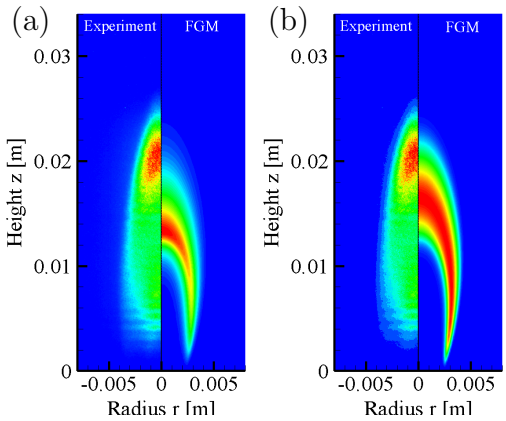

Figure 6.6: *Toluene doped flame - 2222 ppm*; (a) Comparison of the filtered (large aromatic species) PAH PLIF signal (left) with the numerical result showing the summed mass fraction of 3-ring species (right). (b) Comparison of the filtered (large aromatic species) PAH PLIF signal (left) with the numerical result showing the concentration of 9,-anthryl ($C_{14}H_9$) (right).

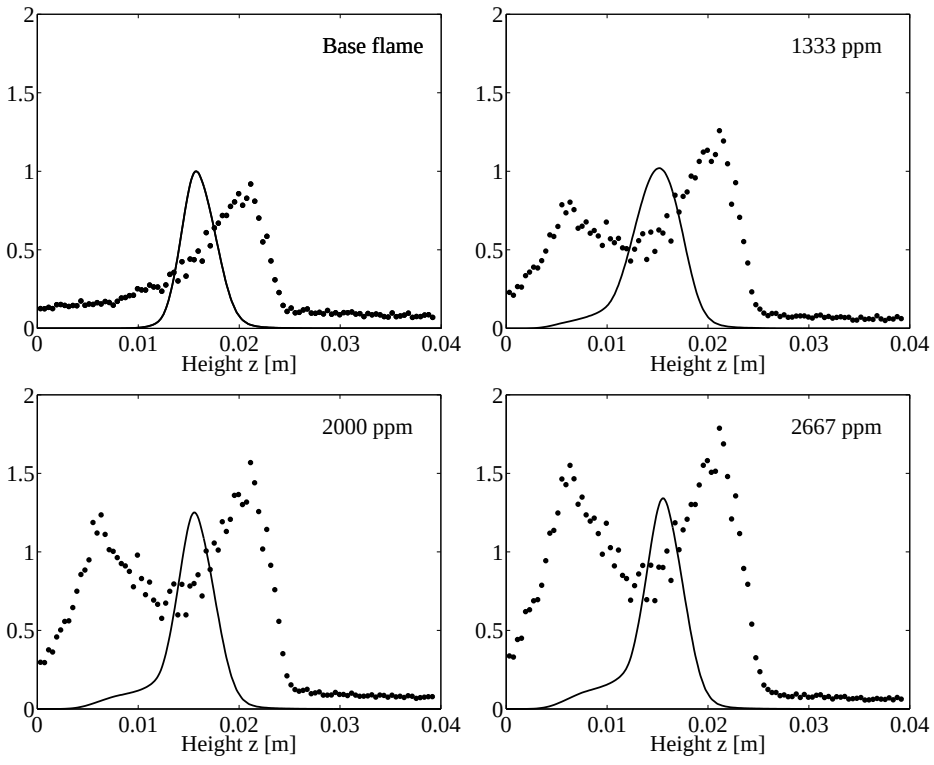

Figure 6.7: *Benzene doped flames* - Centerline profiles of the normalized experimental PAH LIF signal (black dots) and the mass fractions calculated by FGM (solid line) for different benzene additions. The upper left figure shows the PAH distribution in the base flame. The values have been normalized on the base flame results.

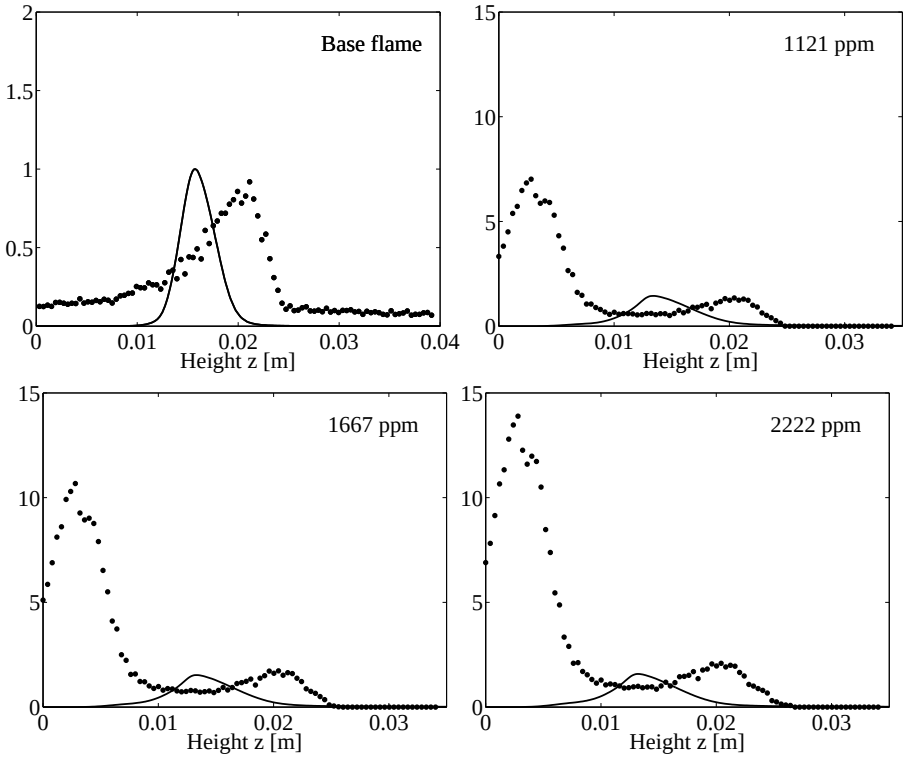

Figure 6.8: *Toluene doped flames* - Centerline profiles of the normalized experimental PAH LIF signal (black dots) and the mass fractions calculated by FGM (solid line) for different toluene additions. The upper left figure shows the PAH distribution in the base flame. The values have been normalized on the base flame results.

in calculation. The other three panels in Fig. 6.7 show the PAH distributions, when adding benzene at three concentrations (1333, 2000, and 2667 ppm). Both the experimental and the modeling results have been normalized using the base flame results. The experimental results show two peaks in the LIF signal, of which the first one is not present in the modeling results. This first peak corresponds to the dopant. The height of this peak is proportional to the amount of dopant in the fuel. The left flank of the peak is caused by the laser beam profile. Close to the burner the intensity of the laser sheet decreases resulting in lower LIF signals. Since the dopant is not included in the numerical PAH definition, the first peak is not observed in the numerical results.

The second peak corresponds to the PAH species which are formed just before the flame front. The height of this peak also increases with increasing amount of dopant, but not as much as the first peak. The computed PAH concentration shows the same trend. The second peak appears to lie on the right flank of the first one. If the height of the second peak is corrected for this background signal caused by the dopant itself, the relative increase in PAH concentration with increasing amount of dopant is in good agreement with the numerical predictions.

The results for the centerline distribution of PAHs when adding toluene, are shown in Fig. 6.8. For easy comparison, the upper left figure shows the base flame once more. As for the benzene doped flames, the experimental results show two peaks in the LIF signal. The first peak, which is related to the dopant, increases much stronger with

Table 6.2: Ring specification in terms of smallest and largest species and the position of maximum concentrations on the centerline for the 2667 ppm benzene doped flame

Group	Smallest species	Largest species	Height [cm]
1-ring	C_6H	C_6H_6F	1.44
2-ring	C_6H_7	$C_{10}H_8$	1.49
3-ring	$C_{11}H_9$	$C_{14}H_{10}$	1.60
4-ring	$C_{16}H_9$	$C_{16}H_{10}$	1.62

increasing dopant rate than in the case of benzene doped flames. This confirms that toluene results in much stronger LIF signals than benzene. The second peak, which corresponds to PAHs that are formed, increases with increasing amount of dopant. As in the case of benzene, the relative increase predicted by the model agrees with the experimental values after subtraction of the toluene baseline.

To further examine the species which are present in the modeled PAH profile, the species have been rearranged into four groups (see table 6.2): In this ring specification, the dopant species themselves are not included. Based on these criteria the PAH species, present in the reaction mechanism, have been rearranged in groups. Table 6.2 also lists the location of the maximum concentration of each group of rings. The results show that with increasing height an increase in aromatic rings is involved. This behavior is in line with the work of Lee *et al.* [26] in which the LIF fluorescence was detected with filters centered at 5 different wavelengths ranging from 330 to 500 nm. It was observed that when the detection wavelength of the PAH LIF becomes longer, the PAH profile shifts closer to the LII profile. Since PAHs grow from the fuel side toward the flame front and soot particles are formed from PAHs, it was concluded that PAH LIF signals measured at shorter (longer) wavelengths represent relatively smaller (larger) PAHs.

6.7 Conclusions

In this paper, the use of FGM for the modeling of PAH chemistry has been investigated. For the first time, FGM is used to model laminar non-premixed flames with the inclusion of PAH chemistry. The performance of FGM has been examined by both numerical and experimental validation. Since the diffusivity of PAH species is relatively small, additional attention has been given to the modeling of preferential diffusion. By using a non-unity Lewis number for the progress variable, preferential diffusion has been included in the FGM model. Validation against numerical results computed with detailed chemistry showed that this improves the PAH predictions significantly. The FGM model reproduces the results of the detailed model within several percent but with only a fraction of the computational cost. This reduction in computational cost makes it possible to employ very detailed PAH reaction mechanisms in multi-dimensional simulations by using FGM. The comparison of FGM results of 2D simulations of a coflow flame with experiments showed that the qualitative OH distributions found by the experiments and the FGM model are in good agreement. The

PAH profiles of both the experiments and the calculations showed agreement in the lower region of the flame. The location of the maximum PAH concentration found in the experiments disagreed with the simulations. This is attributed to the lack of PAH species with more than four aromatic rings in the employed reaction mechanisms. The experimentally observed growth of PAH concentration with increasing amount of dopant in the fuel, was also predicted by the numerical model. For both the benzene and toluene doped flames, the relative increase in PAH concentration was predicted with satisfactory accuracy. Although no quantitative comparison of the PAH concentrations could be made, the results show that the model is able to capture the major characteristics of PAH formation in a multi-dimensional laminar diffusion flame.

Acknowledgements

The financial support of SenterNovem, the Swedish Foundation for Strategic Research and Swedish Energy Agency through CECOST (Centre for Combustion Science and Technology) is gratefully acknowledged.

Bibliography

[1] B.J. Vreugdenhil and R.W.R. Zwart. Tar formation in pyrolysis and gasification. Technical Report ECN-E–08-087, Energy research Centre of the Netherlands, 2009.

[2] M. P. Houben, H. C. de Lange, and A. A. van Steenhoven. Tar reduction through partial combustion of fuel gas. *Fuel*, 84:817–824, January 2005.

[3] T. A. van der Hoeven, H. C. de Lange, and A. A. van Steenhoven. Analysis of hydrogen-influence on tar removal by partial oxidation. *Fuel*, 85:1101–1110, 2006.

[4] J. F. Griffiths. Reduced kinetic models and their application to practical combustion systems. *Prog. Energy Combust. Sci.*, 21:25–127, 1995.

[5] U. Maas and S. B. Pope. Simplifying chemical kinetics: Intrinsic low-dimensional manifolds in composition space. *Combust. Flame*, 88:239–264, 1992.

[6] S. H. Lam and D. A. Goussis. The csp method for simplifying kinetics. *Int. J. Chemical Kinetics*, 26:461–486, 1994.

[7] J. A. van Oijen and L. P. H. de Goey. Modelling of premixed laminar flames using flamelet-generated manifolds. *Combust. Sci. Technol.*, 161:113–138, 2000.

[8] J. A. van Oijen, F. A. Lammers, and L. P. H. de Goey. Modelling of complex premixed burner systems using flamelet-generated manifolds. *Combust. Flame*, 127:2124–2134, 2001.

[9] J. A. van Oijen and L. P. H. de Goey. Modelling of premixed counterflow flames using the flamelet-generated manifold method. *Combust. Theory Modelling*, 6: 463–478, 2002.

[10] J. A. van Oijen, R. J. M. Bastiaans, and L. P. H. de Goey. Low-dimensional manifolds in direct numerical simulations of premixed turbulent flames. *Proc. Combust. Inst.*, 31:1377–1384, 2007.

[11] S. Delhaye, L. M. T. Somers, J. A. van Oijen, and L. P. H. de Goey. Incorporating unsteady flow-effects in flamelet-generated manifolds. *Combust. Flame*, 155:133–144, 2008.

[12] L. M. Verhoeven, W. J. S. Ramaekers, J. A. van Oijen, and L. P. H. de Goey. Modeling non-premixed laminar co-flow flames using flamelet-generated manifolds. *Combust. Flame*, 159:230–241, 2012.

[13] L. P. H. de Goey and J. H. M. ten Thije Boonkkamp. A flamelet description of premixed laminar flames and the relation with flame stretch. *Combust. Flame*, 119:253–271, 1999.

[14] Jörg Appel, Henning Bockhorn, and Michael Frenklach. Kinetic modeling of soot formation with detailed chemistry and physics: laminar premixed flames of C_2 hydrocarbons. *Combust. Flame*, 121:122–136, 2000.

[15] H. Wang and M. Frenklach. A detailed kinetic modeling study of aromatics formation in laminar premixed acetylene and ethylene flames. *Combust. Flame*, 110:173–221, 1997.

[16] R.A. Shandross, J.P. Longwell, and J.B. Howard. Destruction of benzene in high-temperature flames: chemistry of benzene and phenol. *Proc. Combust. Inst.*, 26: 711–719, 1996.

[17] F. Beretta, A. D'Alessio, A. D'Orsi, and P. Minutolo. Modeling non-premixed laminar co-flow flames using flamelet-generated manifolds. *Combust. Sci. Technol.*, 85:455–470, 1992.

[18] J. Wu, K.H. Song, T. Litzinger, S.-Y. Lee, R. Santoro, M. Linevsky, M. Colket, and D. Liscinsky. Reduction of PAH and soot in premixed ethyleneair flames by addition of ethanol. *Combust. Flame*, 144:675–687, 2006.

[19] B.A.V. Bennett, C.S. McEnally, L.D. Pfefferle, and M.D. Smooke. Computational and experimental study of axisymmetric coflow partially premixed ethylene/air flames. *Combust. Flame*, 127:2004–2022, 2001.

[20] M. D. Smooke, C. S. McEnally, L. D. Pfefferle, R. J. Hall, and M. B. Colket. Computational and experimental study of soot formation in a coflow, laminar diffusion flame. *Combust. Flame*, 117:117–139, 1999.

[21] C.S. McEnally, L.D. Pfefferle, A.M. Schaffer, M.B. Long, R.K. Mohammed, M.D. Smooke, and M.B. Colket. Characterization of a coflowing methane/air non-premixed flame with computer modeling, rayleigh-raman imaging, and on-line mass spectroscopy. *Proc. Combust. Inst.*, 28:2063–2070, 2000.

[22] J.B. Bell, M.S. Day, J.F. Crcar, W.G. Bessler, C. Schulz, P. Glarborg, and A.D. Jensen. Detailed modleing and laser-induced-fluorescence imaging of nitric oxide in a NH_3-seeded non-premixed methane-air flame. *Proc. Combust. Inst.*, 29: 2195–2202, 2002.

[23] S.B. Dworkin, A.M. Schaffer, B.C. Connelly, M.B. Long, M.D. Smooke, M.A. Puccio, B. McAndrew, and J.H. Miller. Measurements and calculations of formaldehyde concentrations in a methane/N_2/air, non-premixed flame: Implications for heat release. *Proc. Combust. Inst.*, 32:1311–1318, 2009.

[24] Charles S. McEnally and Lisa D. Pfefferle. Improved sooting tendency measurements for aromatic hydrocarbons and their implications for naphthalene formation pathways. *Combust. Flame*, 148:210–222, 2007.

[25] Charles S. McEnally, Lisa D. Pfefferle, Burak Atakan, and Katharina Koshe Höinghaus. Studies of aromatic hydrocarbon formation mechanisms in flames: Progress towards closing the fuel gap. *Prog. Energy Combust. Sci.*, 32:247–294, February 2006.

[26] S.M. Lee, S.S. Yoon, and S.H. Chung. Synergistic effect on soot formation in counterflow diffusion flames of ethylenepropane mixtures with benzene addition. *Combust. Flame*, 136:493–500, 2004.

CHAPTER 7

Feasibility study: burning velocities at elevated pressures

The main goal of the work presented in this chapter is to demonstrate the feasibility of using the heat flux method in a high pressure environment. This is done by implementing the Heat Flux burner for elevated pressures as designed by Slikker [1] in the same High Pressure Vessel developed for coflow laminar flames studies, the HPVB.

7.1 Laminar burning velocity

The laminar burning velocity determines the rate at which a combustible mixture is consumed and it gives basic information about the diffusivity and reactivity of the flame. It is one of the key parameters when modeling laminar flames and is also the basis to determine the turbulent burning velocity that occurs in practical applications working under high pressure and temperature. For accurate prediction of combustion processes, chemical reaction mechanisms play an essential role. One way of verifying such mechanisms is to model laminar burning velocities and compare the results to experimental data.

Methane is the main component of Natural Gas (NG), which is a very important fuel in the production of electrical power and heat. Updated methane reaction mechanisms for higher pressures are required but available experimental data at these conditions are still scarce. Several methods have been developed to measure the laminar burning velocity of fuel/oxidizer mixtures. For high pressure measurements, the main methods applied are counterflow flames, conical Bunsen flames and spherically propagating flames.

In the counter-flow burner method, fuel and oxidizer streams flow towards one another and the flame front exists in the vicinity of the stagnation plane between them. The flames are stabilized through flame stretch which is controlled by adjusting the distance between the nozzles and/or the jet velocities. The velocity profile along the center line is then measured using PIV or Laser Doppler Velocimetry (LDV)

and extrapolated to a zero stretch rate, from which the laminar burning velocity (S_L) can be determined [2, 3].

The conical flames method is one of the first methods used to measure the burning velocity where a premixed flame is stabilized on a Bunsen burner. The cone angle is measured with a CCD camera and the burning velocity is determined from the relation between burning velocity and gas velocity, flame surface and burner diameter. The accuracy of this method depends on the optical method used to determine the flame surface and is also affected by the heat losses to the burner rim [4].

The constant volume bomb method is based on a freely propagating flame. In this method a (preferably spherical) combustion vessel is filled with a known fuel/oxidizer mixture that is ignited in the center. As a result, a spherical flame will propagate from the center towards the wall. Several methods can be used to determine (S_L), e.g. by measuring the pressure history inside the vessel, determining the density ratio of burnt and unburnt gas mixture or measuring the gas velocity by explosion. The results from these measuring methods need to be corrected for stretch before S_L is determined [5].

The heat flux method developed at Eindhoven University of Technology and first introduced by De Goey [6], does not require stretch corrections or extrapolation of data and therefore is a potential technique for measurements of laminar burning velocity also at elevated pressures. In this method, a premixed flat flame is stabilized on a perforated burner plate and an adiabatic state is achieved by adding heat to the unburnt gas mixture to compensate the heat loss from the flame needed for flame stabilization.

The heat balance of the heat flux burner is shown in Figure 7.1(a). The burner plate in this figure is sketched with only three holes for clarity. The net heat flux is responsible for the temperature profile of the burner plate and is determined as Φ_{net}=Φ_f-Φ_u, where Φ_f is the heat gain from the flame to the burner plate and Φ_u is the heat release from the burner plate to the unburnt mixture. For subadiabatic conditions ($v_g < S_L$), the net heat flux is larger than zero ($\Phi_{net} > 0$) and the flame is losing heat to the burner plate. In an extreme situation where $v_g \ll S_L$ the flame quenches or will enter the burner plate (flash-back). In the superadiabatic condition ($v_g > S_L$), the net heat flux is smaller than zero ($\Phi_{net} < 0$) and in extreme situations ($v_g \gg S_L$) the flame will blow off due to the limited time to consume the fuel/air mixture.

Figure 7.1(b) shows the axial temperature profiles of a freely propagating flame (T_{freely}) and a burner stabilized flame (T_{burner}). In this figure the thickness of the burner plate is x_p and the burner plate temperature is denoted by T_p. Bosschaart [7] has shown that the temperature gradient (dT_p/dx) over the burner plate is quite small compared to the gradient in the unburnt gases. Due to this fact and the very thin burner plate (1 mm), it can be assumed that the temperature gradient over the burner plate is negligible. In this way it is possible to perform one dimensional temperature measurements using thermocouples placed in the circular burner plate.

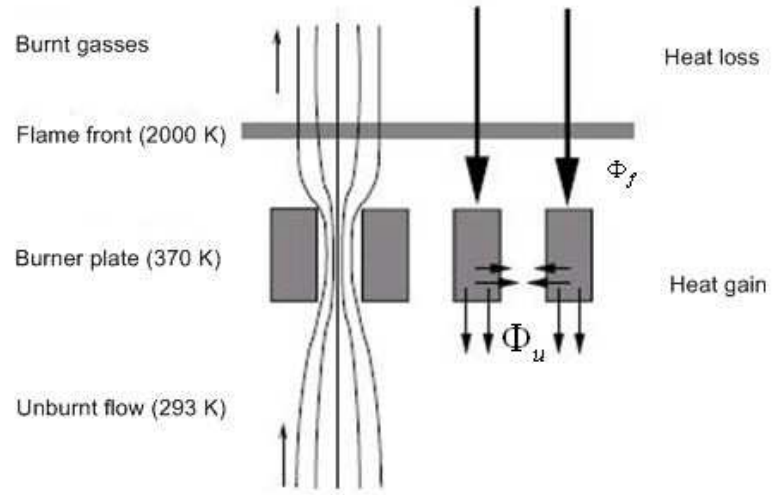

(a)

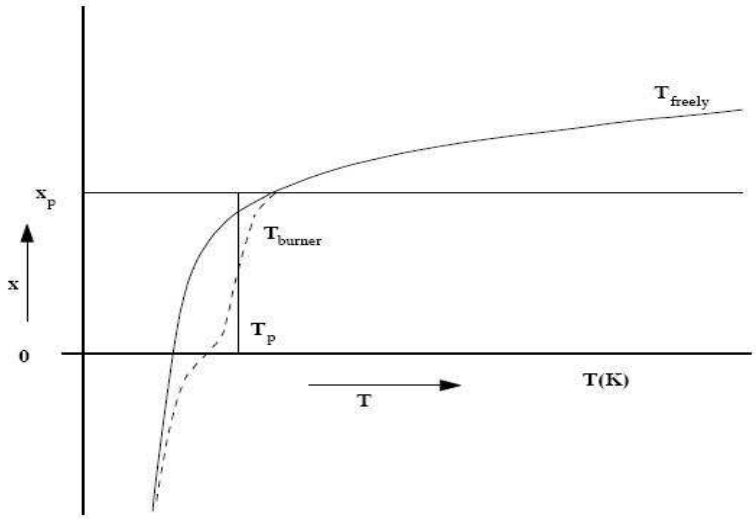

(b)

Figure 7.1: Schematic heat fluxes in the burner plate (a) and the temperature difference between a freely propagating flame and a burner stabilized flame with x_p as the plate thickness (b).

In the adiabatic situation the temperature profile is uniform in the radial direction. For subadiabatic inlet velocities the temperature in the center will be the highest. For superadiabatic velocities this temperature is the lowest, as theoretically derived by Bosschaart [7].

7.2 Experimental setup

A 3D sketch of the experimental setup assembly is shown in figure 7.2. The burner head and plenum chamber are the core of the heat flux burner and are made of brass.

The goal of the plenum chamber and burner head is to create a uniform flow at the outlet where the burner plate is placed. The burner was designed to withstand pressures up to 10 bar and was adapted to fit in the same pressure vessel as the coflow burner in the HPVB setup (see section 2.2 in chapter 2). There were two identical pressure vessels available, therefore, independent setups could be build.

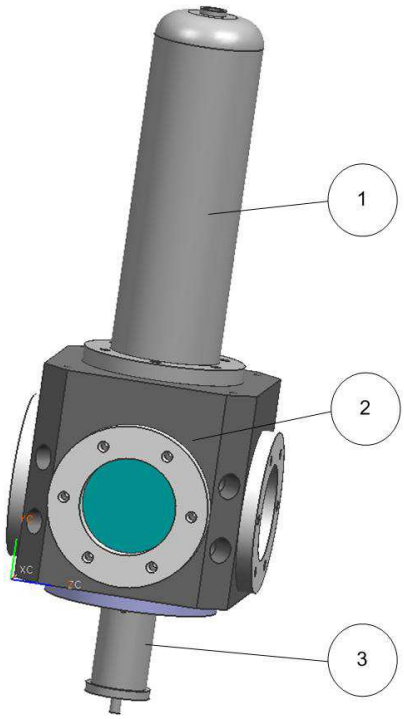

Figure 7.2: Total assembly of the burner, high pressure vessel and chimney: 1. Chimney 2. High pressure vessel 3. Heat flux burner.

In figure 7.3 a cross section and 3D view of an assembled burner is shown with three main components indicated by the colored boxes. The green box indicates the burner head, the red box the plenum chamber and the blue box shows the air-diffuser, which is wrapped around the burner head to lower the temperature in the high pressure vessel.

The burner plate is placed on top of the burner head (figure 7.3(a) (1)). Around the burner head an electrical microtubular heating element is wrapped with built-in type J thermocouple (iron/constantan, range -40 to +750 °C) (figure 7.3(a) (4)). The electrical heating is used to keep the burner plate at constant temperature (in this case approx. 90 °C). The temperature inside the pressure vessel should be maintained below 150 °C to avoid damages to sealing and teflon rings. A diffuser was initially designed and placed around the heating element to deliver a cold air co-flow and help to control the temperature inside the vessel. This measure turned out to cause disturbance to the flame due to a combined effect of the relatively high velocity of the jets with the small size of the vessel. However, it was still possible to perform the measurements for the range of pressure studied in this work (see also recommendations).

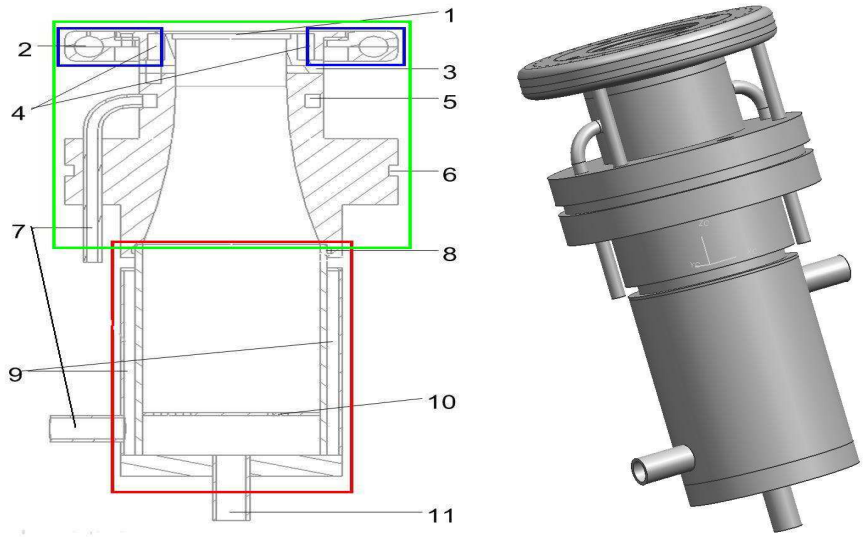

(a) Cross section view. (b) 3D view.

Figure 7.3: Burner head and plenum chamber, definition of parts. 1. Burner plate area, 2. Diffuser channel, 3. Insulating PEEK ring, 4. Chamber for electric heating element, 5. Cold water jacket, 6. O-ring, 7. Inlet cold water jacket 1, 8. O-ring, 9. Cold water jacket 2, 10. Perforated plate (flow straightener), 11. Inlet fuel/air mixture.

A peek ring insulates the hot burner head from the lower part of the burner (figure 7.3(a) (3)). The cold water jackets (figure 7.3(a) (5) and (7)) are used to keep the temperature of the incoming fuel/oxidizer flow (T_u) at constant temperature (25 °C) controlled by water baths. In the groove seen in figure 7.3(a) (6) an O-ring is placed to make the connection between the teflon ring and the burner leak tight. Another O-ring is placed between the teflon ring and the high pressure vessel for the same purpose. A perforated plate is used as flow straightener inside the plenum chamber (figure 7.3(a) (10)) to create a uniform flow. The holes in this plate have a diameter of 2 mm and a pitch of 4 mm. This perforated plate is placed at 1.5 cm from the bottom of the plenum chamber where the fuel/oxidizer mixture enters the burner.

The circular burner plate has an outer radius of 30 mm and contains more than 5000 holes placed in hexagonal configuration, as shown in figure 7.4(a). The holes have a diameter of 0.3 mm and the pitch is 0.4 mm. They were calculated by De Goey et al. [8] and simulated by Slikker [1] and are expected to give accurate results for pressures up to 10 bar. The temperature distribution of the burner plate is measured by thermocouples of type T (Copper-Constantan) that are placed directly in the holes of the burner plate with epoxy glue. The thermocouples are placed at the same height in the configuration shown in figure 7.4(b) with radial distances of 0, 3.2, 4.8, 8.0, 9.6, 11.2, 12.8 and 14.4 mm.

Figure 7.5 shows the layout of the gas supply. Gas flows are measured using calibrated Bronkhorst mass flow controllers (MFC's). For pressures up to 3.0 bar, a 4 L/min CH_4 MFC is used for methane and a 30 L/min CO MFC is used for air applying a conversion factor. For higher pressures a 7 L/min CH_4 MFC is used for

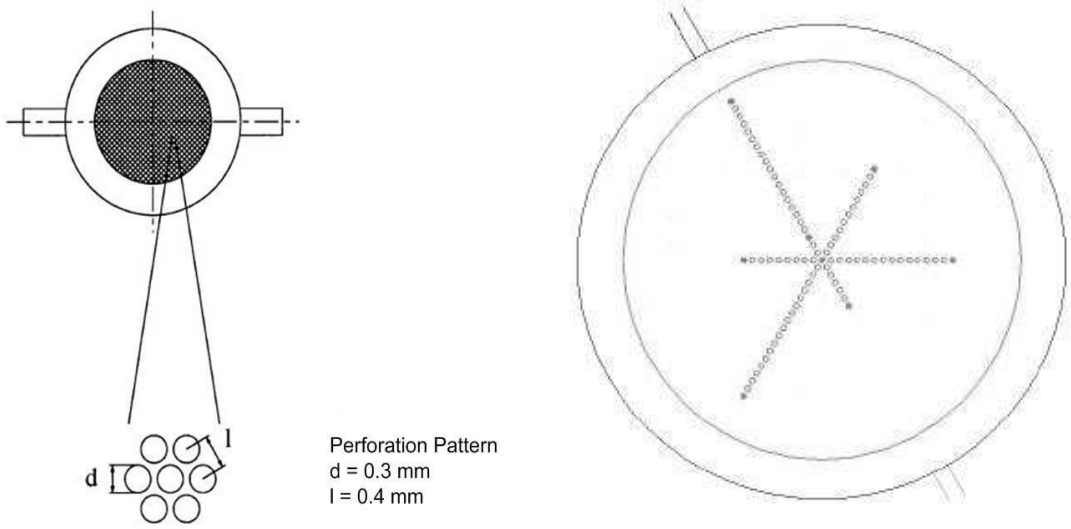

(a) (b)

Figure 7.4: Burner plate perforation pattern (a) and thermocouples configuration (b).

methane and an extra 15 L/min Air MFC, placed in parallel, is used for air supply. The change in the MFC's was necessary to cope with the increased power (i.e. higher mass flow) of the flame at higher pressures. All of the MFCs are tested and calibrated up to 8 bar.

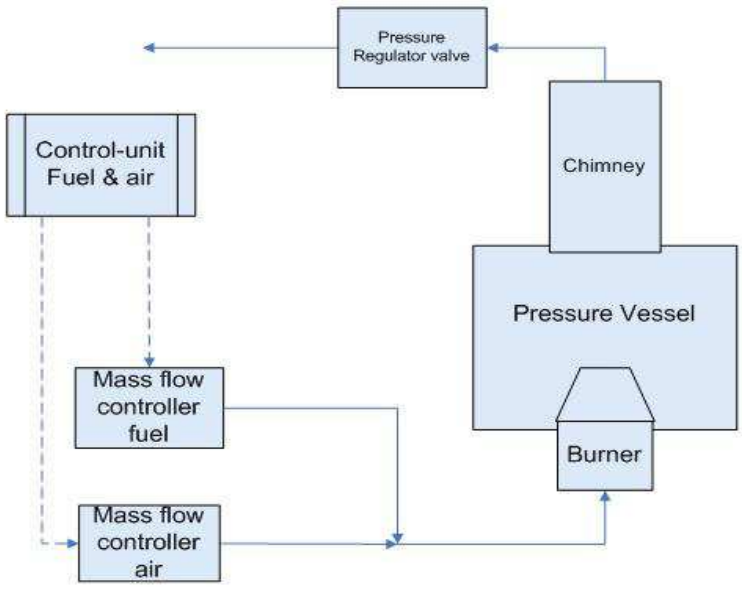

Figure 7.5: System layout for gaseous fuels.

The only measurement required in the heat flux method is the temperature profile of the burner plate for different gas velocities. The radial profile of temperature in the burner plate close to the adiabatic burning velocity is fitted by the method of

least squares to a polynomial of the form $T(r) = \alpha r^2 + \beta$. The coefficient α of such polynomials is plotted against sub and super adiabatic burning velocities. The adiabatic state is reached for zero value of the coefficient α. The procedure and model calculation for measuring the temperature and evaluating the burning velocity is described in more detail by Hermanns [9]. An example of the measured temperatures along the burner plate is given in figure 7.6 for a lean mixture of CH_4 and air at 3 atm and 298 K.

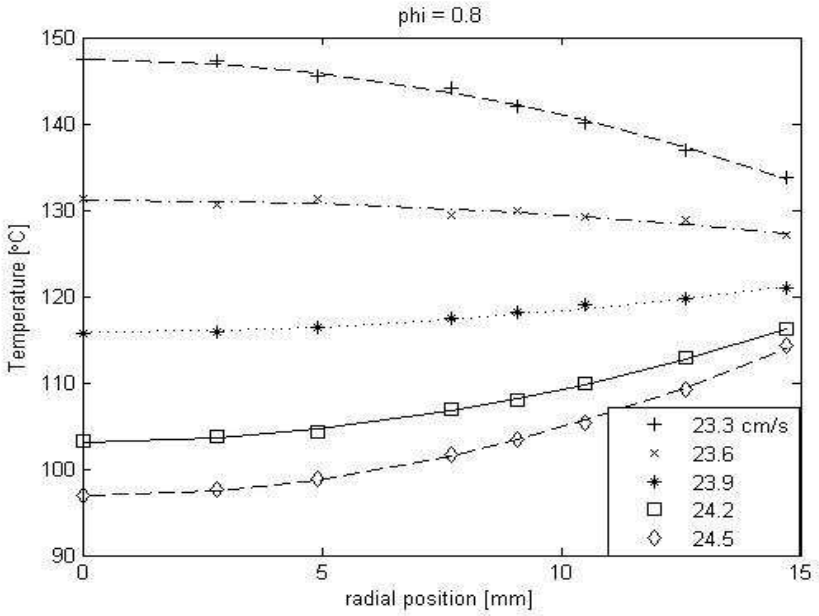

Figure 7.6: Example of radial temperature profiles across the burner plate at different gas velocities.

7.3 Results and discussions

The challenges faced during the first attempts to measure burning velocities at elevated pressure are described and analyzed (preliminary results section). Some possible measures to overcome the problems observed during these initial experiments are discussed. One of the considered measures is successfully implemented and the measurements at elevated pressure are performed and compared with the literature in the subsequent section.

7.3.1 Preliminary results

The heat flux burner was integrated to the high pressure vessel. Due to the relatively small size of the vessel in relation to the flow of gases inside the vessel, the pressure was always slightly higher than atmospheric pressure. Therefore, the measurements on premixed methane/air flames are performed for varying pressures starting from 1.5 up to 5 bar. This is done for equivalence ratios in the range of $0.8 \leq \phi \leq 1.4$.

During the preliminary tests, a visual flame analysis showed strong flame instabilities. Four different situations were distinguished to evaluate these flame instabilities having the adiabatic burning velocity as a reference. A stoichiometric flame at 2 bar is taken as an example of the typical flame instabilities observed, as described below. At this pressure, $S_L \simeq 29$ cm/s.

$u_g < S_L$: In the situation of subadiabatic conditions ($u_g \approx 27$ cm/s), the flame is heavily moving around and the blue color of the flame is not uniform (see figure 7.7(a)). There can be seen several sharp light blue contours when the rest of the flame presents somewhat darker blue. These contours and areas are not stable and move quite fast along the burner plate. This motion occurs in both vertical and horizontal direction and flame edges are lifted off.

$u_g \leq S_L$: In slightly subadiabatic condition ($u_g \leq 29$ cm/s), flame instabilities are still present. However, smoother light blue contours and lower lift off of the flame edges are observed when compared to the subadiabatic condition (figure 7.7(b)). Also, the movements in the vertical direction are weaker and in horizontal direction no movement is visually noticed.

$u_g \geq S_L$: In slightly superadiabatic condition ($u_g \geq 29$ cm/s), the flame showed good stability and a uniform and flat appearance (figure 7.7(c)) as it as expected and has been described by other authors [6, 7, 10, 11] to perform reliable measurements with the heat flux burner.

$u_g > S_L$: In superadiabatic condition ($u_g \approx 31$ cm/s) is close to the blow off limit and it was not possible to measure the temperature of the burner plate. It can be seen in figure 7.7(d) that the flame front presents sharp peaks all over the burner plate. The inlet velocity of the unburnt gas mixture is too high to stabilize the flame, which is no longer flat, on the burner plate.

When pressure is further increased, the magnitude of the flame instability also increased from subadiabatic to closer-to-adiabatic condition, however, the instabilities did not extend to the superadiabatic conditions up to 5 bar. Furthermore, some noise was noticed at various pressure and equivalence ratio conditions. Some possible physical phenomena causing these flame instabilities were considered:

Turbulence: the high pressure vessel was originally designed for small coflow flames with much lower power than the flat premixed flames realized with the heat flux burner. The relatively small size of the vessel in relation to these larger premixed flames can contribute to possible turbulent flow generated by recirculation of the flue gases inside the vessel. Glass tubes were placed around the flame serving as a protection shield for the flame. No significant changes on flame instabilities were observed.

Thermo-acoustic instabilities: fluctuations in the source of heat release can drive thermo-acoustic instabilities. Both fluctuations in equivalence ratio and in mass flux contribute to the heat release rate fluctuations. The behavior of a system including a combustion chamber is governed by the basic variables: (a) air/fuel ratio, (b) flame

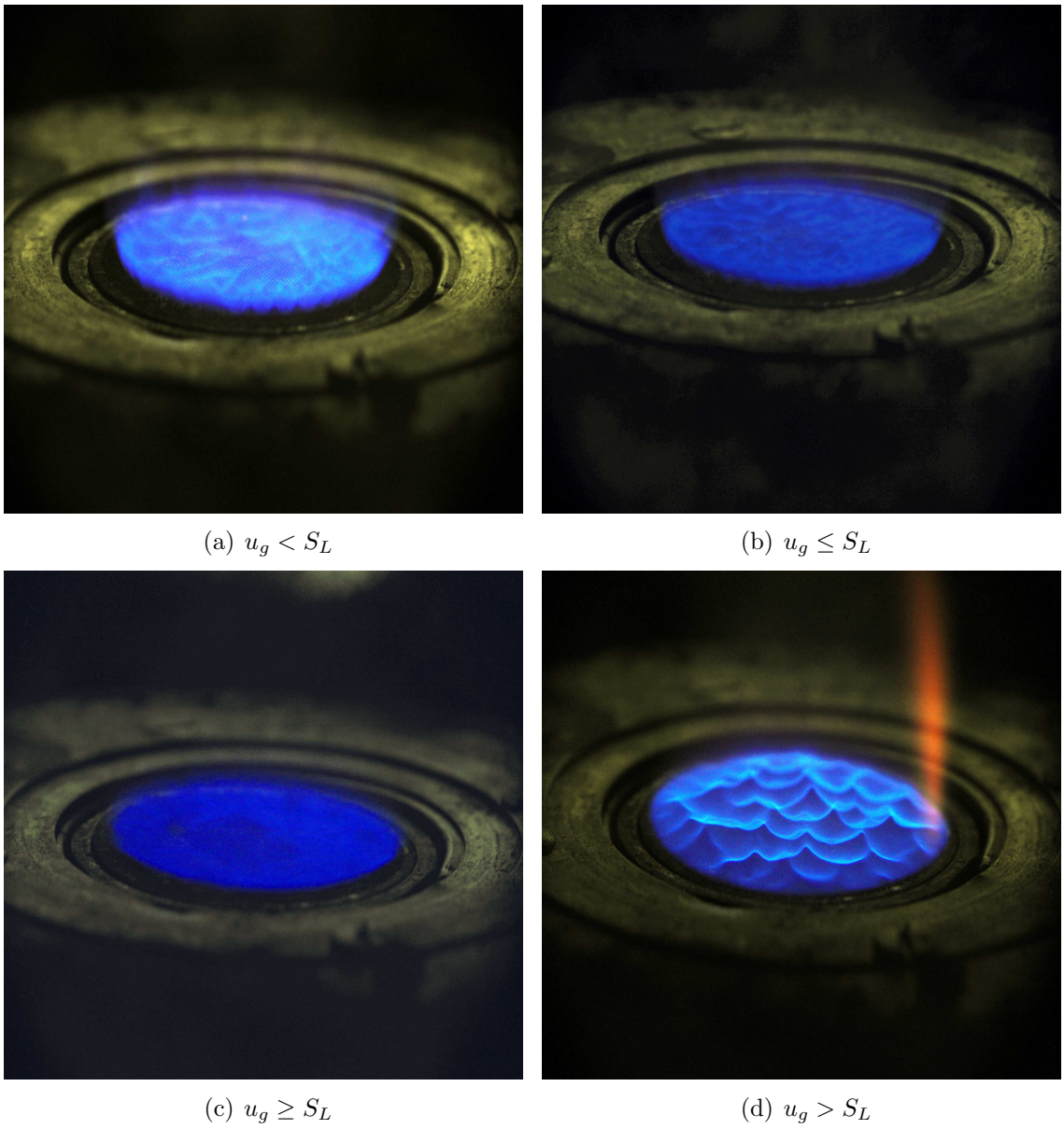

(a) $u_g < S_L$ (b) $u_g \leq S_L$

(c) $u_g \geq S_L$ (d) $u_g > S_L$

Figure 7.7: Stoichiometric premixed methane/air flame at 2 bar and $T_u = 298$ K under subadiabatic, close-to-adiabatic and superadiabatic states.

characteristics and (c) system geometry. Each of these variables can affect the instability of the system. Some attempts were made to change the system geometry by placing several glass tubes around the flame with an outer radius of 5 cm and different heights. Also, steel wool was placed around the burner head and inside the plenum chamber. Besides that, the equivalence ratio was varied for each pressure condition up to 5 bar. Despite these changes in the system variables, the flame instabilities consistently persisted for subadiabatic and close-to-adiabatic conditions. This consistency is an indication that while the thermo-acoustic instability could be responsible for the noise generated at some conditions, it is not likely to be the only phenomena responsible for the observed instabilities.

Cellular flames: premixed flames typically show cellular structures on the flame front. This phenomena can be caused by hydrodynamic (Landau-Darrieus) and thermo-diffusive mechanisms. Hydrodynamic instabilities are typically induced by changes in density as a result of thermal expansion of the burnt gas, normally associated with large scale flames. Thermo-diffusive instabilities can normally be quantified by the Lewis number ($Le = \alpha/D$), which is defined as the ratio of thermal diffusivity (α) to mass diffusivity (D). This dimensionless number should be less than unity for cellular flames to occur. Therefore, cellular flame instabilities are expected in fuel-rich flames of heavy hydrocarbons and fuel-lean flames of light fuels as hydrogen and methane [12]. However, the flame instabilities observed for our methane-air flames occur for all equivalence ratios between 0.8 and 1.4.

Heat balance/transport in the burner plate: the temperature magnitude and distribution on the burner plate can also play an important role in the flame stability. A typical measurement of S_L is performed, even under strong flame instabilities, in order to measure the temperature distribution on the burner plate. It can be seen in figure 7.8 that the temperatures measured for several gas velocities along the radius of the burner plate are extremely high for subadiabatic conditions. Temperatures around 100 °C are expected for adiabatic conditions (in this case, $v_g \approx 29$ cm/s) and below 150 °C for subadiabatic conditions. However, 200 °C is measured around adiabatic conditions and the temperatures reach values as high as 400 °C at subadiabatic conditions. In the worst case (stoichiometric flame measured at 5 bar) temperatures went up higher than 650 °C. These extreme temperatures also caused the burner plate to bend and the fabrication of a new one was necessary. For superadiabatic conditions, the temperatures were within the expected values (figure 7.8).

In situations where the temperature is above 200 °C, some chemical reactions can be initiated which compromises the reliability of the method. Konnov [13, 14] also expressed, in private communication, concerns about some peroxides formation on the burner plate for temperatures $>$ 200 °C. Therefore, it was concluded that the high temperatures, and possible chemical reactions associated with them, were the cause for the flame instabilities observed. From adiabatic to subadiabatic conditions the flame is moving closer to the burner plate causing higher heat losses to the burner plate when compared with the superadiabatic conditions. The flame instabilities get worse when pressure is increased due to the consequent increase in flame power. A goal to keep the temperature of the burner plate below 150 °C has been set in order to perform reliable measurements.

The electrical heating element, used to control the burner plate temperature, can only add heat to the burner plate. In subadiabatic situations it is automatically switched off to also allow heat transfer to the burner head cooling down the burner plate. This mechanism was not working properly and the thermal contact between the burner plate and burner head had to be optimized to improve the release of the surplus of heat in the burner plate. The following solutions were considered:

- Increase the thickness of the burner plate from 1 mm to 2 mm. This measure

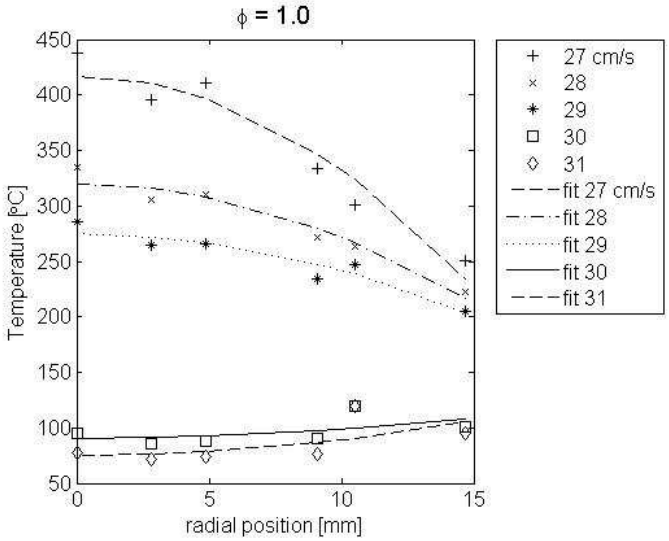

Figure 7.8: Temperature profile in the burner plate for a stoichiometric premixed methane/air flame at 2 bar and $\phi = 1.1$. Preliminary results showing unexpected high temperatures for subadiabatic conditions (i.e. $S_L \leq 29$ cm/s).

doubles the volume of the burner plate and increases the area of contact between the burner plate and the fresh unburnt gas mixture. Consequently, the heat flux released from the burner plate will improve, resulting in a lower average burner plate temperature.

- Replace the electrical heating element around the burner plate with a water channel as used in the burner originally designed for atmospheric pressure measurements. The obvious advantage related to the electrical heating element is that the water channel can cool down the burner plate when necessary.

- In the current design, a mechanical contact is used to conduct heat from burner plate to burner head. A conductive paste layer between the burner head and burner plate could improve the contact surface and therefore heat conduction between them.

Due to manufacturing limitations it turned out not possible to create a thicker burner plate while keeping a hole size of 0.3 mm. The water channels option could not be easily implemented in the current burner design due to the lack of space around the burner head. This solution also implied other burner and vessel design modification to guide the water channels to the burner head which could not be realized within the time frame of the present feasibility study. Therefore, it was chosen to apply a conductive paste layer between the burner head and the burner plate. The conductive paste used (Thermalcote from Thermalloy inc.) has a thermal conductivity of 0.377 W/m.K and can be used for temperatures up to 204 °C.

The performance of the conductive paste was verified by measuring the temperature profile in the burner plate at 5 bar. This pressure is considered to be the worst case where the temperature profile in the burner plate is expected to be the highest,

in the pressure range studied here, due to the increase in flame power. As can be seen in figure 7.9, the temperature profile for ϕ=1.1 shows a maximum value $\simeq$130 °C, which is considerably lower than the values measured before the application of the conductive paste.

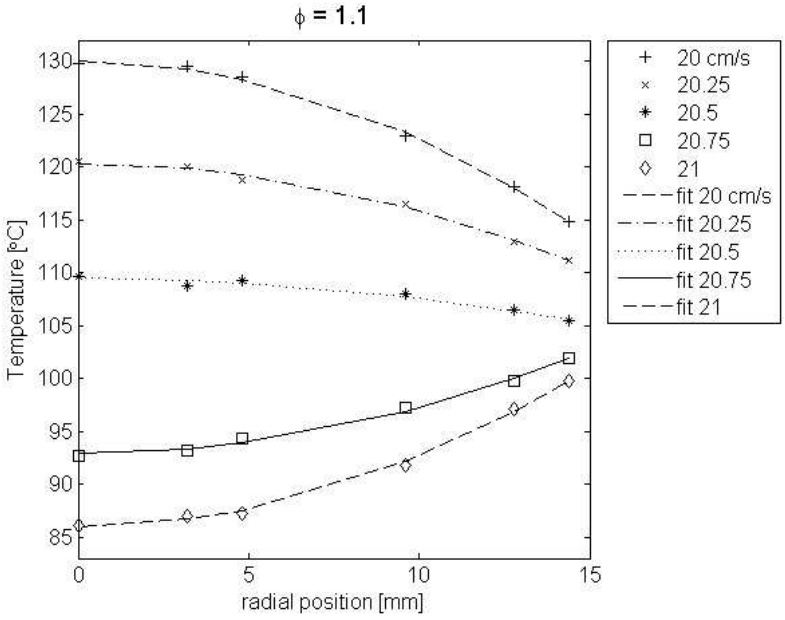

Figure 7.9: Temperature profile in the burner plate for a stoichiometric premixed methane/air flame at 5 bar and $\phi = 1.1$ after application of a conductive paste layer between the burner head and the burner plate.

7.3.2 Measurements of S_L at elevated pressures

Measurements of laminar burning velocities were performed at elevated pressures varying from 1.5 to 5 bar in steps of 0.5 bar. In this range of pressures burning velocities are measured for equivalence ratios varying from 0.8 to 1.4. The experimental results are summarized in figure 7.10 (the solid lines represent a third order polynomial fit as function of equivalence ratio for each pressure). Because the pressure inside the vessel is always slightly higher than atmospheric pressure, even when the chimney is taken off, no measurements at atmospheric pressure could be performed. Therefore, for purpose of comparison, the burning velocities for atmospheric pressure are taken from Slikker [1] since they were measured with the same burner (designed to work at high pressure) before integration with the pressure vessel.

The uncertainty in calculated values for ϕ is only influenced by the accuracy in the mass flow controllers (MFC's) and estimated around 1.2% at ϕ=1.0. For other equivalence ratios the uncertainty increases to 1.5%, due to the relative higher inaccuracy of the MFC's when producing smaller flows. The uncertainty in S_L is influenced by the accuracy in fuel/air mass flows and pressure control as well as temperature measurements [7, 9]. The main contribution to this uncertainty comes from the pressure

deviations. It was estimated to be largest at 1.5 bar, and decreasing when pressure is increased. Typically, four sets of measurements are performed to determine the laminar burning velocities and verify the repeatability. Standard deviations in S_L calculated from these measurements are within 3.2%.

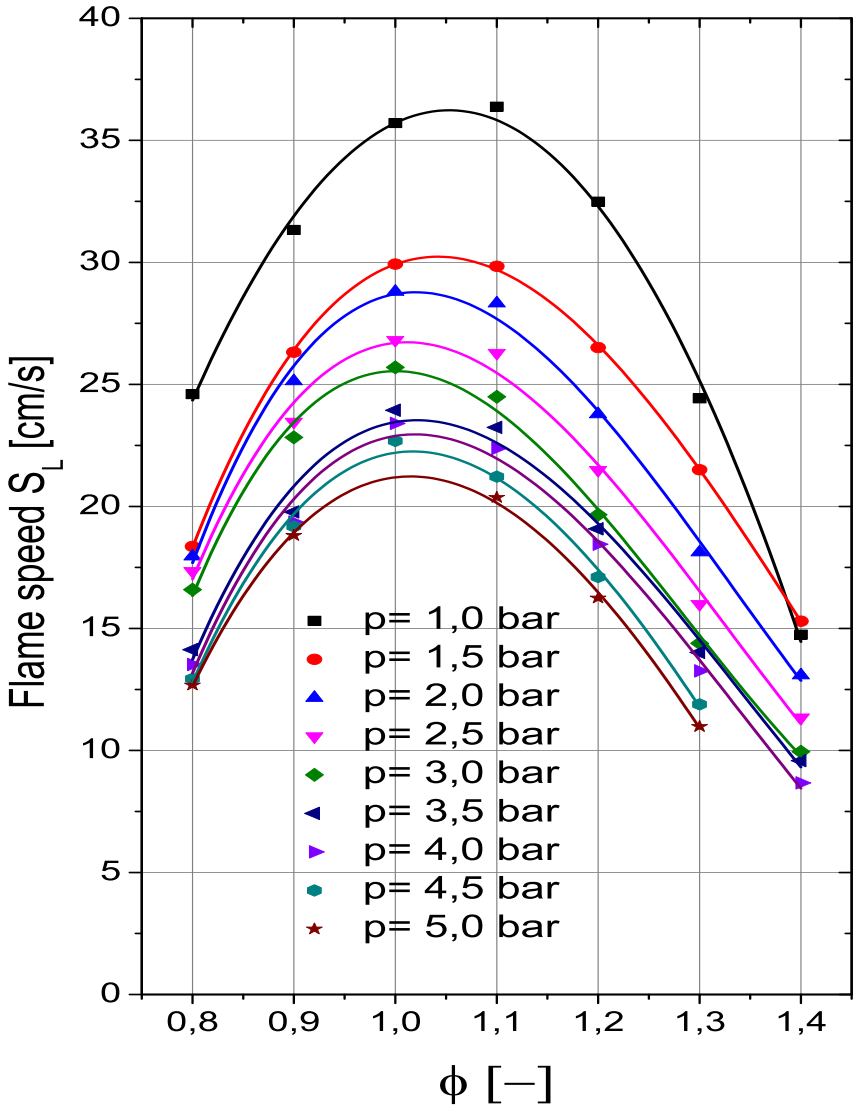

Figure 7.10: Results of adiabatic burning velocity measurements on premixed methane/air flames for pressure up to 5 bar. The equivalence ratio is varied between 0.8 and 1.4 and T_u=298 K. The results for atmospheric pressure are obtained from Slikker [1].

Despite the improvement achieved with the conductive paste, the temperature values for ϕ=1.0 at p=5.0 are still above 200 °C, and therefore, S_L is not measured at this condition. For other equivalence ratios and pressures, the flame power is lower and the large increase in burner plate temperature is only observed when the gas inlet velocity is substantially smaller than the burning velocity. Therefore, during the measurements, smaller velocity steps around the adiabatic burning velocity were taken in order to avoid the flame getting close to the burner plate at subadiabatic conditions.

It can also be seen in figure 7.10 that, for pressures higher than 3.0 bar, the values of S_L at fuel lean condition, especially at $\phi = 0.9$, are very close to each other and relatively far from the values at 3.0 bar. It is important to be mentioned that for this range of pressure ($3.5 \leq p \leq 5.0$ bar) an extra mass flow controller for air was installed to be able to supply the desired air flow. In principle, it is not expected that larger deviations will occur comparatively to the use of one MFC. The flow ratios between the two MFC's used in parallel were set proportional to their mutual maximum flow rates to keep deviations also proportional. The burning velocity for ϕ=1.4 at $p = 1.5$ bar ($S_L = 15.3 \pm 0.5$ cm/s) statistically coincides with the velocity at 1 bar measured by Slikker [1]. The values at 1 bar measured by Slikker and Bosschaart [7] using a burner designed for atmospheric measurements are higher, $S_L = 17.3 \pm 0.8$ cm/s and $S_L = 17.5 \pm 0.7$ cm/s, respectively. At equivalence ratio $\phi = 1.4$, measurements could not be performed for 4.5 and 5.0 bar. It was not possible to keep the vessel at these pressures due to the small flow of exhaust gases and the sealings used to make the environment leak tight. This situation suggests a lower limit in the value of S_L that the current setup can measure, which is $S_L \simeq 8.7$ cm/s. Consequently, the equivalence ratio range that can be measured will also be shorter for higher pressures as the values of S_L approach this lower limit.

The dependence of the adiabatic burning velocities on pressure is normally derived from the experimental data in the form of empirical correlations. The most common empirical correlation found in literature can be written as

$$S_L = S_0(\frac{p}{p_0})^{\beta}, \tag{7.1}$$

where S_0 is the burning velocity at atmospheric pressure p_0, p the actual pressure and β the pressure exponent, which can still depend on equivalence ratio. The correlations calculated in this work are valid for pressures varying from atmospheric to 5 bar and the results are shown in figure 7.11 together with the experimental data for all measured equivalence ratios except ϕ=1.4. A correlation is not calculated for ϕ=1.4 because at this equivalence ratio only measurements up to 4 bar are performed and the value measured at atmospheric measurement is not in correspondence with the expected trend (it should be slightly higher compared to elevated pressure results). The correlations in this figure show a good correspondence with the measured data. The scatter for all correlations is largest for p=1.5 bar where also the error in pressure is supposed to be largest.

Also the scatter in data around 3 and 3.5 bar is larger than for other pressures, for most of the correlations. This is the point where an extra air MFC was installed

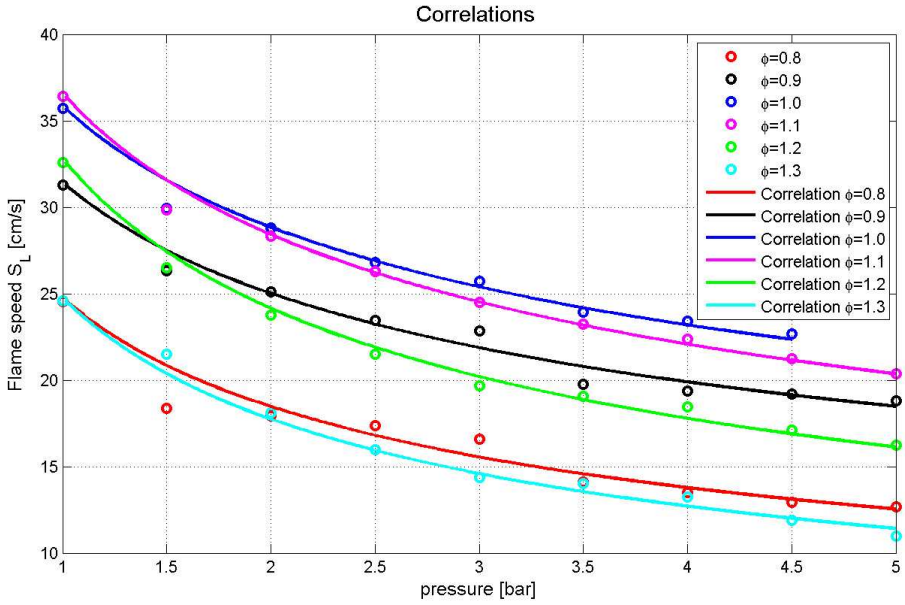

Figure 7.11: Correlations (lines) and experimental data (circles) of S_L as function of pressure at different equivalence ratios in the range of $0.8 \leq \phi \leq 1.3$.

to be able to make the higher air flows. Furthermore it can be concluded that mostly the scatter between correlation and data is less than 0.5 cm/s. A summary of the results from the derived correlations in this section is given in figure 7.12. From this figure it can be concluded that β is maximal for ϕ=1.0 and decreasing for lean and rich flames.

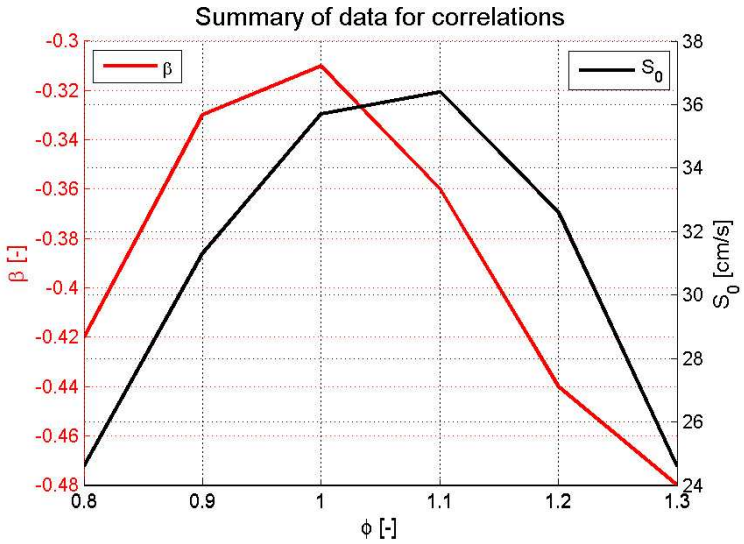

Figure 7.12: Summary of the values β and S_0 used for the derived correlations.

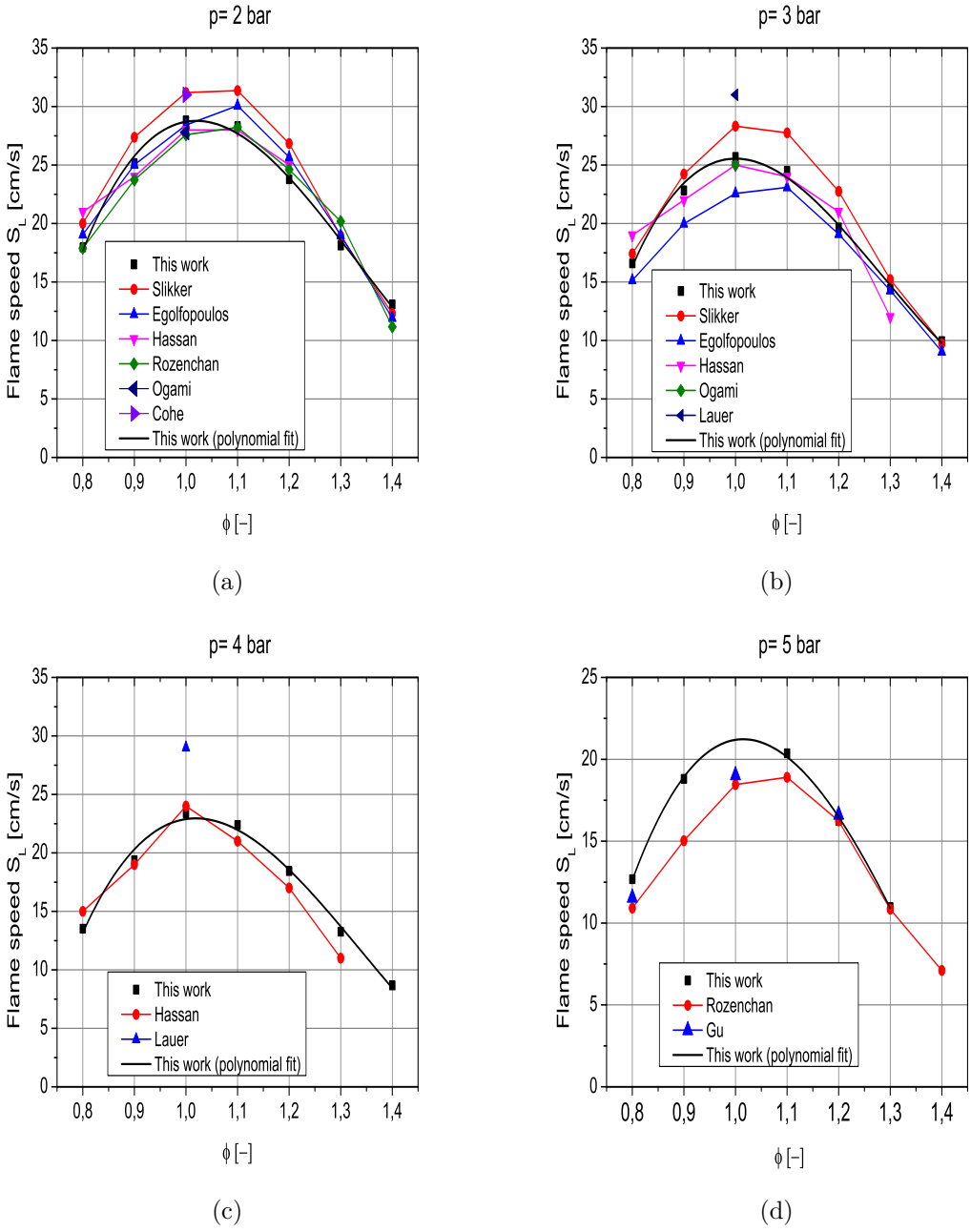

Figure 7.13: Results of measurements at elevated pressures compared with literature with $T_u = 298$ K.

7.3.3 Literature comparison

A comparison with data from literature is presented in figure 7.13. The results at 2 bar, shown in Figure 7.13(a), appear to be in good correspondence with Egolfopoulos et al. [2], Hassan et al. [5], Rozenchan et al. [15] and Ogami and Kobayashi [16]. Results from Slikker [1] and Cohe et al. [17] are somewhat higher. At 3 bar the results are in quite good agreement with Ogami and Kobayashi [16] in stoichiometric conditions and with Hassan et al. [5] in the range $0.9 \leq \phi \leq 1.4$ as shown in Figure

7.13(b)). Results from Slikker [1] and Lauer and Leuckel [18] are higher and Egolfopoulos' results are lower. The measurements of Slikker, shown here up to 3 bar, were performed using the heat flux burner designed for atmospheric pressure measurements which contains a burner plate with larger holes than the one designed for high pressure measurements. Slikker also reported measurements of burning velocities at atmospheric pressure performed in both burners. The values obtained with the burner designed for atmospheric pressure were significantly higher than most results from the literature as well as the values obtained with the burner designed for high pressure measurements, which is the one used in the present work.

For the results at 4 bar, as shown in figure 7.13(c), it can be concluded that a good correspondence is reached with Hassan et al. [5] for ϕ is 0.9 and 1.0. For rich flames the results are slightly lower and for ϕ=0.8 somewhat higher compared to Hassan et al. [5] Stoichiometric results from Lauer and Leuckel [18] are much higher. The results at 5 bar show good agreement with Rozenchan et al. [15] for rich flames (ϕ=1.2 and 1.3) and with Gu et al. [19] for rich and lean flames (ϕ=0.8) as becomes clear from Figure 7.13(d)). In close-to-stoichiometric conditions at 5 bar, the results are higher when compared with the work of Gu et al. [19] and Rozenchan et al. [15]. In general, better agreement has been observed with the work of Hassan et al. [5] for pressures up to 4 bar which does not report data at 5 bar. The stoichiometric flames at 2 and 3 bar show values of S_L close to the results of Ogami and Kobayashi [16]. Their measurements were also obtained with an experimental method where no correction for flame stretch is necessary (Nozzle type burner).

In order to assess the measurements performed in this work using the heat flux method for stoichiometric conditions, a comparison with other data from the literature is done [1, 2, 4, 5, 13, 15–20]. The measured burning velocity and the calculated correlation as function of pressure are shown together with both numerical and experimental data up to 5 bar in figure 7.14.

From this figure a lot of scatter appears between results from different researchers. Compared to this research, results from Lauer and Leuckel [18] are much higher. Also data from Cohe et al. [17] and Slikker are comparatively high. Egolfopoulos et al. [2], Kobayashi et al. [4] and the numerical results from the GRI 3.0 mechanism [20] are crossing the results from this research. A good correspondence is observed comparing with the data from Hassan et al. [5]., Ogami and Kobayashi [16] and the trend from the Konnov 0.5 mechanism [13]. For these cases, the difference in burning velocities between experiment and theory is almost constant for pressures up to 5 bar (< 1 cm/s).

Empirical correlations (in the form of Eq. 7.1) were also calculated for stoichiometric flames by Slikker [1] and Stone et al. [21] and at ϕ= 0.8, 1.0 and 1.2 by Gu et al. [19]. These correlations are valid for pressures between 0.2 and 3 bar (Slikker), from 1 to 10 bar (Gu et al. [19]) and from 0.5 to 10.4 bar (Stone et al. [21]). The correlation from this work is valid for pressures from atmospheric to 5 bar. In order to compare these correlations with the present work, the coefficient β is determined for the other literature sources. The result is plotted for lean (ϕ=0.8), stoichiometric and rich flames (ϕ=1.2) in figure 7.15, where the circles represent the measured adiabatic burning velocities.

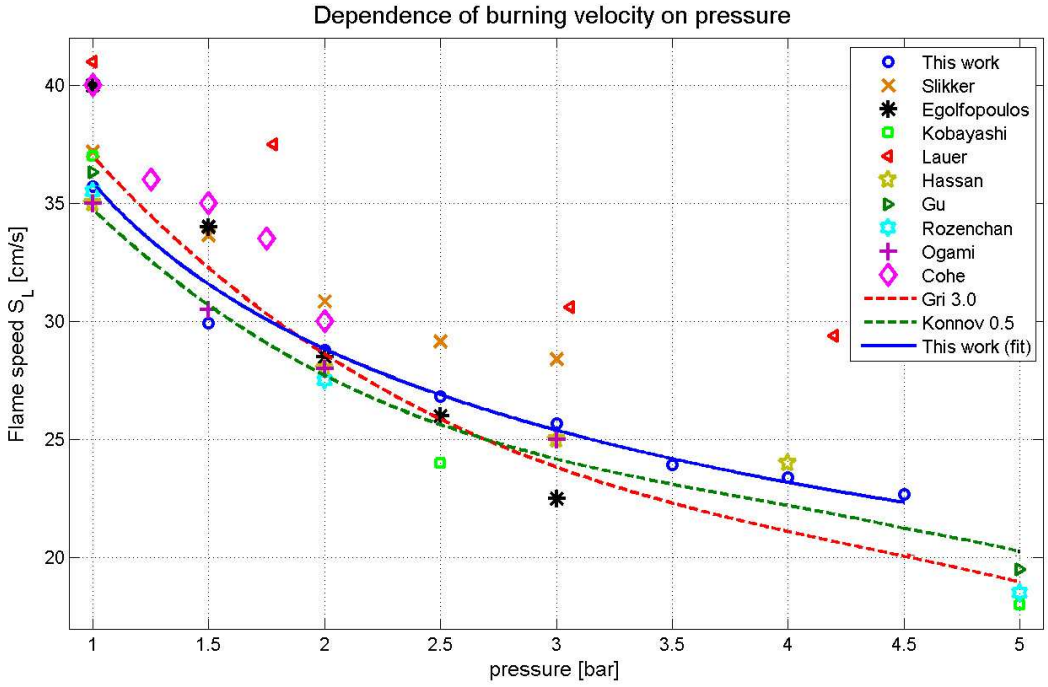

Figure 7.14: Comparison of numerical and experimental data of burning velocity as function of pressure for stoichiometric flames up to 5 bar (T_u=298 K).

The values of β determined from this research are shown in Table 7.1 together with results from other research. From this table and the figure 7.15, good agreement with the results from Stone et al. [21] for stoichiometric flames and from Gu et al. [19] for rich flames can be seen (there are overlaps of curves in figure 7.15). The values of β determined for Gu et al. [19] for stoichiometric and lean flames are slightly higher and therefore the correlations show a slightly weaker trend.

Table 7.1: Overview of values for the pressure exponent β measured in literature for lean (ϕ=0.8), stoichiometric and rich flames (ϕ=1.2)

References	ϕ=0.8	ϕ=1.0	ϕ=1.2
This work	-0.42	-0.31	-0.44
Slikker [1]	n.a.	-0.26	n.a.
Stone et al. [21]	n.a.	-0.314	n.a.
Gu et al. [19]	-0.504	-0.374	-0.438

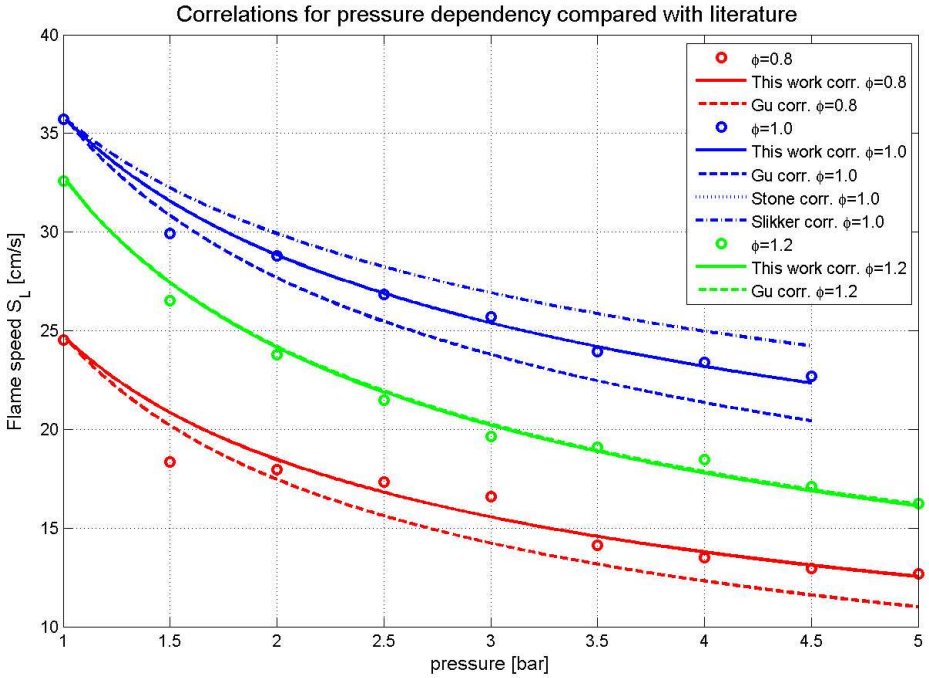

Figure 7.15: Correlations (lines) and experimental data (circles) of S_L as function of pressure for lean, stoichiometric and rich flames (T_u=298 K). There are overlaps of curves between this and Stone's work at ϕ=1.0 and this and Gu's work at ϕ=1.2.

7.4 Conclusions

A feasibility study to extend the heat flux burner method to elevated pressures was accomplished by integrating the heat flux burner setup into a high pressure vessel. The latter was used with a coflow burner in earlier chapters.

Preliminary pressurization tests showed strong flame instabilities in subadiabatic and close-to-adiabatic conditions. The relation of the instabilities with some known physical phenomena was assessed and the root cause of the instabilities was attributed to the high temperatures in the burner plate. In close-to-adiabatic and subadiabatic conditions the flame is closer to the burner plate than in superadiabatic conditions, comparatively increasing the heat release rate to the burner plate. The worst case was a stoichiometric flame at 5 bar where temperatures reached values over 650°C, damaging the burner plate. A conductive paste improved the heat transfer from the burner plate to the burner head reducing the temperature to acceptable values below 150°C. Measurements of S_L as function of ϕ and pressure could be performed except for: (a) a stoichiometric flame at 5 bar, where temperatures were still above 200°C and (b) ϕ =1.4 at 4.5 and 5.0 bar, where exhaust gases flow was not large enough to reach those pressures with the current pressurization system. Therefore, for higher pressure measurement with the current setup, design modifications must be implemented to improve cooling of the burner plate and vessel pressurization.

Four sets of measurements were performed at each flame condition and calculated standard deviations in S_L were lower than 3.2%. Comparison with data from literature showed good agreement with the work of Hassan et al. [5] for pressures up to 4 bar over the entire range of equivalence ratios. The rich flames at 5 bar show best correspondence with the work of Rozenchan et al. [15], however, the lean flames at 5 bar are somewhat faster. Stoichiometric burning velocities show better agreement with experimental data from Hassan et al. [5] and Ogami and Kobayashi [16] as well as with numerical predictions using the reaction mechanism of Konnov [13]. Empirical correlations of burning velocity and pressure were derived for all measured equivalence ratios with a scatter less than 0.5 cm/s. The empirical correlation calculated in this work for pressures up to 5 bar showed good agreement with the work of Stone et al. [21] and Gu et al. [19] for ϕ=1.0 and 1.2 respectively.

7.5 Recommendations

Based on the preceding results and findings, the following recommendations can be made:

Burner plate temperature: in order to improve cooling of the burner plate, it is recommended to replace the electrical heating element with a water channel around the burner plate. This will imply in the current burner and vessel a design modification to guide the water channels to the burner head.

Vessel temperature: due to the increase of flame power with pressure, the temperature inside the vessel is reaching values close to the limit of the sealing materials of the setup. The air diffuser designed to control the temperature inside the vessel caused disturbance to the flame due to a combined effect of the relatively high velocity of the jets with the small size of the vessel. The design can be adapted to deliver an air flow with lower velocity by increasing the diameter of the holes. An increase in the size of the vessel will also contribute to reduce the disturbances caused by the air diffuser while keeping the temperature inside the vessel comparatively lower due to the lager volume.

Vessel pressurization: the pressure in the vessel is measured by a manometer and manually adjusted to the required pressure via a needle valve on top of the chimney. It is suggested to install a back pressure regulator in order to reduce the time adjusting the pressure and improve precision. Besides the use for cooling, the extra air (or nitrogen) provided by the diffuser will help the vessel pressurization in case of low exhaust gases flow, as was experienced for measurements at $\phi = 1.4$ and $p \geq 4.5$ bar.

Bibliography

[1] W.J. Slikker. Extension of the heat flux method to elevated pressures. Technical report, Eindhoven University of Technology, 2008.

[2] F.N. Egolfopoulos, P. Cho, and C.K. Law. Laminar flame speeds of methane-air mixtures under reduced and elevated pressures. *Combustion and Flame*, 76: 375–391, 1989.

[3] O. Park, P.S. Veloo, N. Liu, and F.N. Egolfopoulos. Combustion characteristics of alternative gaseous fuels. *Proceedings of the Combustion Institute*, 33:887–894, 2011.

[4] H. Kobayashi, T. Nakashima, T. Tamura, K. Maruta, and T. Niioka. Turbulence measurements and observations of turbulent premixed flames at elevated pressures up to 3.0 MPa. *Combustion and Flame*, 108:104–117, 1997.

[5] M.I. Hassan, K.T. Aung, and G.M. Faeth. Measured and predicted properties of laminar premixed methane/air flames at various pressures. *Combustion and Flame*, 115:539, 1998.

[6] L.P.H. de Goey, A. van Maaren, and R.M. Quax. Stabilization of adiabatic premixed laminar flames on a flat-flame burner. *Combustion Science and Technology*, 92:201–207, 1993.

[7] K.J. Bosschaart and L.P.H de Goey. Detailed analysis of the heat-flux method for measuring burning velocities. *Combustion and Flame.*, 132:170–180, 2003.

[8] L.P.H. de Goey, L.M.T. Somers, W.M.M.L. Bosch, and R.M.M. Mallens. Modeling of the small scale structure of flat burner-stabilized flames. *Combustion Science and Technology*, 104:387–400, 1995.

[9] R.T.E. Hermanns, A.A. Konnov, R.J.M. Bastiaans, L.P.H. de Goey, K. Lucka, and H. Köhne. Effects of temperature and composition on the laminar burning velocity of CH_4 + H_2 + O_2 + N_2 flames. *Fuel*, 89:114–121, 2010.

[10] A. van Maaren. *One-step chemical reaction parameters for premixed laminar flames*. PhD thesis, Eindhoven University of Technology, 1994.

[11] V. Ratna Kishore. *Experimental and computational investigations on open laminar flames of multi-component gaseous fuel mixtures*. PhD thesis, Indian Institute of Technology Delhi, 1994.

[12] A. A. Konnov and I. V. Dyakov. Measurements of propagation speeds in adiabatic cellular premixed flames of CH_4 + O_2 + CO_2. *Experimental Thermal Fluids and Science*, 29:901–907, 2005.

[13] A. A. Konnov. Development and validation of a detailed reaction mechanism for the combustion of small hydrocarbons. *28th Symposium (Int.) on Combustion*, page 317, 2000.

[14] A.A. Konnov, I.V. Dyakov, and J. De Ruyck. Probe sampling measurements and modeling of Nitric Oxide formation in methane-air flames. *Combustion Science and Technology*, 169:127–153, 2001.

[15] C. Rozenchan, D.L. Zhu, C.K. Law, and S.D. Tse. Outward propagation, burning velocities, and chemical effects of methane flames up to 60 atm. *Proceedings of the Combustion Institute*, 29:1461–1469, 2002.

[16] Y. Ogami and H. Kobayashi. Laminar burning velocity of stoichiometric CH_4/air premixed flames at high-pressure and high-temperature. *JSME International Journal Series B*, 48(3):603–609, 2005.

[17] C. Cohé, D.F. Kurtulus, C. Chauveau, and I. Gökalp. Investigation of laminar lean premixed methane-air flames at high pressures. *Proceedings of the European Combustion Meeting*, 2007.

[18] G. Lauer and W. Leuckel. Laminar burning velocity of coal gases and methane at elevated pressures and temperatures: Experiments and modeling. *Archivum Combustionis*, 15(1-2):7–23, 1995.

[19] X.J. Gu, M.Z. Haq, M. Lawes, and R. Woolley. Laminar burning velocity and markstein lengths of methane-air mixtures. *Combustion and Flame*, 121:41–58, 2000.

[20] G.P. Smith, D.M. Golden, M. Frenklach, N.W. Moriarty, B. Eiteneer, M. Goldenberg, C.T. Bowman, R.K. Hanson, S. Song, W.C. Gardiner Jr, V.V. Lissianski, and Z. Qin. *http://www.me.berkeley.edu/gri_mech/version30/text30.html*, 1999.

[21] R. Stone, A. Clarke, and P. Beckwith. Correlations for the laminar burning velocity of methane/diluent/air mixtures obtained in free-fall experiments. *Combustion and Flame*, 114:546–555, 1998.

CHAPTER 8

Conclusions and recommendations

A High Pressure Vessel and Burner (HPVB) setup was constructed, capable to burn gaseous and vaporized liquid fuels in laminar coflow diffusion and partially premixed flames. The evaporation concept that is used to vaporize the liquid fuels is the Controlled Evaporator Mixer (CEM, Bronkhorst) which can deliver reproducible and accurate stable vapor flow. The setup can be operated at pressures up to 3.0 MPa and offer ample optical accessibility to apply laser diagnostic techniques through four optical ports. An additional syringe pump system was integrated to the fuel line allowing these coflow gaseous and vaporized liquid flames to be doped with small amounts of liquid compounds at atmospheric pressure. To the knowledge of the author, there is no report of an existing experimental setup with similar characteristics and capabilities.

The major observations during the operation and measurements carried out with the HPVB setup are summarized below along with recommendations.

1. Flames of gaseous fuels have shown very good stability, with flame height standard deviation (σ) over time of less than 1% in most of the conditions investigated at atmospheric pressure. Measurements of spatially resolved soot volume fractions using the line-of-sight-attenuation (LOSA) technique were validated with data from Smooke and co-workers in ethylene diffusion flames. Overall a good agreement was observed, both in peak values and location of maxima in soot volume fractions.

2. The flame stability of vaporized liquid fuels (n-heptane and blends with oxygenated fuels) at atmospheric pressure showed strong dependence on fuel vapor flow, coflow air flow rates and the heated ring temperature. The coflow rates resulting in optimal stability varied between 20 and 25 L/min (0.43 - 0.54 g/s). Partially premixed flames are more stable if the system temperature is around the liquid fuel boiling point, while for diffusion flames higher temperatures show better stability. Stable laminar n-heptane flame at atmospheric pressure can be created for a large set of flow conditions as presented in table 2.3 of chapter

2. Blends of n-heptane with oxygenated fuels were found to be very unstable and the blend with cyclohexanone damaged the ball valve in the fuel line, due to the chemical nature of this fuel. It is recommended for the studies with the oxygenated fuels to use the doped flame approach, in which only a small amount of these fuels is added to the fuel line after the evaporator.

3. Methane-air diffusion flames initially became asymmetric for pressures higher than 0.6 MPa. This anomaly was attributed to formation of a water droplet at the tip of the aluminium fuel tube. This problem was solved by using a fuel tube with a lower thermal conductivity material (stainless steel) which kept the fuel tip relatively hotter, avoiding the water droplet formation. Methane-air partially premixed flames did not show asymmetry and were stable up to 2.5 MPa. Flame instabilities of vaporized liquid fuels dramatically increased with pressure and no long term stability was observed for pressures higher than 0.3 MPa for the investigated n-heptane flames.

4. Design modifications were necessary to improve flame stability. An orifice, one-way-valve and a buffer placed in the fuel line appeared to be successful in damping the strong flame oscillations that lead to flame blow off. The chimney design was also modified to increase the system (vessel + chimney) volume and include a water trap channel. The increase in the system volume also improved the overall flame stability.

5. Water condensation on the optical windows and vessel was largely avoided using high coflow air. However, it was observed that condensation still occurs on the lower part of the chimney's wall. In order to verify to which extent water condensation on this lower part of the chimney was affecting the flame stability, it is recommended to build a water cooling system around the chimney to induce water condensation on the upper part of the chimney's wall far from the flame and into the water trap channel. This cooling system would also serve to evaluate the effect of the flue gas temperature inside the vessel on the flame stability.

6. In the HPVB setup the pressure in the vessel can be regulated by a back pressure regulator. However, diffusion flames have shown high sensitivity to the pressure changes in the vessel when the pressure regulator was adjusting to the desired setpoint. Manual adjustment of the pressure was necessary to prevent flames to quench or blow off. This behavior was not observed for the partially premixed flames: these were comparatively much less sensitive to pressure changes and the pressure regulator could be used. It is recommended to change the parameters in the PID controller of the back pressure regulator to slow down the adjustment to the setpoint, avoiding sudden changes in pressure.

7. Considering the experimental setup developed here to study laminar flames at elevated pressures, there are advantages and limitations in applying the LII (Laser Induced Incandescence) technique for soot formation investigations when compared to the LOSA technique. The LII technique, after proper calibration, can provide instantaneous 2D maps of soot volume fraction distribution in flames with very low soot concentration. The application of LII in this setup is specially recommended if measurements in a large range of flame conditions (different flow

rates, type of fuels, etc.) and in low sooting flames are necessary. In this aspect, the LOSA technique is a comparatively slower measurement process due to the necessary laser scans over the flame width and height, and additionally, if the measurement resolution needs to be improved by taking smaller spatial steps between the laser scans. On the other hand, at higher soot concentrations, signal trapping significantly affects the LII signal as discussed in chapter 4 and references therein. Therefore, for measurements of soot volume fraction in flames at elevated pressure, the application of the LOSA technique is recommended since the signal (attenuation) to noise ratio only improves when measuring higher soot concentrations.

8. The LOSA measurements in this work indicate that the maximum soot volume fraction increases as $f_{v_{max}} \propto P^{2.46}$ over the pressure range from 0.6 to 1.0 MPa. This trend agrees closely with the work of Thomson [1] for pressures between 0.5 and 1.0 MPa.

9. A combination of LIF (Laser Induced Fluorescence) and LII using both 266 nm and 1064 nm as excitation wavelengths were applied to measure qualitative profiles of OH, PAH and soot, as well as quantitative soot volume fractions in vaporized liquid fuels flames (n-heptane and n-decane). The results illustrate that:

   (a) this technique can provide unambiguous spatial identification of PAH and soot in laminar flames;

   (b) the maximum PAH LIF signal is a good predictor of $f_{v_{max}}$ from LII;

   (c) excitation at 266 nm with delayed detection results in a linear correlation with soot volume fraction from LII using prompt detection and 1064 nm excitation;

   (d) the influence of any additional photo-chemical processes using high laser power at 266 nm and the influence of particle size for the delayed gate time, appear not significant for the flame conditions studied here;

   (e) the delayed and prompt measurements of LII signals spatially match, suggesting good synchronization between the different optical setups and a good flame repeatability of the HPVB setup.

10. A laminar CH_4/N_2-air co-flow flame has been doped with two dopants, benzene and toluene, each at three different concentrations. No problems were found during the operation of the injection system and the flames showed very good stability over all conditions studied. Qualitative profiles of Polycyclic Aromatic Hydrocarbons and OH radical have been measured to provide experimental data for investigation (done by others) of the capability of the flamelet-generated manifold (FGM) approach to numerically model multidimensional, laminar, non-premixed flames with the inclusion of PAH chemistry. Results showed that the model is able to capture the major characteristics of PAH formation.

11. The feasibility of using the heat flux method in a high pressure environment was investigated by integrating the heat flux burner in the high pressure vessel of the

HPVB setup. Measurements of burning velocities were carried out in premixed methane-air flames at pressures up to 0.5 MPa. Preliminary high pressure tests showed strong flame instabilities in subadiabatic and close-to-adiabatic conditions. The flame instabilities were related to the high temperature in the burner plate. A conductive paste improved the heat transfer from the burner plate to the burner head reducing the temperature to acceptable values, except for a stoichiometric flame at 0.5 MPa. Due to pressurization problems burning velocities for ϕ =1.4 at 0.45 and 0.50 MPa could not be measured. In order to solve these problems it is recommended to:

(a) replace the electrical heating element by a water channel around the burner plate;

(b) adapt the design of the current diffuser to deliver an air flow with lower velocity, by increasing the diameter of the holes. Besides the use for cooling, the extra air (or nitrogen) provided by the diffuser will help the vessel pressurization;

(c) install a back pressure regulator in order to reduce the time required for adjusting the pressure and to improve precision.

Overall, a new and innovative experimental setup has been added to enrich the spectrum of experimental research on future fuels and engines, carried out at the Combustion Technology group at Eindhoven University of Technology.

Bibliography

[1] Kevin A. Thomson. *Soot Formation in Annular Non-premixed Laminar Flames of Methane-Air at Pressures of 0.1 to 4.0 MPa.* Phd thesis, University of Waterloo, 2004.

Appendix: Machining Drawings

This appendix contains the machining drawings of the following parts of the HPVB setup:

- High pressure vessel
- High pressure burner
- Fuel tube with interchangeable nozzle
- Chimney

High pressure vessel

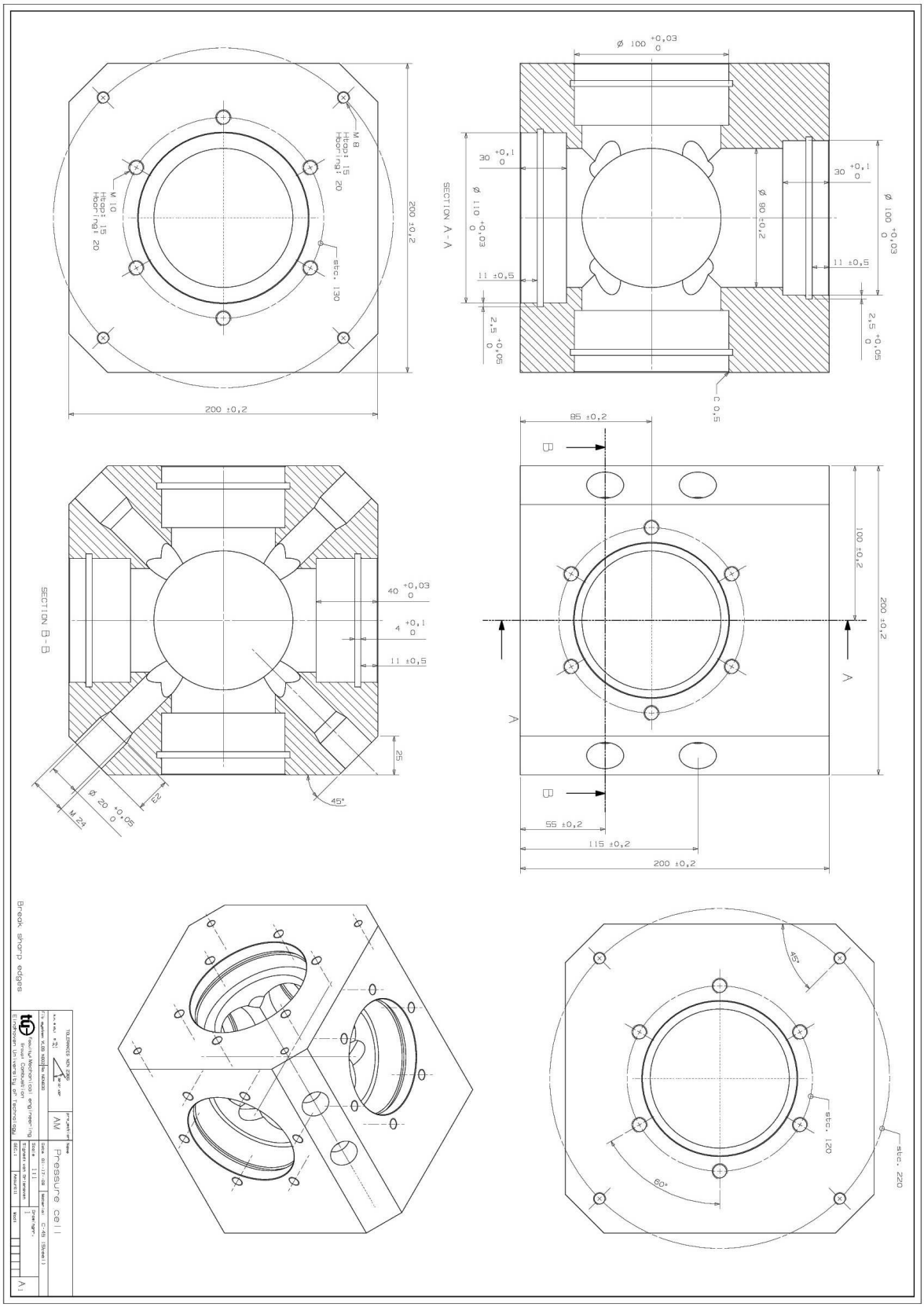

High pressure burner

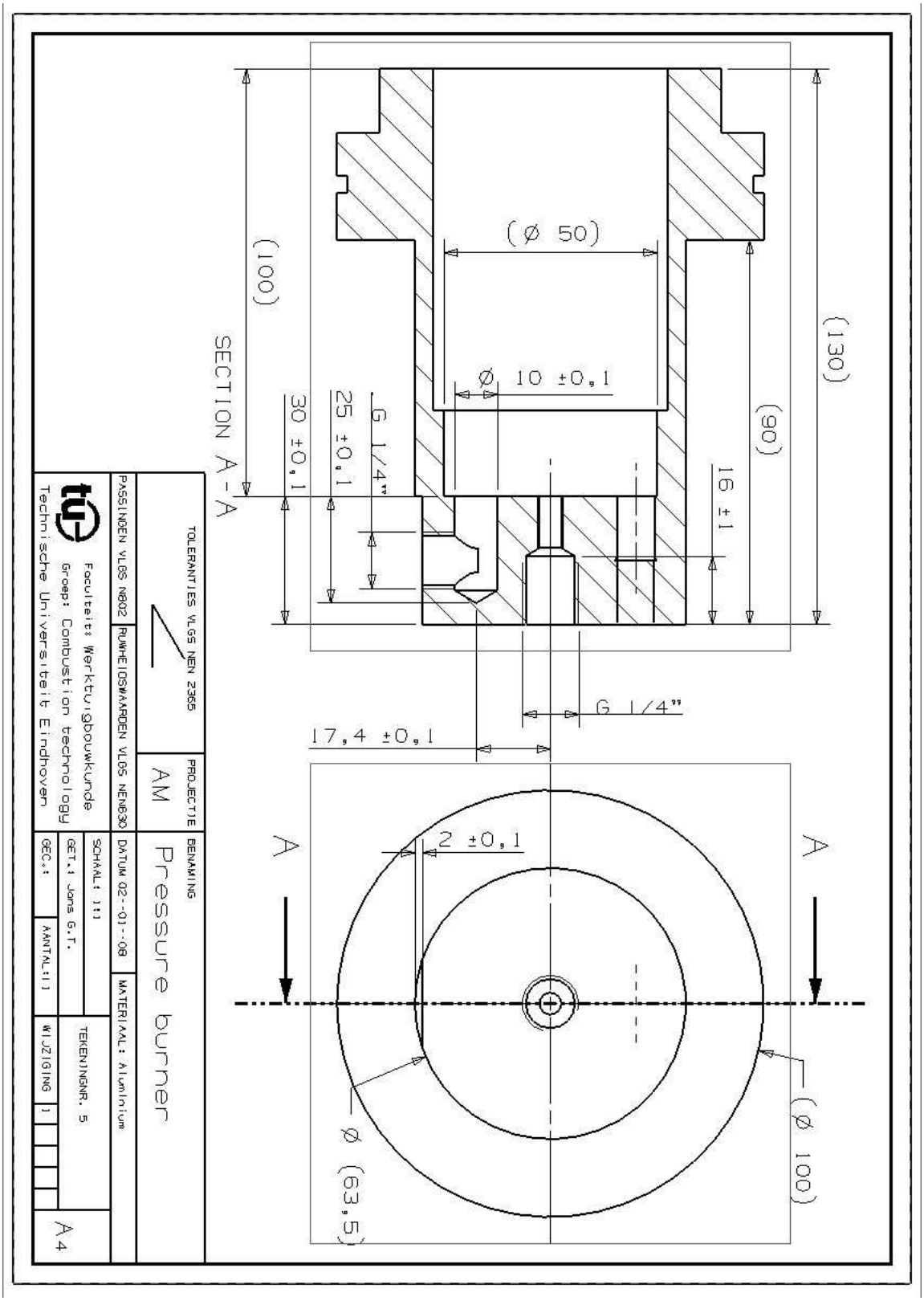

Fuel tube with interchangeable nozzle

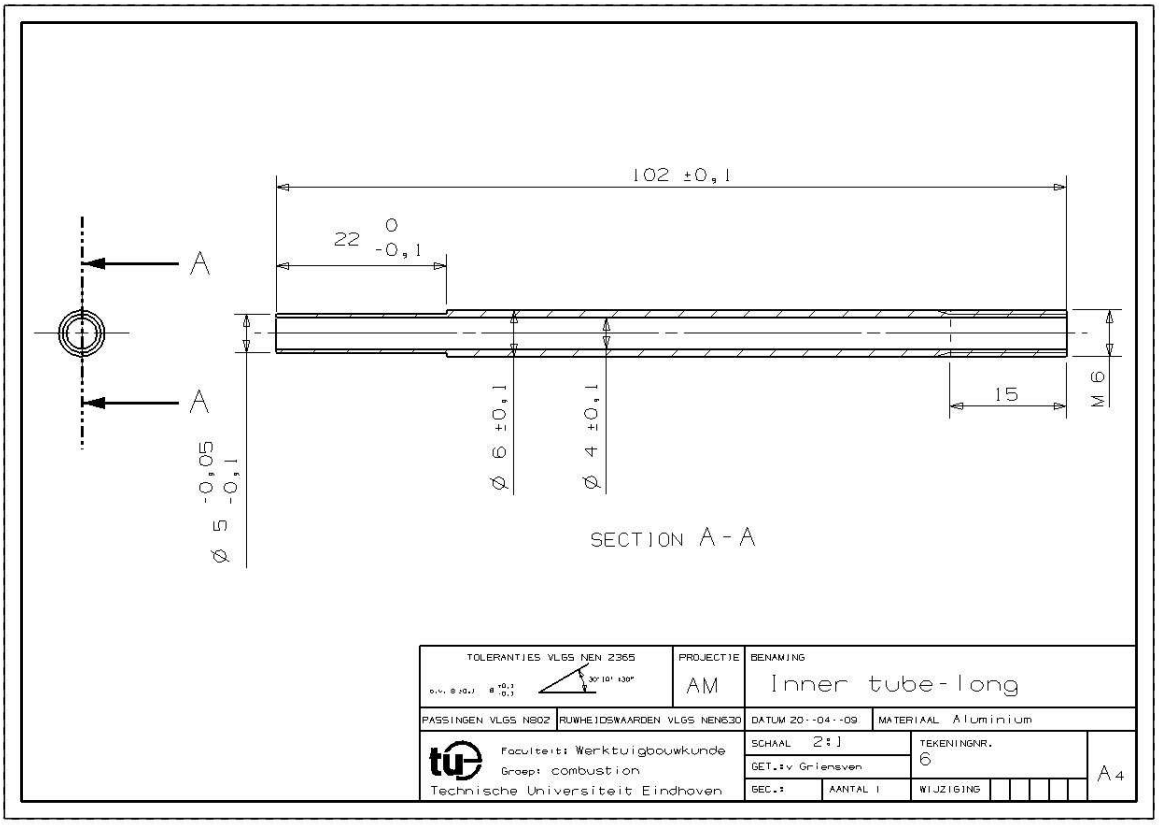

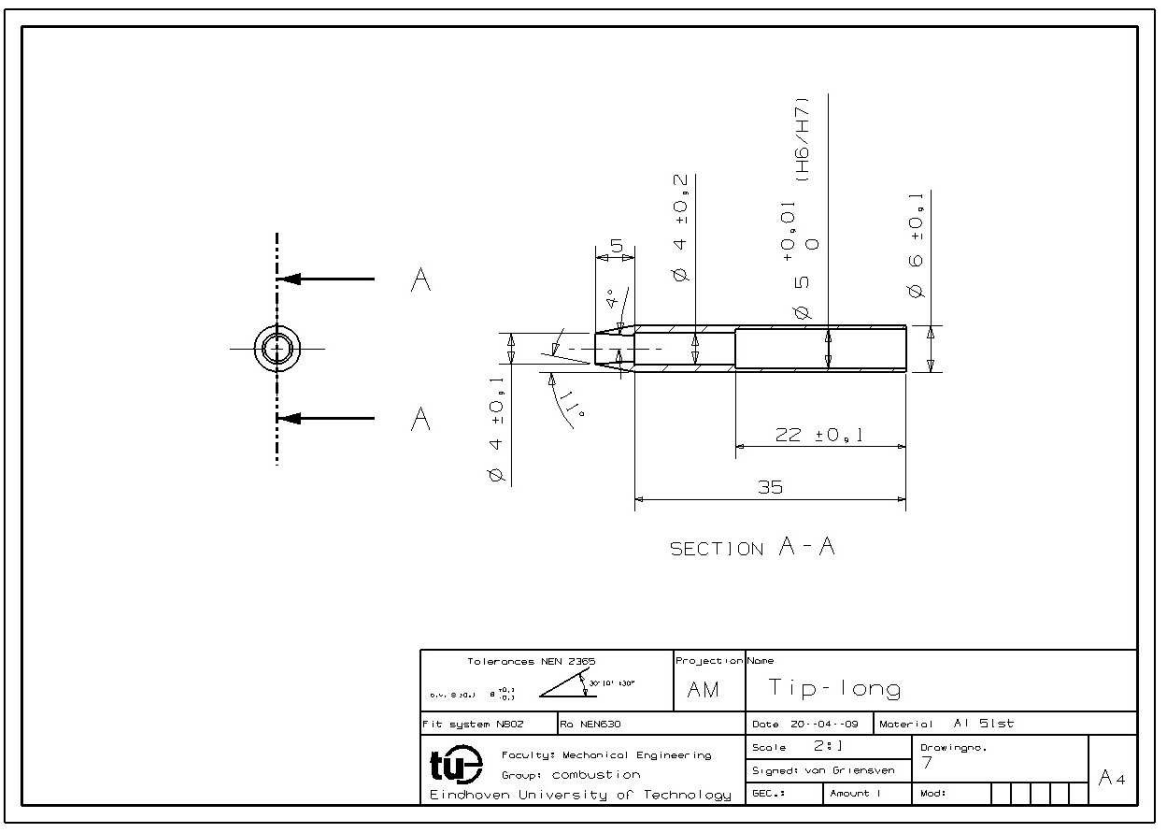

Chimney

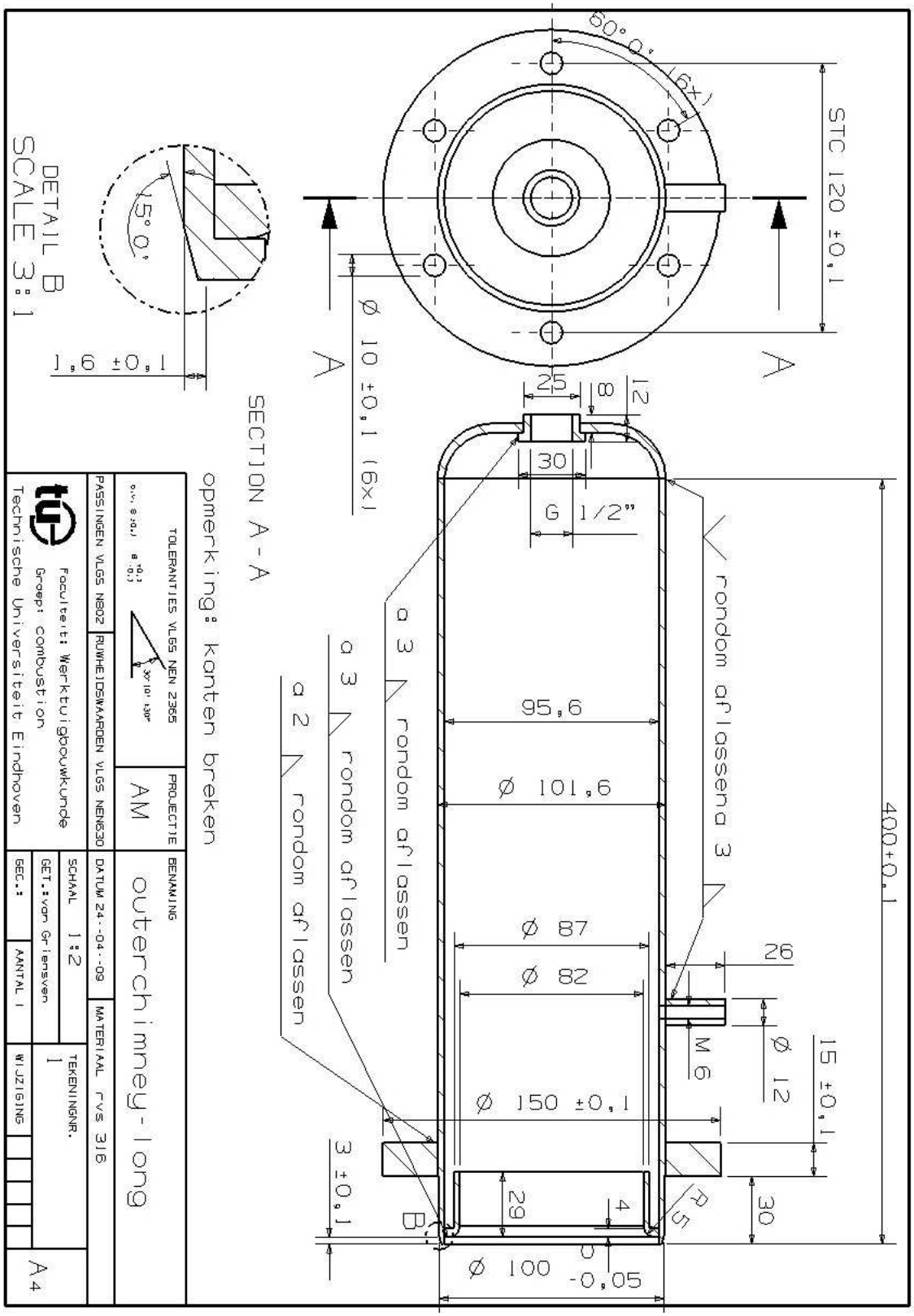
STC 120 ±0,1
60° 0' (6x)
Ø 10 ±0,1 (6x)
25
8
12
30
G 1/2"
400±0,1
random aflassen a 3
95,6
Ø 101,6
Ø 87
Ø 82
26
M 6
Ø 12
15 ±0,1
Ø 150 ±0,1
3 ±0,1
29
4
R 5
30
Ø 100 -0,05
SECTION A-A
DETAIL B
SCALE 3:1
15° 0'
1,6 ±0,1
opmerking: kanten breken
TOLERANTIES VLGS NEN 2365
PROJECTIE
BENAMING
AM
outerchimney-long
PASSINGEN VLGS N802
RUWHEIDSWAARDEN VLGS NEN630
DATUM 24-04-09
MATERIAAL rvs 316
SCHAAL 1:2
TEKENINGNR. 1
GET.: van Griensven
SEC.:
AANTAL 1
WIJZIGING
A4
Faculteit: Werktuigbouwkunde
Groep: combustion
Technische Universiteit Eindhoven

Curriculum Vitae

Marcelo Henrique de Andrade Oliveira was born in Recife, state of Pernambuco, Brazil on August 15^{th} 1975. After finishing scientific pre-university education in 1994, he started his study of Chemical Engineering at the Federal University of Pernambuco (UPFE) in Brazil. He worked on two industrial internships: from 1999 to 2000 as a quality control supervisor at a thermoplastic polymer (PVC - Polyvinyl chloride) manufacturer and from 2000 to 2001 as an engineer for production processing and financial analysis at a leading manufacturer of specialty polyester films (Terphane Ltda). After graduating in 2001, he completed his Master of Science in Chemical Engineering in 2004 studying the adsorbed natural gas (ANG) technology, an alternative technology to compressed natural gas (CNG) and liquefied natural gas (LNG) for storage of natural gas, especially for vehicular applications. Later that year, he started working, at the same University, as a Chemical Engineer Researcher on a project for the Brazilian oil company Petrobras to develop a new technology to treat waste water from oil refineries and offshore platforms using natural gas combustion. During this project, he was involved in building and starting up a pilot plant in cooperation with the École Polytechnique de Montreal (Canada) and private companies in Brazil, as well as in CFD (Computational Fluid Dynamics) simulations. In 2007, he moved to the Netherlands to start his PhD research on Combustion Technology at the Eindhoven University of Technology (TU/e). The research topic is to develop an experimental setup for studies of the combustion behavior of alternative automotive fuels at high pressure, applying laser diagnostics.

Acknowledgements

It is with enormous gratitude that I acknowledge the intellectual, emotional and financial support of all the people and institutions involved in my PhD project. I owe my deepest gratitude to my supervisors Philip de Goey and Carlo Luijten from Eindhoven University of Technology (TU/e) and Marcus Aldén from Lund University for their invaluable guidance and the opportunity to work in this cooperation project between these renowned institutions. I have sincerely appreciated and enjoyed your approachability and friendliness at all moments. Carlo, your eye for detail (the Dutch word is not appropriate) and your friendship were a great support.

I am indebted to many professionals who contributed to the construction of the HPVB and LOSA setups: Gerard van Hout, Wout de Boer, Theo de Groot, Bart van Pinxten, Hans van Griensven and Paul Bloemen. Thank you Viktor Kornilov, Manohar, Nico Dam, Zhou Lei, Maarten Meijer, Mayuri Goswami and Alexander Konnov for your fruitful help and technical discussions at TU/e. A special thank you to Liselotte Verhoeven and Jeroen van Oijen for the numerical modeling in our joined work. I share the credits of my thesis with the students that I had the pleasure to work with: Ralf van der Zanden, Gerben Jans, Peter Bertrand and Sander Derks.

It has been a great opportunity to work at Lund University in Sweden for the laser diagnostics measurements and for that I acknowledge Per-Erik Bengtsson, Henrik Bladh, Nils-Erik Olofsson, Jonathan Johnsson, Andreas Lantz, Bo Li and Zhongshan Li. I would also like to thank Gerard van Hout and Niels Leermakers to help me transport the experimental setup from Eindhoven to Lund and back.

I want to thank Kevin Thomson for sharing his knowledge on high pressure experiments as well as Mitchell Smooke for providing the LII data for comparison with our LOSA experiments. A thank you to my roommates: Xander, Miao, Atieh and Maurice for your sociability and for making our office a pleasant place to work. I would also like to thank Marjan Dijk for her organizational support and example of strength. I want to say to all my colleagues at the Combustion Technology division that I feel very fortunate to have met you, people from many different cultures, which has been a great learning experience in my life.

Concluding this thesis would not have been possible without the exceptional support and love of my Brazilian family: Valmir, Ana Tereza, Teopista, Marília (obrigado!) and of my Dutch family: Liz, Phil, Ernst, Guido, Anouschka, Sebas, Anne, Yonas, Nel and Sytske. A special thank you to my loved wife, Judith de Jong Andrade Oliveira, for supporting me each step of the way, encouraging me, understanding my absence and for the great care of our son Luca.